Biological and biomimetic mineralization via protein nanoribbon scaffolds

Susrut Akkineni

A dissertation

submitted in partial fulfillment of the

requirements for the degree of

Doctor of Philosophy

University of Washington

2022

Reading Committee:

James J. De Yoreo, Chair

Shuai Zhang

Lilo Pozzo

Program Authorized to Offer Degree:

Materials Science and Engineering

University of Washington

Abstract

Biological and biomimetic mineralization via protein nanoribbon scaffolds

Susrut Akkineni

Chair of the Supervisory Committee:
Professor James J. De Yoreo
Materials Science and Engineering

Understanding how protein scaffolds direct mineral morphogenesis is crucial for engineering bone and tooth and would open new vistas in hybrid materials design. In the case of tooth enamel, which is the hardest tissue in the body and consists of organized bundles of coaligned filamentous apatite crystals, co-aligned amyloid-like amelogenin nanoribbons (Amel NR) are hypothesized to provide the scaffold for amorphous calcium phosphate (ACP) precursor to apatite. From quantitative analysis of ACP nucleation rates on Amel NRs as a function of chemical potential, we see phosphorylated Amel NRs (pAmel NRs) are far more potent calcium phosphate nucleators than other amelogenin motifs or collagen, which provides the scaffold for bone. This potency stems from a periodic array of charged sites that provide a template for calcium phosphate ion binding on a low-energy interface. To extend this knowledge towards templating substrates on which pAmel NRs can be patterned for tissue engineering of synthetic bone or tooth, we employed block copolymer (BCP) lamellae. From these studies, we see bottom-up, biomimetic fabrication of filamentous mineral on substrates with high-fidelity may be possible through a combination of low surface energy, high nucleation rate, low growth rate and spatially separated discrete domains generated by aligned arrays of pAmel NR.

TABLE OF CONTENTS

LIST OF FIGURES

LIST OF TABLES

LIST OF ABBREVEATIONS

14P2	14 amino acid segment containing the 2nd proline at the amelogenin N terminus
Cterm	Highly charged DKTKREEVD segment at amelogenin C terminus
rH174	recombinant human amelogenin with 174 amino acids
ACP	Amorphous calcium phosphate
OCP	Octacalcium phosphate
BCP	Block copolymer
PS	Polystyrene
PMMA	Polymethylmethacrylate
PILP	Polymer-induced liquid precursor
AP	Apatite
Amel	Amelogenin
NR	Nanoribbon
Amel NR	Amelogenin nanoribbons
pAmel NR	phosphorylated amelogenin nanoribbons
HOPG	Highly ordered pyrolytic graphite
ssNMR	Solid-state Nuclear Magnetic Resonance Spectroscopy
FFT	Fast-Fourier Transform
LRAP	Leucine rich amelogenin protein
Amel NR	Amelogenin nanoribbons
pAmel NR	phosphorylated amelogenin nanoribbons
AFM	Atomic Force Microscopy
TEM	Transmission Electron Microscopy
SAED	Selected Area Electron Diffraction
σ	Supersaturation
J_o	Heterogeneous nucleation rate
α_{ACP}	Effective interfacial energy with respect to amorphous calcium phosphate
σ_{ACP}	Supersaturation with respect to amorphous calcium phosphate
A	Kinetic pre-factor
ω	Volume of mineral growth unit
k	Boltzmann's constant
T	Absolute temperature (kelvin)
R	Radius of hemispherical nucleus
ML	Mineral-liquid
MS	Mineral-substrate
LS	Liquid-substrate
α_{eff}	Effective interfacial energy
ΔG	Gibbs free energy
K_{sp}	Equilibrium solubility product

ACKNOWLEDGEMENTS

I express my sincerest gratitude to my doctoral adviser and mentor, Prof. James De Yoreo, for the unwavering support with endless patience and encouragement throughout the course of the program. Your advice on how to do science and be a scientist are extremely valuable and I will always remember them. I heartfully thank Dr. Jinhui Tao for mentoring me and guiding me through the experimental side of my research in the PhD program.

I appreciate and thank my collaborators: Prof. Stefan Habelitz, for sharing his expertise on amelogenin and guiding the project with the bigger picture in mind and keeping it relevant to enamel; Dr. Jiajun Chen for helping me on so many occasions, especially HR-AFM; Dr. Miao Song and Dr. Biao Jin for selflessly helping me with valuable HR-TEM data collection; Dr. Cheng Zhu and Prof. Hendrik Heinz for being such excellent and friendly collaborators, I truly enjoyed working with you on the molecular dynamics simulations and I hope we may work together again in the future; Dr. Johan Bonde, for making such great recombinant proteins and sharing them; Dr. Gregory Doerk for being such an excellent collaborator and selflessly providing us with beautiful block copolymer samples, it was a delight to work with you; Prof. Shuai Zhang for giving such great advice especially in the last stretch of my program and for collaborating with me on several occasions; Dr. Chenyang Shi for being so friendly, great to work with, and not to forget, some wonderful PiFM results; Ying Xia, Dr. Hao Shen, and Prof. Chun-Long Chen for sharing their systems and working together on them to answer really cool and interesting questions. I'm also grateful for the support from Tracy Baker, Elias Nakouzi, George Meigs, Odeta Qufoku, Benjamin Legg, John Loring, Jennifer Soltis, Yushi Bai and Guomin Zhu for helpful discussions and preliminary work. I'm also thankful for the support of NIH (grant R01DE025709-01A1), UW, CSSAS and PNNL for providing the framework and resources. I thank Prof. François Baneyx, Prof. Lilo Pozzo, Prof. Shuai Zhang, Prof, Lucien Brush and Prof. Chun-Long Chen for serving on my committee and their valuable feedback.

Last but not the least, I'm fortunate to have my family and friends in my life to support me through this long and arduous journey, through the ups and downs. I hope I can do the same for you in the future, if not more.

DISCLAIMER ON TEXT AND IMAGES

Parts of the text and images have been duplicated here from the article '**Amyloid-like amelogenin nanoribbons template mineralization via a low energy interface of ion binding sites. S Akkineni**, C Zhu, J Chen, M Song, S E Hoff, J S Bonde, J Tao, H Heinz, S Habelitz, J J De Yoreo. *Proceedings of the National Academy of Sciences* **119**, (2022)'

Chapter 1. INTRODUCTION

1.1 MOTIVATION

The control that living organisms exert on crystallization is extraordinary in terms of location, orientation, size, morphology, phase and efficiency, a stark contrast to state-of-the-art synthetic crystallization. However, the role of many organic and inorganic components and mechanisms by which biomineralization occurs are not well understood. As a result, hierarchical organic-inorganic hybrid structures (or hybrid materials), such as those in tooth enamel and bone, which are ubiquitous in biominerals (**Figure 1.1**), remain challenging to synthesize *in vitro*. Unlocking these mechanisms holds the key to tissue repair and synthesis of advanced materials with superior and novel structure, function, property, and performance relationships.

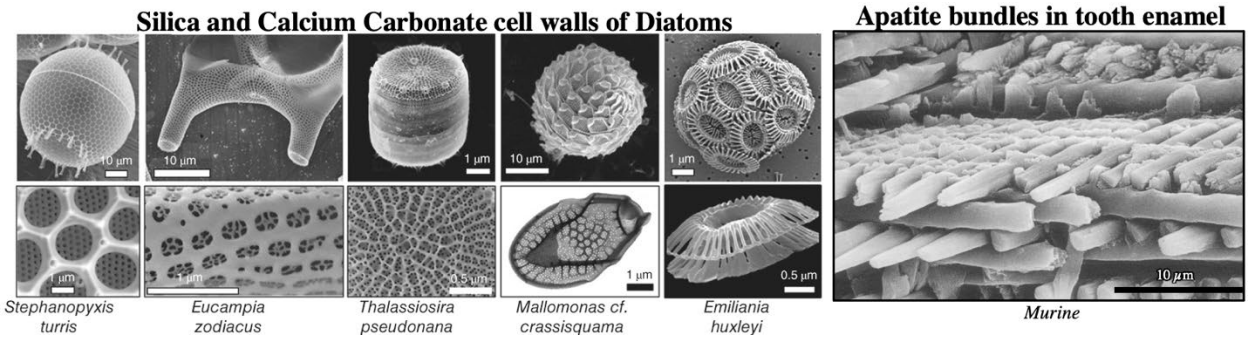

Figure 1.1. Architectures of silica, calcium carbonate and calcium phosphate biominerals. Reused with permission of John Wiley & Sons - Books, from Ref[1].

Current methods for fabricating biomimetic architectures typically involve a top-down and bottom-up approach which use high temperatures/pressures and rigid scaffolds. Moreover, the organization of inorganic crystals in these composites are often anisotropic in three-dimensions (3D)[2], which is not the case in their biological counterparts[3]. Biominerals, such as tooth enamel, are more complex, possessing an additional level of patterning in 3D, as well as aligned and crystallographically misoriented crystals, which were recently shown to provide a toughening mechanism[3] (**Figure 1.2)**. The higher level of inorganic crystal organization here typically involves cellular movements that secrete a self-assembling organic scaffold such as protein or

polysaccharide fibers. Hence, in this work, I sought to understand how protein scaffolds direct morphogenesis of inorganic matter into organized composites—ultimately to achieve unique properties. I do this in context of tooth enamel—the hardest and most resilient material in the human body, and of vital importance to oral healthcare.

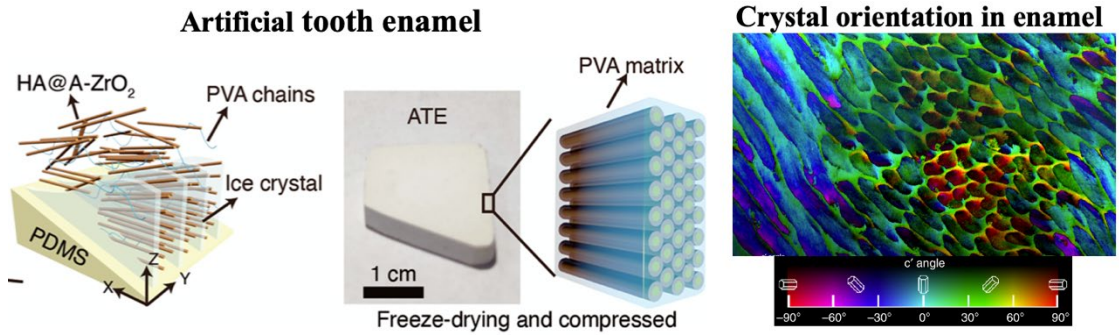

Figure 1.2. Microstructure of state-of-the-art artificial tooth enamel[2] versus human tooth enamel[3]. Adapted with permission of American Association for the Advancement of Science, from Ref[2]

1.2 How are filament or plate shaped biominerals made?

The uniqueness of enamel is in the microstructure and the underlying process which involves the secretion of an organic matrix and concomitant formation of amorphous calcium phosphate (ACP) within, and eventual organization and transformation into acicular crystalline apatite (**Figure 1.3**)[4,5]. The process, called *amelogenesis,* results in a hierarchical nanocomposite with a remarkable interwoven rod-interrod pattern (also called decussation or Hunter-Schreger bands), as shown in **Figure 1.3** H and I for murine enamel, which is made of bundled apatite filaments ~50 nm wide (26 nm x 63 nm for human enamel [6]) and several microns long. The long-axes (*c* axis) of all filaments in each bundle are roughly parallel to one another and the misorientation between them is thought to provide a fracture-resistant, toughening role that is unique to enamel [3]. Similar bundles of apatite filaments are observed for other mammalian enamel, though the Hunter-Schreger bands or decussation pattern—which is key to the mechanical

performance—varies from species to species [7,8], presumably orchestrated by the secretory cells (ameloblasts).

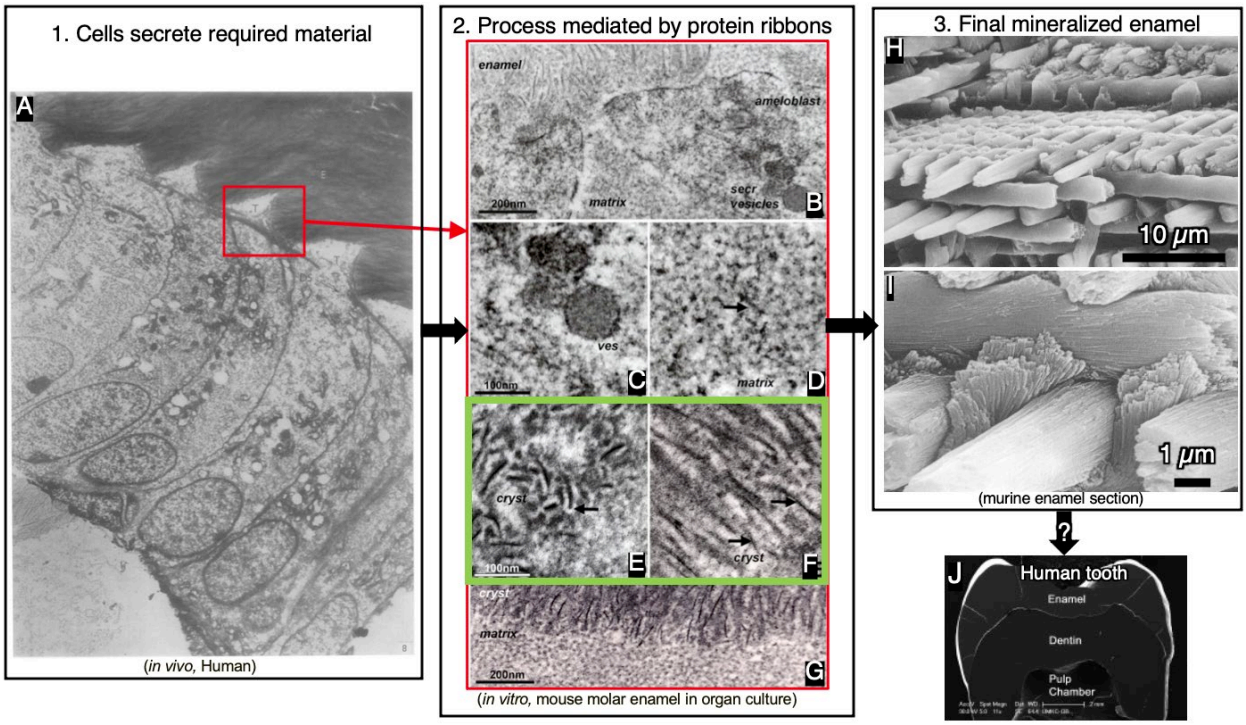

Figure 1.3. Electron micrographs of enamel at various stages. (**A**) sections of human enamel showing ameloblasts secrete proteins and mineral at the dentin-enamel junction (magnification: x 7700) [4]. (**B-D)** *in vitro* organ culture experiment showing vesicles that contain matrix proteins are secreted by ameloblasts and form the scaffold for mineralization [9]. (**E**) amorphous calcium phosphate forms around the self-assembling protein nanoribbons [9] which are initially randomly oriented. (**F**) crystalline calcium phosphate forms from the amorphous precursors [9]. (**G**) junction between protein matrix with amorphous mineral and crystals [9]. (**H**) nearly matured rat incisor enamel without any residual protein matrix [5]. (**I**) higher magnification of (H) showing each rod and interrod consists of 50 nm wide apatite filament. Each rod or interrod with bundled filaments is formed by a single ameloblast. (**J**) Multi-layered structure of human molar tooth section.

The initial human enamel matrix consists of 60-70% water, 20-30% proteins and 15-20% mineral ions. However, the final tissue is reported to have a composition of approximately 94-96% mineral, 2-5% water and 1-2% proteins [10], because during maturation stage, 98% of the scaffold (protein matrix) is enzymatically digested [9]. Thus, disabling tissue regeneration, and ultimately leaving insufficient evidence to identify individual protein structure-function and crystal growth

mechanism[11]. Therefore, the apatite crystallization pathway and matrix-mediated mineralization mechanism remains unclear.

The filament morphology and the observation of an intermediate amorphous mineral phase closely associated with the organic scaffold are not unique to mammalian tooth enamel, they were observed in other species where the organic matrix was not completely digested (**Figure 1.4**) [12–15]. For example, the zebra fish bone consists of an initial amorphous phase closely associated with collagen fibers that evolves to filament- or plate-like apatite[15]. Another example is the sea urchin spicule, which is thought mineralize calcite through the formation and aggregation of amorphous calcium carbonate nanoparticles guided by the SpSM protein scaffold[12,16,17]. This process is not strictly restricted to proteins or calcified tissue either, fibrous scaffolds of the polysaccharide chitin are believed to guide the formation of magnetite through an amorphous iron oxide phase[13,15]. The crystallization pathway involving aggregation of an amorphous or a disordered phase is attributed to nonclassical crystal growth processes [18], rather than classical crystal growth which involves an ion-by-ion mode and formation of a stable nucleus [19]. Though the mechanism in each system may vary, there are a few common elements which I outline here based on previous reports [19–24]: 1) involvement of an organic scaffold in organizing and templating the mineral either directly or through interaction with other macromolecules, 2) a scaffold comprising hierarchically self-assembling macromolecule that forms a supramolecular fiber or nanoribbon, 3) an amorphous precursor closely associated with the scaffold in the initial stages, and finally 4) phase transformation of the precursors into the thermodynamically stable mineral phase.

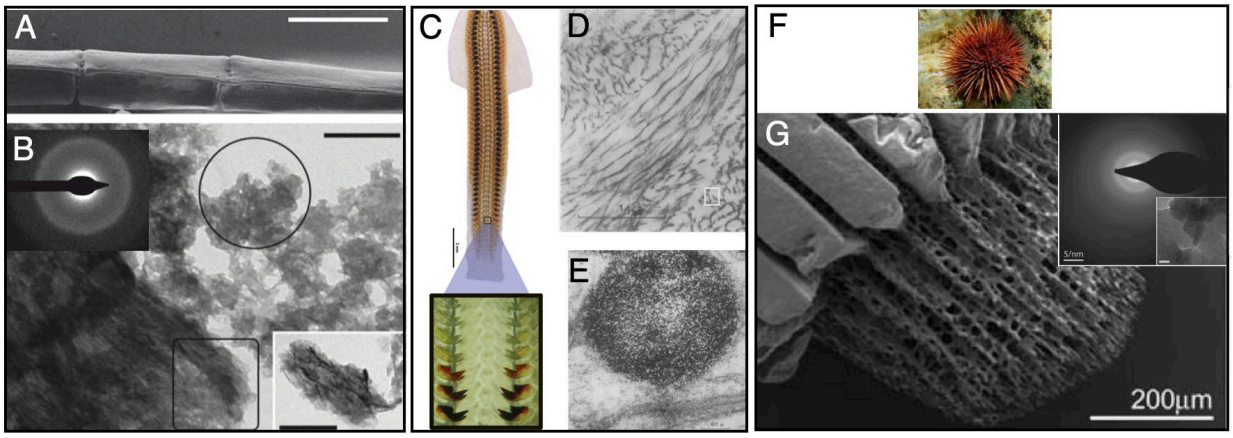

Figure 1.4. Amorphous mineral closely associated with organic scaffolds. Collagen and ACP in Zebra fish bone [15]: (**A**) SEM micrograph of native fin ray bone (scale bar: 200 µm) and (**B**) TEM micrograph of mineral particle aggregates, encircled particle shows an amorphous nature in the corresponding SAED and area marked in rectangle is poorly crystalline apatite (scale bar: 100 nm); Copyright (2008) National Academy of Sciences. Chitin and amorphous iron oxide in Chiton teeth: (**C**) Light micrograph of the radula with inset showing stages of tooth development [14]. (**D**) Fibrous meshwork of unmineralized proteinaceous tooth and (**E**) amorphous body associated with the organic framework [13]. Adapted with permission of Elsevier, from Ref [13]. Calcite and SpSM in Sea Urchin spicules: (**F**) stock photo of *Paracentrotus lividus* from www.snorkeing-report.com and **G**) SEM of regenerating spines and corresponding SAED of the amorphous calcium carbonate precursor [12]. Adapted with permission of American Association for the Advancement of Science, from Ref[12]

These observations are intriguing and raise more questions: 1) are there amino acids with functional groups, such as phosphorylation or glycosylation, common to these macromolecules? 2) does the protein self-assembly play a role in the final structure or is the bundled morphology only due to the mineral crystallization in a confined space? 3) is the intermediate amorphous phase important? and if yes, why? 4) in some cases, the final crystallite has a 'beads on a string' or granular morphology made of nanospheres, whereas others have a smooth single crystal, why does this occur and how?

Other authors have researched these questions on a variety of biomineral systems[19,23–31], however a clear mechanistic understanding in context of enamel based on careful in situ,

thermodynamic, or kinetic studies is yet to be developed. Therefore, this field has garnered intense attention from materials chemists and engineers towards the study of structure-function-property relationship between the various components. In the case of bone, the self-assembly of the collagen scaffold and mineralization of apatite is believed to be highly synergistic and concomitant, one influencing the other while interacting with a wide variety of soluble macromolecules that control the nucleation, growth, phase transformation, morphology, and crystal habits [32–36]. Some researchers also hypothesize the amorphous phase is formed first as it is more kinetically accessible than other thermodynamically favorable phases, and the amorphous nature suggests the particles may be easier to deliver, fill empty spaces, mold, dissolve and reprecipitate to the stable state since the final crystal is often not easily dissolved at physiological conditions[17,19,37–39]. Compared to bone where the collagen matrix persists, tooth enamel mineralization is challenging to study due to digestion of the organic matrix and not much is known about the structure-function relationship between the scaffold and various organic constituents and their impact on the thermodynamics and kinetic parameters governing the nucleation growth and phase transformation of the mineral from amorphous phase to the apatite crystals[40–44]. Therefore, I provide background on the organic matrix-mediated mineralization in tooth enamel in the following sections preceding my study on nucleation on nanoribbons.

1.1 INSOLUBLE MATRIX-MEDIATED MINERALIZATION IN ENAMEL

Weiner suggested that organic matrices in several biomineralization systems are organized according to the same basic motif, which is a core of relatively hydrophobic structural macromolecules (usually proteins) and surface layers of acidic proteins and polysaccharides [45,46]. The more acidic hydrophilic macromolecules are closely associated with the mineral phase,

whereas the relatively hydrophobic components are spatially removed from the mineral. These two types of proteins have led to categorization of the hydrophobic component as framework, scaffold, substrate, or insoluble matrix macromolecules and the hydrophilic as additives, surface, or soluble macromolecules.

Therefore, the structural organization of the organic matrix in enamel, which primarily consists of proteins, can provide knowledge on the biomineralization process. The enamel protein matrix, from secretion to maturation stage, was identified to consist of amelogenin (*Amel*), enamelin (*Enam*), MMP-20, KLK-4, amelotin and ameloblastin [47]. Of these, *Amel* constitutes 90% of the developing enamel protein matrix and is later digested by KLK-4 during the maturation stage. Irregular production of *Amel* in humans can lead to *Amelogenesis imperfecta*, resulting in thin, pitted and fragile enamel layer, and is major genetic disease that affects oral health of the population [48].

Due to ethical restrictions concerned with studies on developing enamel in human embryos, many studies focus on murine, porcine and bovine models to investigate the biomineralization process and enamel-related diseases. By comparing wild-type and *Amel*-knockout (**Figure 1.5**) mouse models, researchers were able to provide evidence for the importance of *Amel* and determine enamel structure in absence of *Amel*, which results in relatively thin enamel that is brittle and disorganized[49,50].

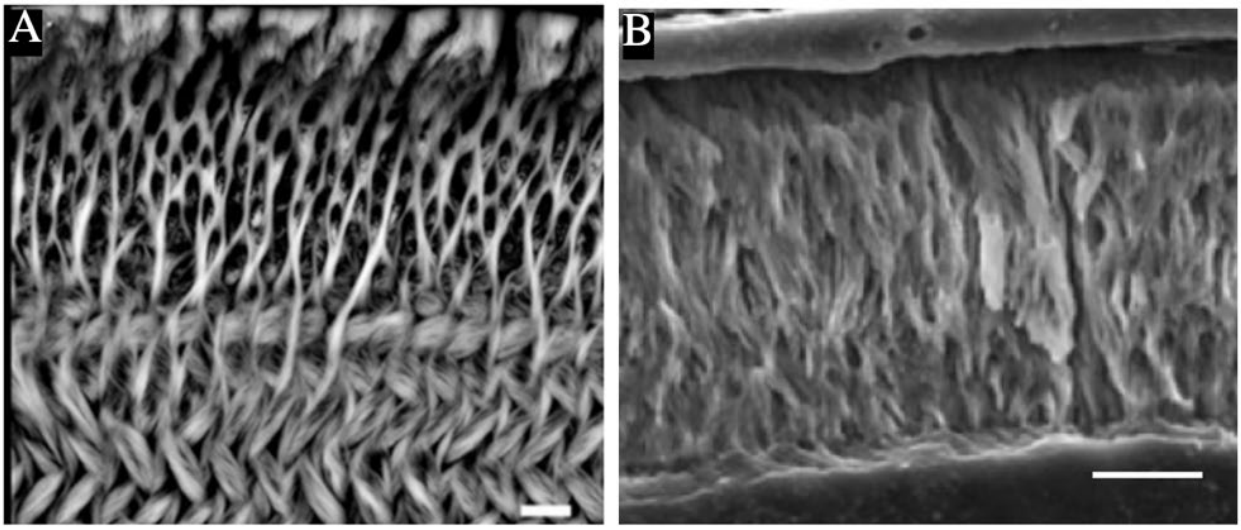

Figure 1.5. Microstructure of enamel in (**a**) wild-type mouse (**b**) amelogenin-knockout mouse [50,51]. Reprinted with permission of The American Physiological Society, from Ref[50]

1.2 HISTORY OF AMELOGENIN: AN INTRINSICALLY DISORDERED PROTEIN

Anfinsen's Dogma for protein structure states that the primary amino acid sequence defines the final thermodynamically stable secondary, tertiary, and quaternary structures[52]. However, amelogenin is categorized as an intrinsically disordered protein (IDP)[53], which falls outside the principles governing protein folding[54]. For IDPs, the primary amino acid sequence can have a partially or completely unfolded structure as the native thermodynamically stable state, and interchange between different structures depending on the local chemical environment as well as undergo self-association and interactions with itself, other proteins, ions or crystals[55–57]. Therefore, the structure cannot be easily solved by state-of-the-art computational prediction algorithms such as AlphaFold or RoseTTAFold [58,59]. This makes structure-function studies considerably more challenging as they require extensive *in vitro* experiments that consistently generates supramolecular structures identical to those *in vivo*; all while not knowing the precise chemical environment in developing enamel.

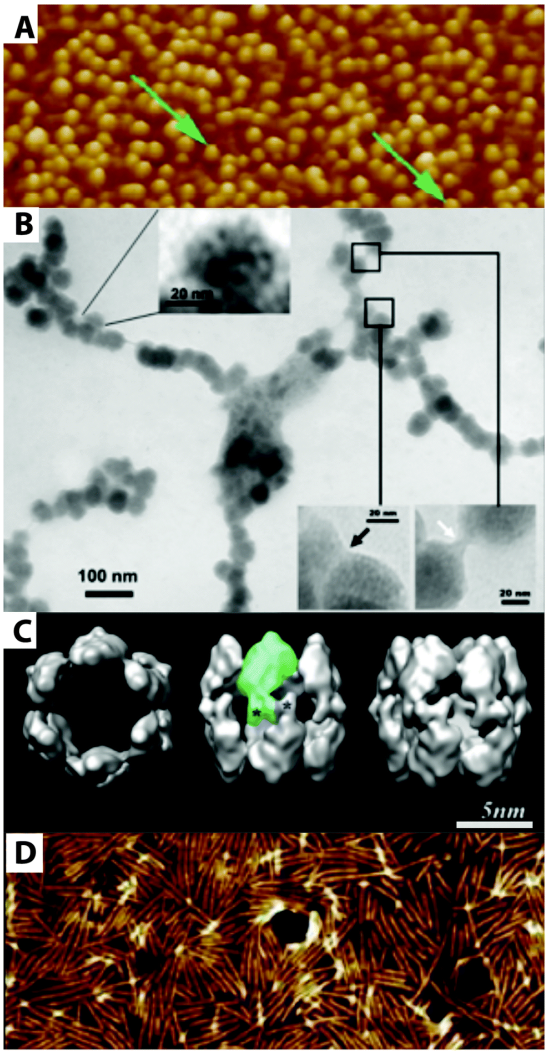

Figure 1.6. Quaternary structures of amelogenin[60]. (**A**) Nanospheres at pH 8 on mica[61], (**B**) Chains of nanospheres grown by evaporation with PEG[62,63]. (**C**) Structure of amelogenin oligomers formed at pH 8. (**D**) amyloid-like nanoribbons at pH 4.5 in presence of calcium and phosphate ions[64]. Reproduced with permission of Royal Society of Chemistry, from Ref. [60].

Despite these challenges several groups over the past 30 years performed *in vitro* self-assembly studies to show *Amel* quaternary protein structure is highly dependent on concentration, pH, and presence or absence of mineral (calcium or phosphate) ions during the self-assembly process (**Figure 1.6**), as is the case with IDPs [60,63–66]. Of these, numerous studies on mineralization start from the widely explored model in which amelogenin assembles into supramolecular nanospheres or oligomers **(**Figure 1.6 A), which lack a quaternary structure, have a wide size

distribution, and disassemble on apatite[40,41,43,60,67–79]. These nanospheres were then proposed to form larger clustered complexes containing calcium and phosphate which may form chains (beads on a string) and nucleate ACP/apatite in their cores[63].

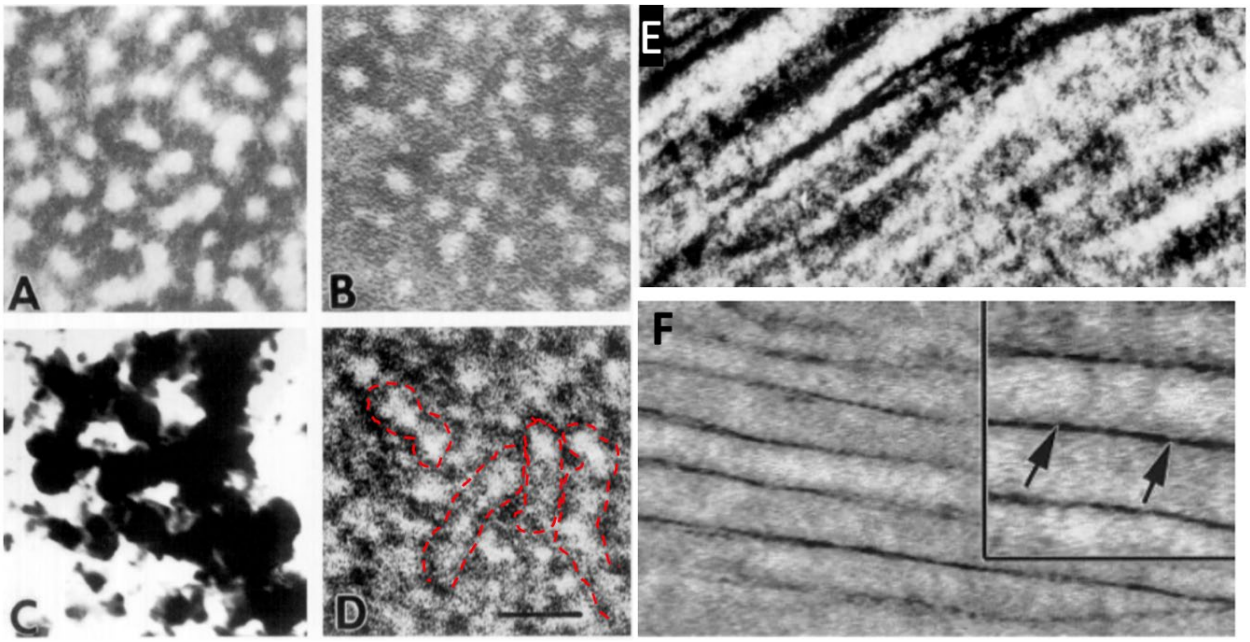

Figure 1.7. Transmission electron microscopy of mouse enamel sections from secretory stage with staining used as evidence of nanospheres. (**A-C**) are images of nanospheres prepared using (A) phosphotungsten (bright features), (B) Uranyl acetate (bright features) (C) palladium chloride (dark features), (**D**) is stippled material from in vivo section stained with uranyl acetate (bright features), and (**E**) shows protein matrix with mineral from Fincham et al. 1995 [75]. (**F)** TEM image of uranyl acetate-stained enamel from wild-type in Paine et al 2000 shows ribbon-like assemblies (bright features) [80]. Reprinted with permission of Elsevier, from Ref.[75,80]

However, the pathway by which these nanospheres assemble into a scaffold of bundled fibers that template discrete AP filaments is unclear (Figure 1.6 B) [40,63,67,75,80]. In enamel sections containing mineral, the mineral resides on the periphery of the ribbon and not in the core as the nanosphere-Ca-P cluster hypothesis suggests [75,80]. Moreover, the morphology of a chain of amelogenin nanospheres does not match the morphology of *in vivo* ribbon-like protein assemblies. This is not surprising since the basis for the nanosphere model was purely morphological, and

considerable uncertainty exists due to the *ex-situ* TEM micrographs which show evidence of sphere-like motifs in stippled materials of stained animal sections and co-existence of ribbon-like feature (outlined with red-dashed lines in **Figure 1.7** [75]. Because, in such studies presenting *ex situ* evidence of nanospheres[75,80], one can easily argue that the existence of ribbons is an artifact of the organization of spheres or the appearance of spheres in ribbon could be artifacts of sample preparation and imaging.

In contrast, recent *in vitro* reports using aged solutions at acidic pH demonstrate that full-length Amel can indeed adopt an amyloid-like (cross-β-sheet) quaternary structure and self-assemble into nanoribbons (NRs) 17 nm wide, 3-4 nm in thickness and several microns long (**Figure 1.6 C**) that can aggregate to form bundles [64,81]. Supporting this model*, in vivo* studies revealed the presence of highly-aligned bundles of ribbon-like β-sheet protein assemblies in the developing enamel matrix of various mammals (**Figure 1.8**), including humans [4,81–87]*,* and these NRs match the morphology and quaternary structure of ribbons assembled *in vitro* from both recombinant human Amel (rH174) [65,88,89] and synthetic peptides [81]. The link between the nanosphere model and Amel NRs is also yet to be clearly established but a recent *in vitro* study suggests nanospheres (or oligomers) can form nanoribbons in acidic or alkaline conditions over time scales that are relevant to developing enamel [88.] This transition from a compact globular (random-coil) structure to β-sheet protofibrils (which resemble the stippled material in enamel matrix), then to amyloid-like (cross-β-sheet) quaternary structure nanoribbons has been extensively reported for amyloid sequences [14,90–99]. Future investigations on the protein conformation in the secretory vesicles and the stippled material in enamel matrix may fill this knowledge gap on protein conformation through amelogenesis.

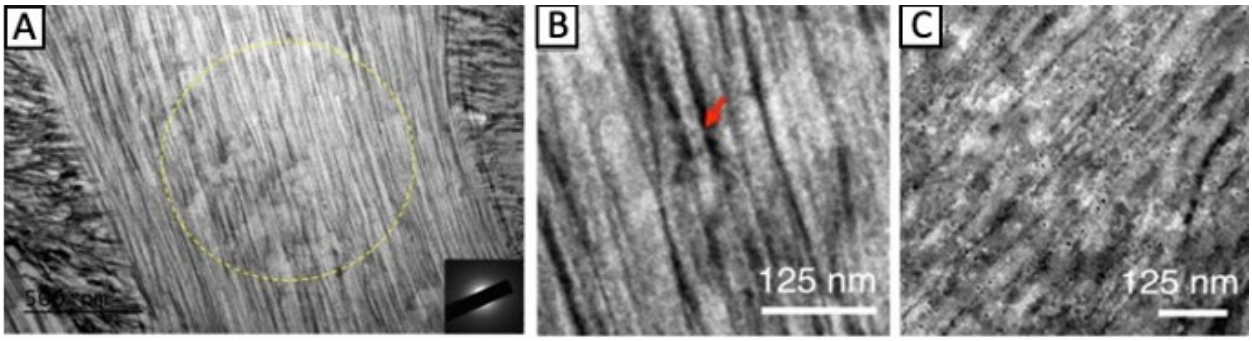

Figure 1.8. (A) TEM image of demineralized, stained secretory stage enamel section reveals a vast protein nanoribbon network with the signature enamel pattern. (B) Higher magnification TEM image of one region in A showing filamentous nature of enamel protein matrix. (C) Immunostaining of demineralized wild-type secretory stage enamel section stained positive with amelogenin antibody. Section was incubated with primary amelogenin antibody from rabbit and secondary antibody from goat with 5nm gold labeling in sequence and negatively stained.[100]

In vivo observations using KLK4 knockout mice suggest Amel NRs are involved in mineralization of AP filaments via ACP which form during the secretory stage of amelogenesis[87] (**Figure 1.9** A-C), while recent in vitro experiments demonstrate that synthetic NRs can indeed template growth of AP filaments starting with an amorphous precursor formed in the presence of acidic macromolecules[86] (**Figure 1.9**). Thus, Amel NRs provide a conceptually simple scaffold for AP filament formation[101] **(Figure 1.10**). However, the extent to which Amel NRs facilitate ACP nucleation, whether the mineral is templated on the flat-face or edge of the NR, the mechanism that leads to NR templating of ACP, and the basis of this mechanism in the relationship between NR and mineral structure remain unknown due to the complex crystallization mechanisms and variety of macromolecules involved.

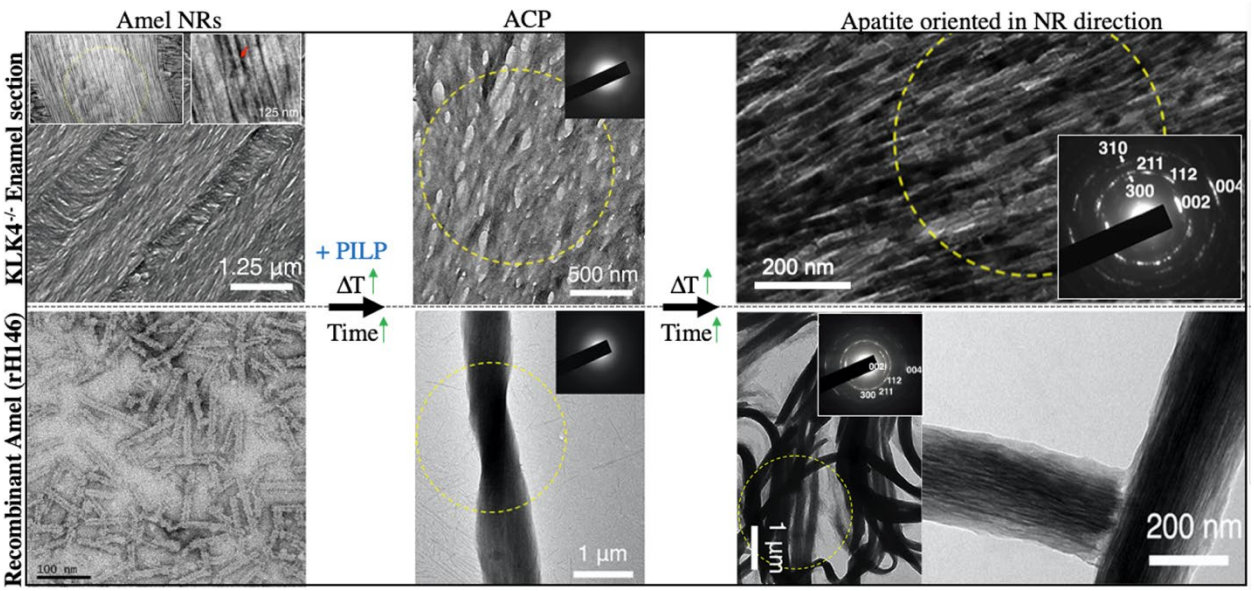

Figure 1.9. in vitro Amel NR templated mineralization of oriented apatite via ACP in enamel section of KLK4 knockout mouse after demineralization and recombinant amelogenin without C terminus (rH146) using PILP[64,86]. Adapted with permission of Copyright (2020) National Academy of Sciences, from Ref[86]; and adapted with permission from Ref.[64]. Copyright (2012) American Chemical Society

Therefore, this work does not address which structure is more relevant to enamel formation and at which stage, because one can always point to papers that argue for both cases that have been reviewed and published. Rather we focus on the question, if β-sheet Amel NRs are hypothesized to play a role in apatite formation, do they, in fact, act as strong nucleators of ACP and, if so, why?

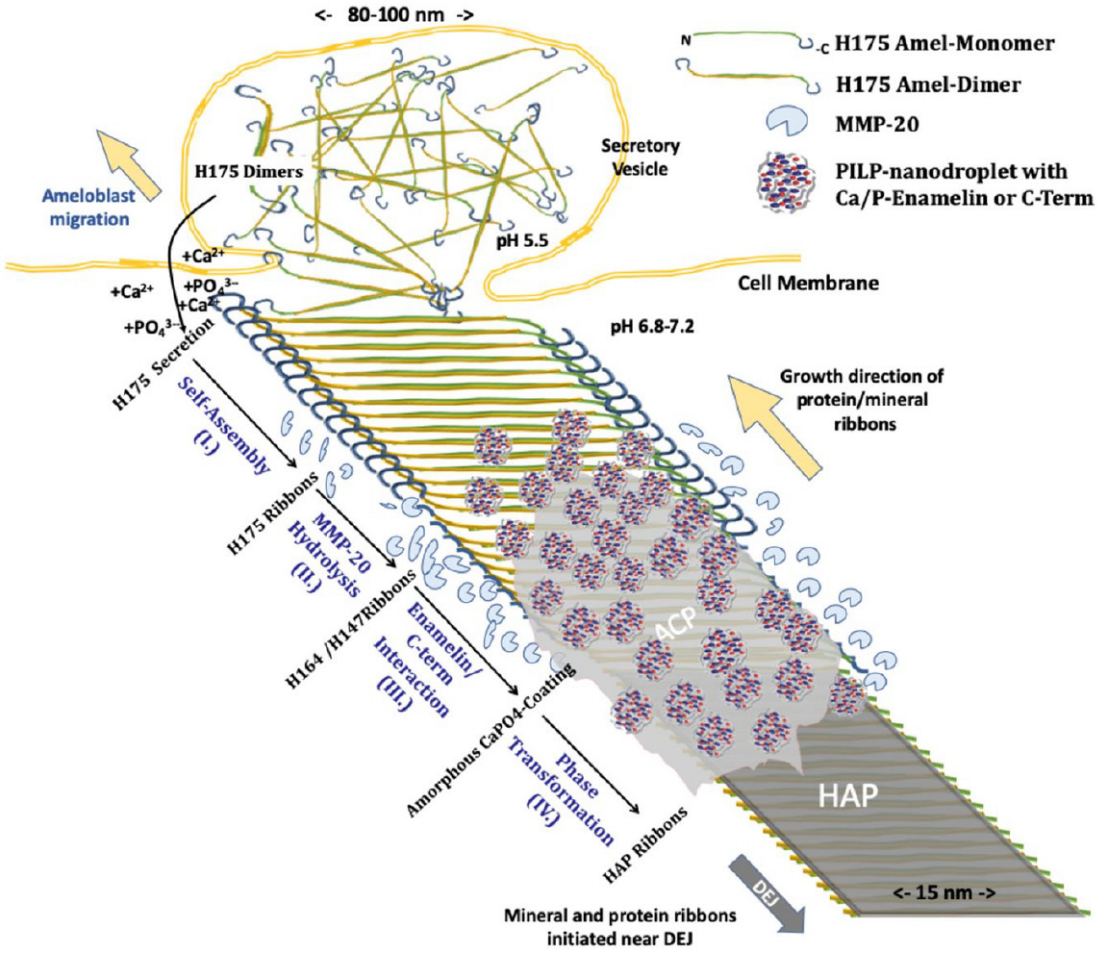

Figure 1.10. Model of NR-templated crystallization pathway[101]. Monomer or dimeric full-length human amelogenin (H175) is exocytosed at Tome's process. Step 1: self-assembly into NRs. Step 2: MMP20 cleaves C-termini at both edges of NR to form H147. Step 3: PILP nanodroplets of calcium and phosphate form and interact with H147 NRs. Step 4: Nucleation of ACP on NR from PILP and transformation into HAP with width ~15 matching NR width. NR assembly and concomitant mineral growth advance as ameloblasts recede and continue to exocytose matrix proteins; thus, ribbons follow cell pathway and create the decussation pattern of prismatic enamel.

Chapter 2. SELF-ASSEMBLY AND STRUCTURE OF AMELOGENIN NANORIBBONS

2.1 STRUCTURAL AND FUNCTIONAL BLOCKS OF AMELOGENIN

The cross β-sheet conformation of amyloids is a stable quaternary structure that is usually formed in context of disease, when native structured proteins are misfolded, and identifiable by their characteristic ribbon or acicular morphology. However, there has been increasing evidence of amyloid structure in proteins that perform a biological function in bacteria, fungi, insects, and humans[93,102,103].

Several in vitro studies on various amyloid sequences have shown that cross β-sheet ribbons self-assemble and aggregate through a multistep pathway, from oligomers to β-sheet protofibrils, protofibrils to cross β-sheet fibers (or ribbons), and finally fibers into bundles that make up the tissue[92,95,104]. The self-assembly of β-sheet protofibrils and cross β-sheet fibers is non-spontaneous, they have a characteristic sigmoidal curve, with an initial lag/nucleation phase followed by elongation phase that eventually plateaus as the concentration of precursors drops[105]. This is the inherent behavior of nucleating systems (typically found in inorganic systems) and its potential involvement in synergistic and concomitant self-assembly and mineral templating is intriguing and worth exploring in the future[19,25].

The self-assembly and supramolecular structure for Amel NR of 1) recombinant human full-length amelogenin (rH174, which is H175 without methionine-1 and serine-16 instead of phosphoserine-16), 2) MMP20-cleavage product (rH146, which is H147 without methionine-1),

and 3) analog peptides (14P2 and p14P2) were previously investigated by AFM[64–66,81,86,88,89], negative stained TEM[64,66,81,86,89], XRD[65,88], microscale thermophoresis[64], and SAXS[64,65] in addition to spectroscopic studies with NMR[106], FTIR[65], AFM-SNOM[81], AFM-IR[86], CD[81], Thioflavin-T[81] and other amyloid- and amelogenin-specific assays[81,87,100]. However, advanced characterization with cryo-EM, solid-state NMR and single-fiber x-ray diffraction on the full-length protein is yet to be reported, therefore an atomically precise model does not currently exist. The studies till date show Amel NR of rH174 has a bi-layer structure (cross β-sheet) with a hydrophobic core and hydrophilic exterior (Figure 2.1), formed by self-assembly of β-sheets at the hydrophobic N-terminus interface in a steric-zipper conformation (anti-parallel direction). The ultrastructure of rH146 also shows the hydrophilic C-terminus (DKTKREEVD segment, labelled as Cterm) cleaved by MMP20 likely resides at both edges of the rH174 ribbon giving a winged (or trough) appearance. This Cterm segment is hypothesized to play a role in binding with (010) facet of apatite and effectively inhibiting growth in the a and b axis while promoting growth in the (001) or c axis[44,107–109], however it's impact on ACP nucleation is yet to be characterized and will be a subject of investigation here. Native human amelogenin also has a single phosphorylated serine, which is hypothesized to play a crucial role in stabilizing a transient ACP mineral phase in developing enamel[76,77,110–112], however, synthesis of recombinant phosphorylated full-length amelogenin for detailed *in vitro* studies has been challenging. In addition, the variable, histidine- and proline-rich central domain and other segments of Amel may also play a role in self-assembly or mineralization [43,113–116], however, their structures and functions are unclear in context of Amel NRs and were not investigated here.

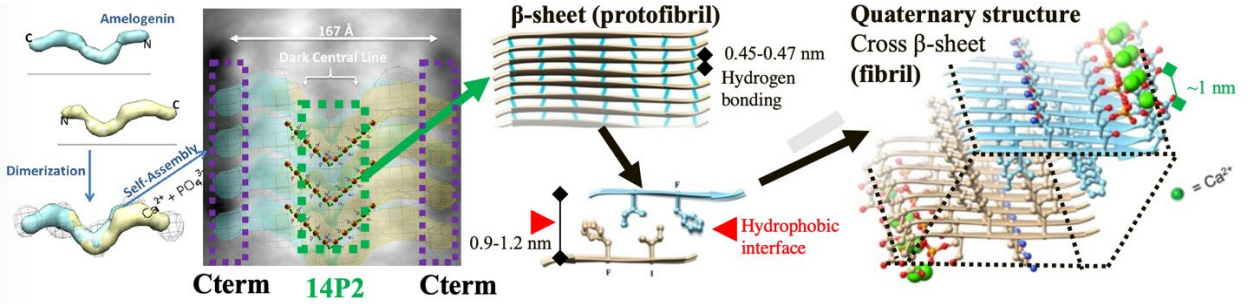

Figure 2.1. Scheme of proposed nanoribbon self-assembly and structure adapted from previously published TEM, XRD, FTIR, and NMR measurements[64,81]. Adapted with permission from Ref.[64], Copyright (2012) American Chemical Society.

Bioinformatics and molecular modelling of full-length *Amel* using the amyloid-like structure have revealed an evolutionarily conserved segment near the N-terminus, labelled 14P2, with high propensity to fold into β-sheets, and further guide the folding of the full-length protein into cross β-sheets, indicated by the dark central line in the electron micrograph of the *Amel* nanoribbon [81] (**Figure 2.1**). *In vitro* studies show full-length *Amel* without the 14P2 segment cannot form nanoribbons, and more recently, *in vivo* studies confirmed absence of the 14P2 domain drastically impacts organization of the organic matrix pattern and mineral morphology unique to enamel, forming a thin and disorganized mineral layer with non-discrete apatite[87] (**Figure 2.2** and **Figure 2.3**). These studies provide strong evidence that self-assembly of nanoribbons at the 14P2 domain is crucial to enamel structure. In addition to 14P2's role in *Amel* self-assembly, 14P2 polypeptides were also reported to have amyloid-like properties and independently self-assemble into fibrils [81].

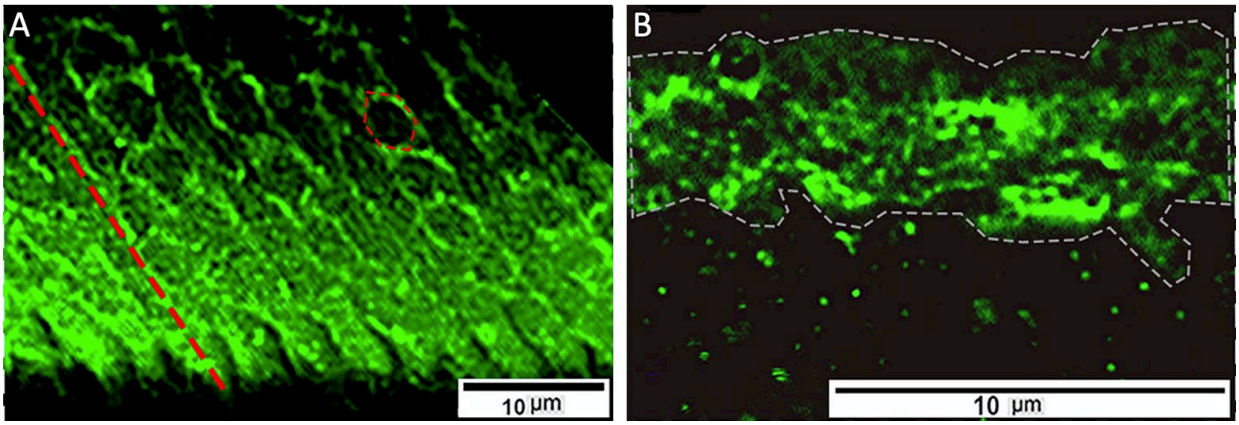

Figure 2.2. Super-resolution confocal microscopy and immunostaining 14P2 domain in amelogenin is crucial for typical tissue pattern in developing enamel matrix. (**A**) with 14P2 where amelogenin-positive signal (green) is distributed either along the long axis of enamel rods (indicated by dotted-red line) or hexagon-shaped (red-dotted hexagon line). (**B**) without 14P2 shows amelogenin (green) distributed in enamel matrix without a pattern [87]. Adapted with permission of John Wiley & Sons – Books, from Ref. [87]

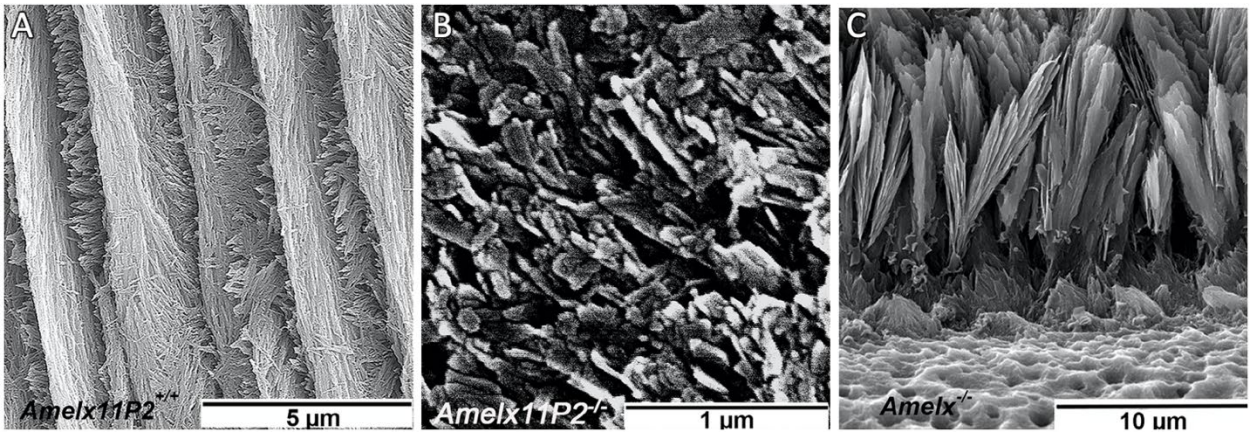

Figure 2.3. 14P2 and amelogenin are crucial for decussation pattern of enamel apatite. Microstructure of mice enamel with (A) amelogenin shows the regular pattern made of discrete apatite filaments, (B) amelogenin without 14P2 domain shows disorganized filaments and sheets, and (C) without amelogenin short fan-like mineral made of apatite platelets [87]. Adapted with permission of John Wiley & Sons – Books, from Ref. [87]

2.1 DRAWBACKS OF USING CROSS-β-SHEET NANORIBBONS

The previously reported *in vitro* protocol for NR self-assembly is unsuitable for *in situ* AFM analyses of calcium phosphate nucleation because it leads to multiple NR polymorphs and has pre-existing calcium and phosphate salts in solution that preclude measurements of nucleation rates at known supersaturations **Figure 2.4**. Calcium and phosphate were used because self-assembly studies have shown cross-β-sheet NRs do not form in their absence. However, these reports neglected the presence of β-sheet NRs (precursors to cross-β-sheet NRs) in the background of their samples, likely due to unavailability of high-resolution *in situ* microscopy to characterize sub-nanometer features. Furthermore, several reports on amyloid sequences show that salts typically promote aggregation of the β sheet protofibrils into the cross-β-sheet ribbons by inhibiting intermolecular or NR-to-NR repulsion. Therefore, salts are likely not required for self-assembly of β-sheet ribbons but only required for their aggregation into cross-β-sheet NRs.

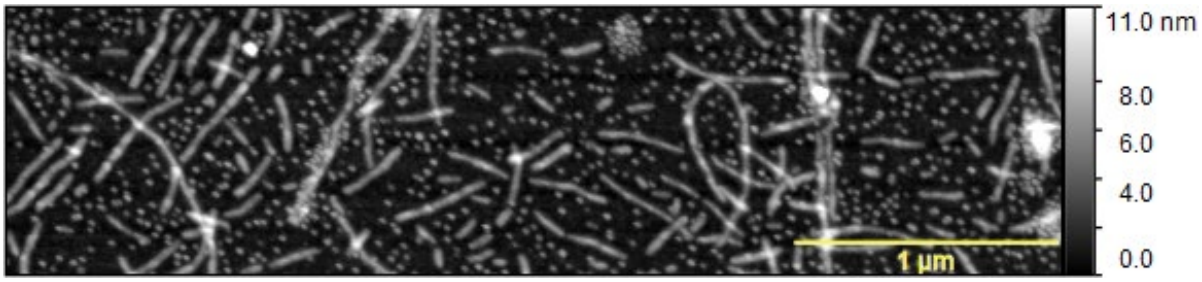

Figure 2.4. Polymorphs of recombinant full-length amelogenin nanoribbons prepared in presence of calcium and phosphate ions. Ribbon dimensions (5 ± 1.17 nm tall, 30.75 ±7.73 nm wide) are not uniform and nanospheres, salt precipitates are observed and surface coverage not uniform

2.1 APPROACH WITH β-SHEET PRECURSORS OF CROSS-β-SHEET NANORIBBONS

β sheet interactions are intrinsic to the sequence and conformation compared to other interactions such as π-π bonding, van der Waal's forces or hydrophobicity that are involved in the formation of cross-β sheet and higher order structures. Therefore, single β sheet protofibrils are

the rational choice to obtain consistent interfaces. Hence, the protocol was redesigned to exclude Ca and PO_4 salts and isolate single β sheets on a charge neutral surface that can coat 100% of our observed area under AFM (at least 20 x 20 μm scan area), which is also transferable to other sequences. This was performed by lowering pH from 3.1 to 1.94 and lowering concentrations from 1 mg/mL to 0.1 mg/mL for self-assembly on HOPG [92,95,117,118].

14P2 was used as a model sequence for a detailed, high-throughput studies due to commercial availability, prior data on structure of nanoribbons, and self-assembly kinetics in the order of minutes relative to rH174 that takes several hours [81,88]. Most importantly, 14P2 provided a better map of the NR backbone structure since in situ AFM is unable to clearly resolve the packing of monomers in NR with long hydrophilic functional groups or flexible tail end domains (phosphoserine and Cterm domain). As observed for Cterm sequences compared to 14P2, the flexible tail likely makes the surface appear disordered. This same effect was observed in highly crystalline sheets of peptide-mimetic molecules possessing hydrophilic headgroups; even though both XRD and TEM demonstrate high crystallinity, the surface appears disordered [119].

2.2 Design of structure-function study

To address the knowledge gaps in the role of Amel NR in templating apatite via ACP, we performed *in situ* Atomic Force Microscopy (AFM) analyses of calcium phosphate nucleation on self-assembled NRs of the full-length protein, as well as evolutionarily-conserved sub-segments hypothesized to be important for: 1) self-assembly; 2) stabilizing ACP (i.e., phosphoserine-16); and 3) binding with the AP surface, i.e., the C-terminus, which is cleaved by Matrix metalloproteinase-20 (MMP20) during amelogenesis at the site indicated in **Figure 2.5 A**[44,81,110,113]. To further understand the underlying chemical interactions and correlate NR and

mineral structures with energetics, we performed molecular dynamics (MD) simulations of the conformational states of NRs formed from these peptide sub-segments and compared them with the growth unit of ACP (the $Ca_2(HPO_4)_3)^{2-}$dimer).

Based on the above hypotheses, five sequences were designed. Three were non-phosphorylated sequences: one recombinant full-length human Amel (rH174) and two peptide analogs consisting of the domain that drives self-assembly (14P2) and this 14P2 domain with the truncated C-terminus appended to it (14P2Cterm), as shown in **Figure 2.5, A** to **C**. Phosphorylated versions of both peptides, p14P2 and p14P2Cterm, were also synthesized with phosphoserine sites as highlighted in **Figure 2.5, A** to **C**.

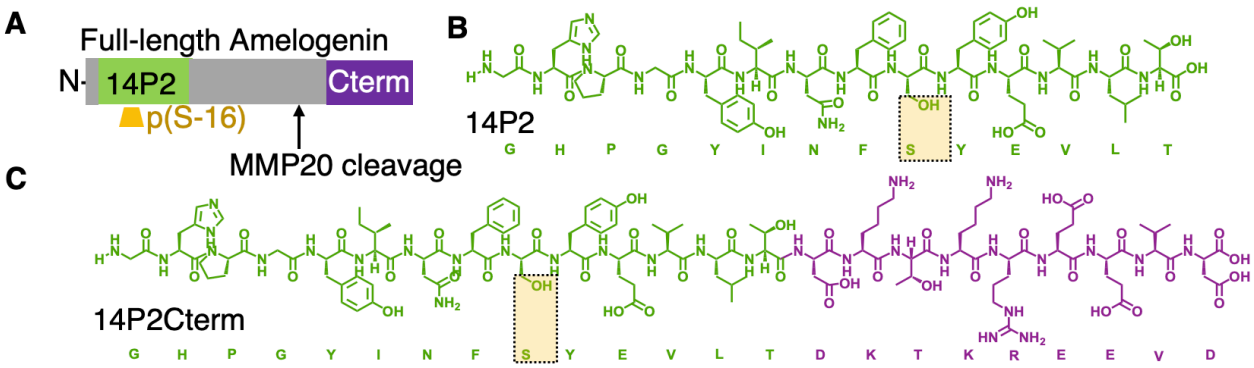

Figure 2.5. Sequences of full-length *Amel* and peptide analogs used in our study[120]. (a) Location of functional domains in human amelogenin, **(b)** self-assembling 14P2 domain, **(c)** 14P2Cterm (14P2 appended with truncated C-terminus, which is important for AP binding).

2.3 MINERAL-FREE SELF-ASSEMBLY METHOD

All solutions were prepared in polypropylene microcentrifuge tubes (Eppendorf and Ted Pella, Inc, USA). Lyophilized peptide or protein was dissolved in 10 mM HCl pH 1.94 (37 wt.% HCl in H_2O, 99.999% trace metals basis, Sigma-Aldrich CAS:7647-01-0 diluted with ultrapure DI water purified by MilliQ Elix Essential 3 and Advantage A10). Solutions were vortexed and

sonicated for 15-30 minutes in a Branson ultrasonic bath (M5800H, 40 kHz frequency) until a clear stock solution is obtained. For all AFM experiments, the stock solutions were 1 mg/mL in concentration: molarities of 626.2 μM for 14P2, 596 μM for p14P2, 370.75 μM for 14P2Cterm, 360 μM for p14P2Cterm and 50.08 μM for rH174. Solutions were further diluted immediately or aged and then diluted based on their application described below.

2.4 LARGE FILMS OF ALIGNED NANORIBBONS

2.4.1 *Sample preparation method*

1 mg/mL stock solutions were vortexed and used after 48 hours and up to 336 hours of incubation at room temperature (25 ºC). Aliquots of 0.1 mg/mL were diluted from the stock using 10 mM HCl (pH 1.94). 50 μL of 0.1 mg/mL solution was drop-cast on freshly cleaved HOPG ZYB quality (Ted Pella or Bruker) and incubated at 37 ºC in a sealed chamber (RH ~100%) for 12 hours for consistency with all samples. After incubation, solutions on HOPG were exchanged with 1 mM HCl (pH 3.1) first then H_2O, three times each, to remove unbound protein/peptide without disassembly.

For high-resolution AFM, dilute aliquots were prepared using freshly dissolved 1 mg/mL stock solutions and immediately used. 0.01 mg/mL was used for imaging R1 type NRs of 14P2 and other peptide sequences. While 0.05 mg/mL was used for R2 type NRs of 14P2 and 14P2Cterm

2.4.2 *AFM imaging method*

Self-assembled films on HOPG: For peptides, silicon nitride cantilevers with Si tip (Applied Nanostructures HYDRA4V-100NG, spring constant k: 0.088 N/m or Bruker SNL-10, spring constant k: 0.24 N/m or 0.12 N/m) were treated with UV/ozone for 15 minutes. Substrates

were placed on the AFM stage (MultiMode 8, Bruker), operated in tapping mode and surface was imaged in liquid at room temperature (25˚C). For imaging rH174, silicon tip cantilevers (Arrow UHF, NanoWorld) were treated with UV/Ozone for 15 min prior to performing high-speed tapping mode (5-10 Hz scan rate) on the Cypher VRS (Asylum Research).

High-resolution AFM: For peptides, silicon nitride tip cantilevers (Bruker, OTR4, spring constant k: 0.08 N/m or OTR8, spring constant k: 0.15 N/m) were plasma treated for 1 min before use to make them hydrophilic. Substrates were placed on the AFM stage (Cypher VRS, Asylum Research) and surface was imaged in liquid at room temperature (25˚C). Images of 14P2 R1 nanoribbons were obtained by drop casting the 0.01 mg/mL onto freshly cleaved HOPG (ZYB quality, Ted Pella or Bruker) surface and immediately imaged using tapping mode. Similar process was used for images of R2 nanoribbons with 0.05 mg/mL by using contact mode.

2.4.3 *Results*

With this protocol, all sequences were observed to assemble into NRs both in solution and on the surface of highly ordered pyrolytic graphite (HOPG) and remain stable in water (**Figure 2.6, A to E)** over a pH range of 1.94 - 7.4. While the NR dimensions for each sequence (**Table 2.1**) were distinct, the self-assembled NR films were similar in morphology, consisting of individual NRs or NR arrays with well aligned rows, though the film morphology was unclear in some areas.

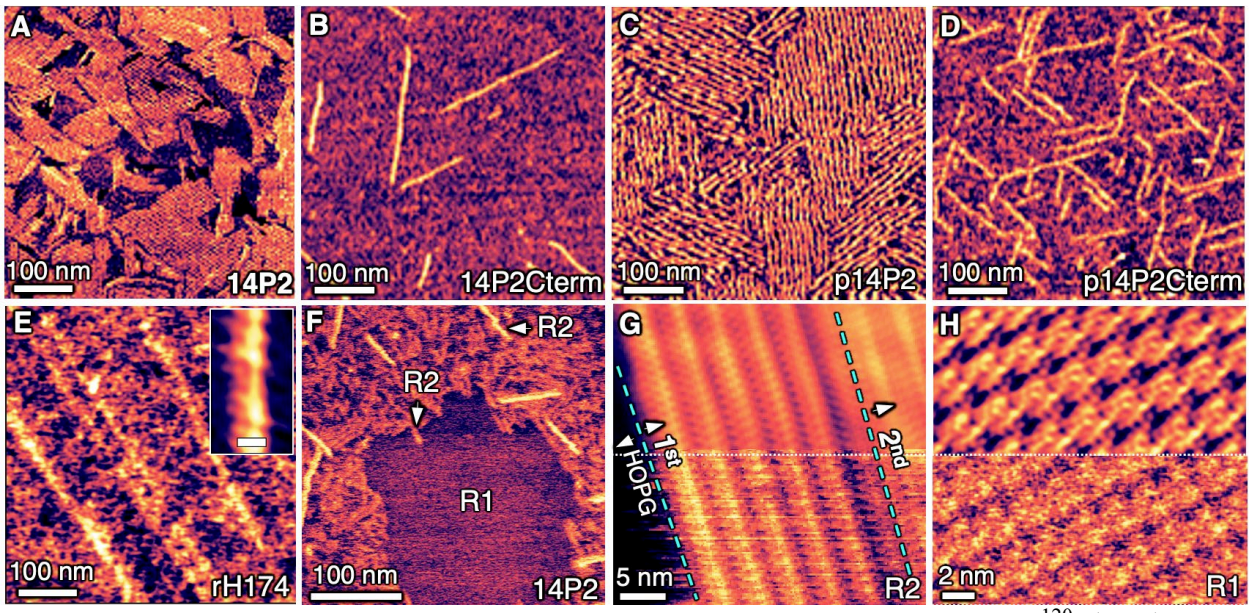

Figure 2.6. Assemblies of full-length *Amel* and peptide analogs on HOPG[120]. (**A-E**) *In situ* AFM images of ordered nanoribbons assembled on HOPG using 0.1 mg/mL diluted from 1 mg/mL aged for 48 hours and characterized in pure water: (**A**) 14P2; (**B**) 14P2Cterm; (**C**) and (**D**) phosphorylated versions p14P2 and p14P2Cterm, respectively; (**E**) recombinant full-length Amel, rH174; inset shows higher magnification of ribbon structure reconstructed using 2D Fast-Fourier Transform-filter, scale bar is 10 nm. (**F**) *In situ* AFM on HOPG in fresh 0.01 mg/mL solution of 14P2 at pH 1.94 reveals 100% coverage with multiple layers: two types, R1 and R2. (**G**) Structure of R2 in fresh 0.05 mg/mL solution of 14P2 solution at pH 1.94; dashed blue lines delineate the boundary of a second layer over the first on HOPG. (**H**) Structure of R1 in indicated region of (F). (G) and (H) bottom: original image; top: after reconstruction with 2D Fast-Fourier Transform-(FFT)-filter.

Table 2.1. Dimensions of NRs measured from *in situ* AFM images shown in **Figure 2.6** and **Figure 2.8**. Error is Std. dev., n≥5.

Sequence	NR type	Height (nm)	Width (nm)
14P2	R2 R1	0.65 ± 0.04 0.33 ± 0.07	5.81 ± 0.60 2.51 ± 0.47
p14P2	R2 R1	1.11 ± 0.1 0.75 ± 0.08	7.57 ± 0.5 3.64 ± 1
14P2Cterm	R2 R1	0.67 ± 0.08 0.30 ± 0.04	6.16 ± 1.51 3.53 ± 0.36
p14P2Cterm	R2 R1	1.36 ± 0.26 0.82 ± 0.05	9.35 ± 1.24 4.08 ± 0.36
rH174	R2	0.63 ± 0.05	15.00 ± 2.10

Higher magnification analysis of the baseline sequence 14P2 showed that, at sufficiently high concentration (fresh 0.01 mg/mL solution), HOPG was indeed completely covered,

supporting NR layers of two types, referred to as R1 and R2 (Figure 2.6 F), both of which were in direct contact with HOPG. Of the two, R2 was by far the dominant morphology and formed multiple layers at sufficiently high concentration (≥ 0.05 mg/mL) without any involvement of R1 NRs (Figure 2.6 G). In contrast, R1, which was rarely observed for the peptides and never observed for rH174, only formed single highly crystalline layers and was only observed at concentrations ≤ 0.01 mg/mL (Figure 2.6 H). In all cases, the NRs were aligned with the three HOPG <$10\bar{1}0$> directions (**Figure 2.6 C** and **Figure 2.7**).

Because all mineralization experiments were performed with R2 NRs, further discussion of NR structure is restricted to this type, though basic morphological information on the R1 layers can be found in Table 2.1 and Figure 2.8. The width and height of peptide R2 NRs ranged from 5.81±0.60 nm to 9.35±1.24 nm and 0.65±0.04 nm to 1.36±0.26 nm, respectively, depending on the sequence (**Table 2.1**). For rH174, the measured R2 NR width and height were 15 ± 2.1 nm and 0.63 ± 0.05 nm, respectively. (Note that a 0.5-1.0 nm spread in dimensions measured on soft matter, particularly for features below 2 nm, is common due to variations in tip-sample interactions)

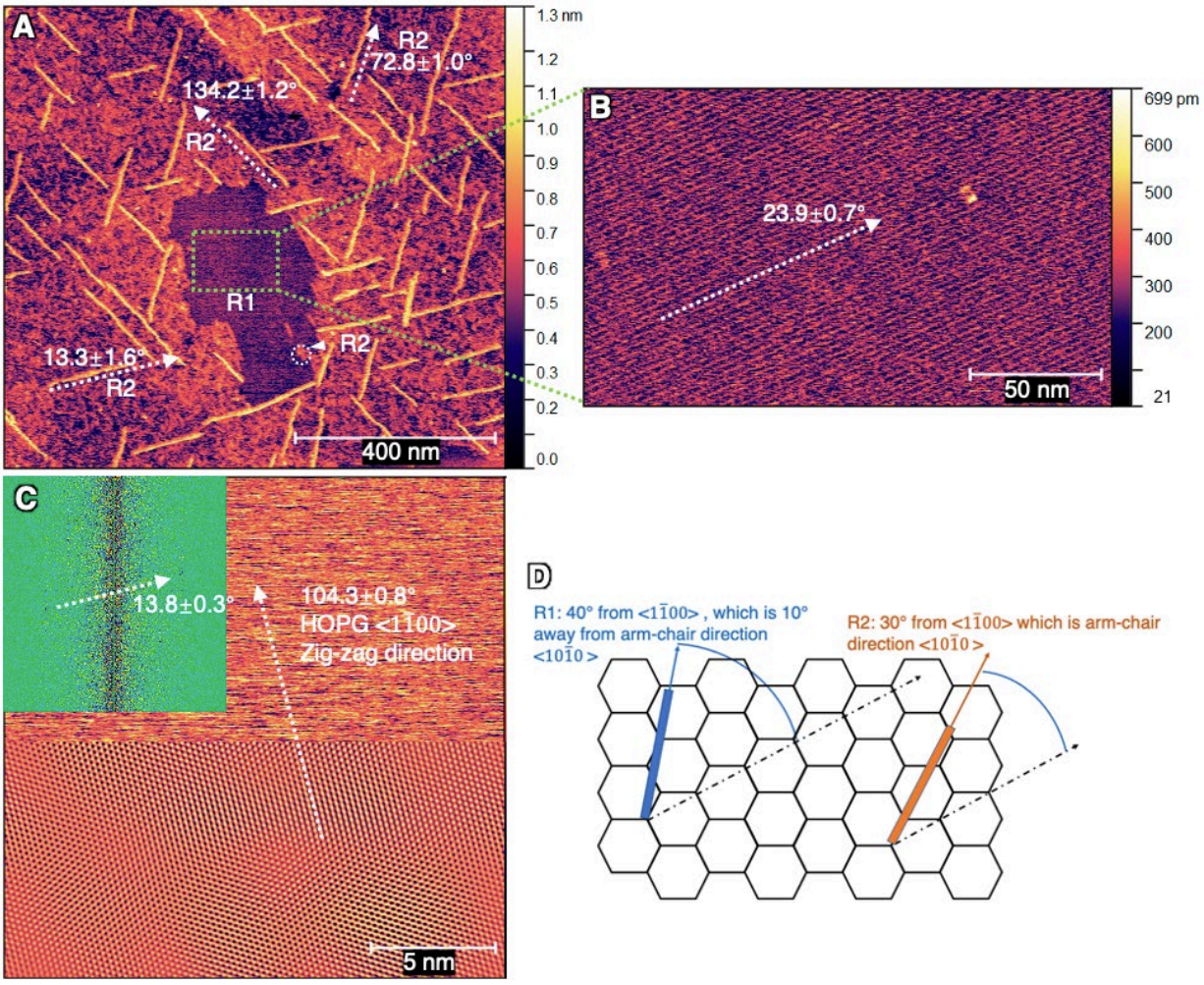

Figure 2.7. Orientation of R1 and R2 NRs with respect to underlying HOPG (0001) from in situ AFM images of 14P2 using 0.01 mg/mL from freshly prepared 1 mg/mL stock solution (Fig. 1I)[120]. (**A**) Multiple layers are visible, white arrows indicate relative direction of R2 NRs which lie on the arm-chair direction, <10$\bar{1}$0> (~13.3˚), darkest area in the center consists of R1 NRs as seen in (B). (**B**) R1 NRs and direction relative to graphite lattice, (**C**) Top half is AFM image of underlying HOPG substrate collected after scratching the top layer with contact mode AFM and bottom half is the reconstructed image with noise removed by 2D-FFT filter using points shown in FFT inset indicating the zig zag direction <1$\bar{1}$00>. (**D**) R1 NRs lay 10˚ away from direction R2 NRs (arm-chair direction <10$\bar{1}$0>).

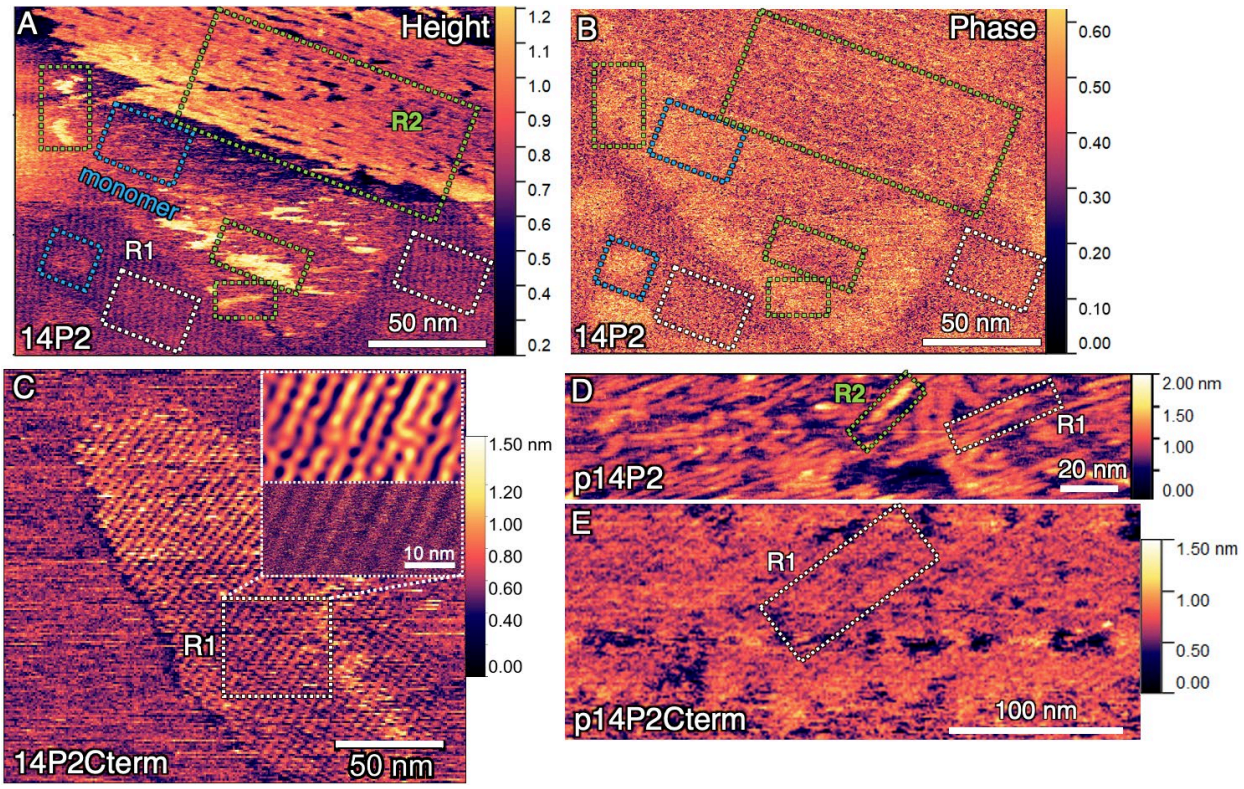

Figure 2.8. *In situ* AFM images of R1 NRs on HOPG for 14P2, 14P2Cterm, p14P2 and p14P2Cterm with low peptide concentrations (≤0.01 mg/mL, fresh solutions)[120]. (**A** and **B**) Representative data of 14P2 showing the method for identifying NR type from height and phase contrast data. Green boxes are R2 NRs which have a darker phase contrast and larger thickness (brighter features in height), white boxes are R1 NRs that also show a dark contrast but with roughly half the width as R2 NRs, and blue shows amorphous structures or monomers (brightest features in phase images) bind to the surface. (**C**) 14P2Cterm R1 NRs with inset showing molecular resolution image of R1 NRs where bottom half is original image and top half with noise removed using 2D-FFT filter, **(D)** p14P2 R1 and R2 NRs and **(E)** p14P2Cterm R1 NRs.

The dimensions of the R2 NRs are consistent with those of the β-sheet precursors of cross-β-sheet NRs. At 0.5-2.0 nm, their thickness is roughly half that of cross-β-sheets depending on the sequence investigated and the AFM substrate and imaging parameters used [95,121,122]. Because β-sheet NRs typically have a hydrophilic and hydrophobic interface on opposing faces, they self-assemble in an anti-parallel fashion on the two hydrophobic interfaces to form the cross-β-sheet structure, which is the motif exhibited by the Amel NRs observed *in vivo*. Here, the HOPG surface is expected to provide one of the hydrophobic surfaces, leading to formation of β-sheet NRs rather

than cross-β-sheets, but maintaining the same NR-solution interface as obtained with cross-β-sheet ribbons.

The similarity between the structure and homology of NRs assembled at pH 1.94 and those of previously reported Amel NRs assembled at various pH values, as well as their integrity upon binding to HOPG, was further assessed by a combination of AFM and MD simulations, supported by in situ synchrotron X-ray Diffraction (XRD).

2.5 Evaluation of self-assembled NRs on HOPG

Based on observations from previous reports of amyloid self-assembly at acidic pH and assembly on HOPG [92,117], we evaluated the self-assembly of single β-sheets NRs of 14P2 at pH 1.94 in solution and on HOPG and compared the results at pH 3.1. Films of 14P2 NRs on HOPG assembled at pH 1.94 were then assessed for any structural changes during binding and exchange to phosphate buffer at pH 7.4. Self-assembly of rH174 NRs on HOPG was also studied. The methods and results are discussed below.

2.5.1 *Method*

1 mg/mL (626.29 μM) solutions of 14P2 at pH 1.94 and 3.1 were prepared according to the mineral-free self-assembly protocol and incubated at room temperature (25 ºC). Silicon Nitride cantilever with Si tip (Applied Nanostructures HYDRA4V-100NG, spring constant k: 0.088 N/m or Bruker SNL-10 C, spring constant k: 0.24 N/m or 0.12 N/m) were treated with UV/ozone for 15. A freshly cleaved HOPG surface was first imaged under pH 1.94 or 3.1 water without peptides. After confirming that the surface is clean, the stock solutions were vortexed for 3 seconds and

aliquots for imaging were withdrawn at the specified times then diluted to 0.1 mg/mL (62.6 μM). 100 μL of 0.1 mg/mL (62.6 μM) solution was immediately introduced onto HOPG and imaged.

For imaging self-assembly of rh174 β sheets on HOPG, 0.0001 mg/mL (5 nM) solution of rH174 at pH 1.94 was diluted from freshly prepared 1 mg/mL solution using the mineral-free self-assembly protocol. Silicon tip cantilevers (Arrow UHF, NanoWorld) were treated with UV/Ozone for 15 min prior to performing high-speed tapping mode (5-10 Hz scan rate) on the Cypher VRS (Asylum Research). A freshly cleaved HOPG surface was first imaged under pH 1.94 water. After confirming that the surface is clean, 30 uL of freshly made 5 nM rH174 solution was introduced onto HOPG and imaged.

2.5.2 *14P2 R2 NR self-assembly at ph 1.94 and 3.1*

Both 14P2 solutions, pH 1.94 and 3.1, deposited multiple layers of NRs with width ~5.8 nm and ~0.65 nm height on HOPG matching R2 NR dimensions (**Figure 2.9**). Length measurements were performed on the topmost layer. The bottom layers may have longer NR, but the features were not clearly distinguishable for measurements at 2 μm x 0.5 μm scan size. For both pH, the smallest NR length at all time points was 10 nm, observed around 100 hours. The largest length (>90 nm) was observed at 313 h for pH 1.94 (solid black line in Figure 2.9 C).

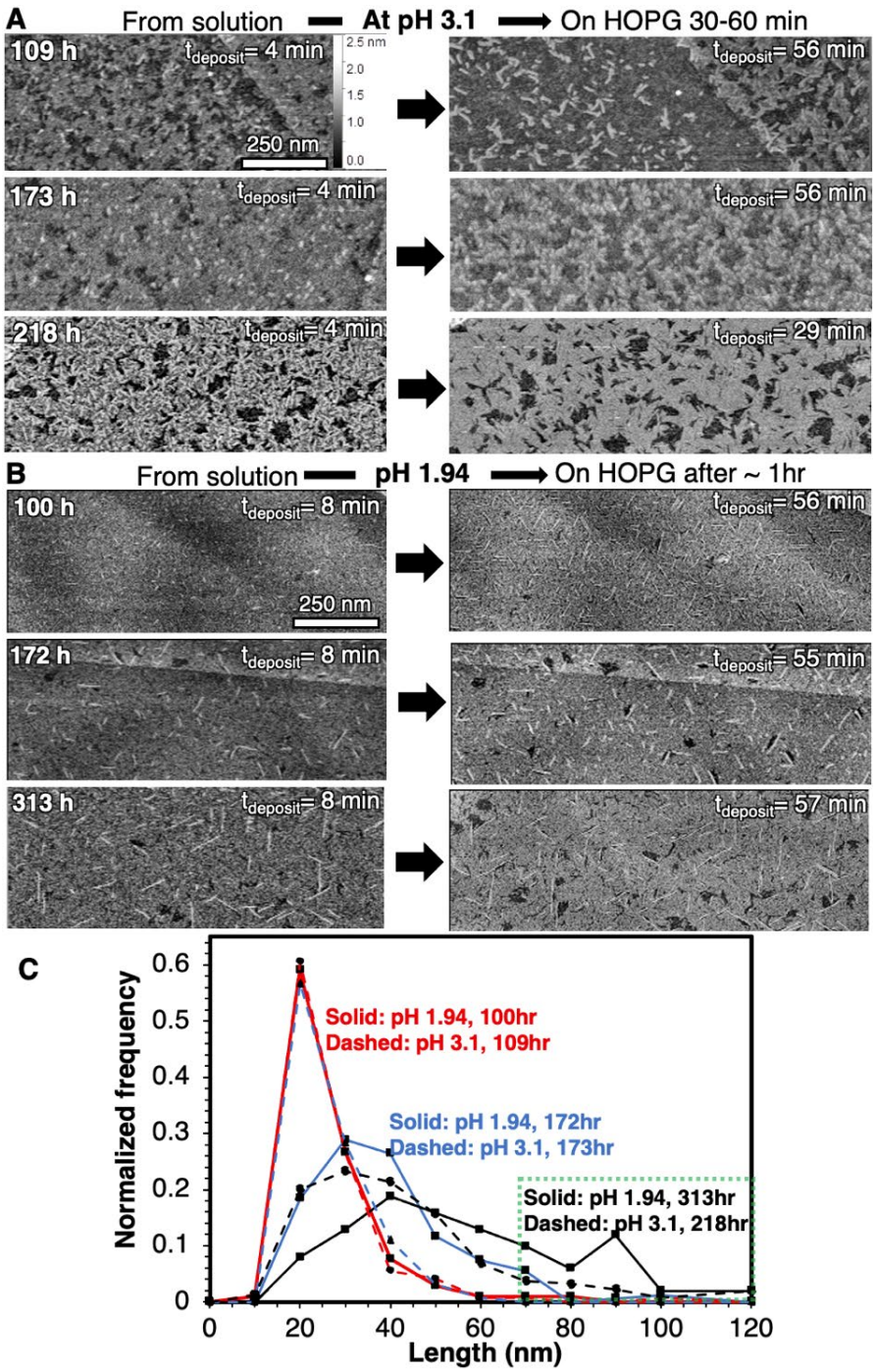

Figure 2.9. Self-assembly of single β sheet 14P2 NRs at pH 1.94 and pH 3.1 at similar time points characterized by in situ AFM on HOPG. $t_{deposit}$= 0 min is defined as the moment the solution is introduced into the AFM flow cell. Aliquots of 1 mg/ml 14P2 solutions at (**A**) pH 3.1 and (**B**) pH 1.94 are taken out, diluted to 0.1 mg/ml, introduced into the AFM liquid cell and imaged immediately (left column), and 30-60 min after initial deposition (right column). (**C**) In all cases, the NRs grew in length over time in solution and on HOPG. The longest NRs were seen with pH 1.94 at 313 h (solid black line in dotted green box). A broadening of the length distribution and shift towards the right (higher length) is also observed.

At pH 1.94, stock solutions from different time points show that the lengths of the NRs increase over time (Figure 2.9 B; 100, 172 and 313 hours), which further grew in length when incubated on HOPG for 30-60 min. The assembly process at pH 1.94 and ~170 hours at higher magnification is shown in **Figure 2.10 A**. The pH 3.1 stock solutions also had ~10 nm NRs at 100 h, however, longer incubation of the stock resulted in NRs that were shorter than those at pH 1.94 at similar time points (Figure 2.9 A). NRs at pH 3.1 also grow in length within ~1 hr of deposition on HOPG.

The above results demonstrate identical NRs self-assemble in solution and on HOPG and that self-assembly is enhanced both at pH 1.94 and by HOPG surface. Therefore, we conclude the assembly can be controlled using pH and incubation time in bulk or on HOPG, as observed in other amyloid studies [117,118]. Additional spectroscopic characterization with techniques such as in situ tip-enhanced Raman or solid-state NMR may provide more structural information. However, current techniques are unable to detect a strong signal for peptides on graphite using in situ conditions and requires further advancements in technology or expensive peptide labels. Instead, we employed synchrotron XRD.

2.6 Self-assembly dynamics and integrity on HOPG

Assembly and integrity of R2 NRs of 14P2 and rH174 assembled at pH 1.94 were further investigated at higher magnification (**Figure 2.10**). For 14P2, 50 µL of pH 1.94 0.1 mg/mL (62.6 µM) solution, diluted from 1 mg/mL (626.29 µM) stock solution aged for 170 h (~7 days), was injected into the liquid cell. After the system equilibrated, the imaging medium (10 mM HCl) was exchanged with water, observed for any changes, then exchanged with 9.5 mM KH_2PO_4 at pH 7.4 to monitor any structural changes in the protein films at different pH. Analysis of the height, width

and phase signal showed no changes other than reorganization (Figure 2.10A). *In situ* AFM observations of 5 nM rH174 solutions also demonstrated that single β sheet NRs assemble over time on HOPG (Figure 2.10 B to E).

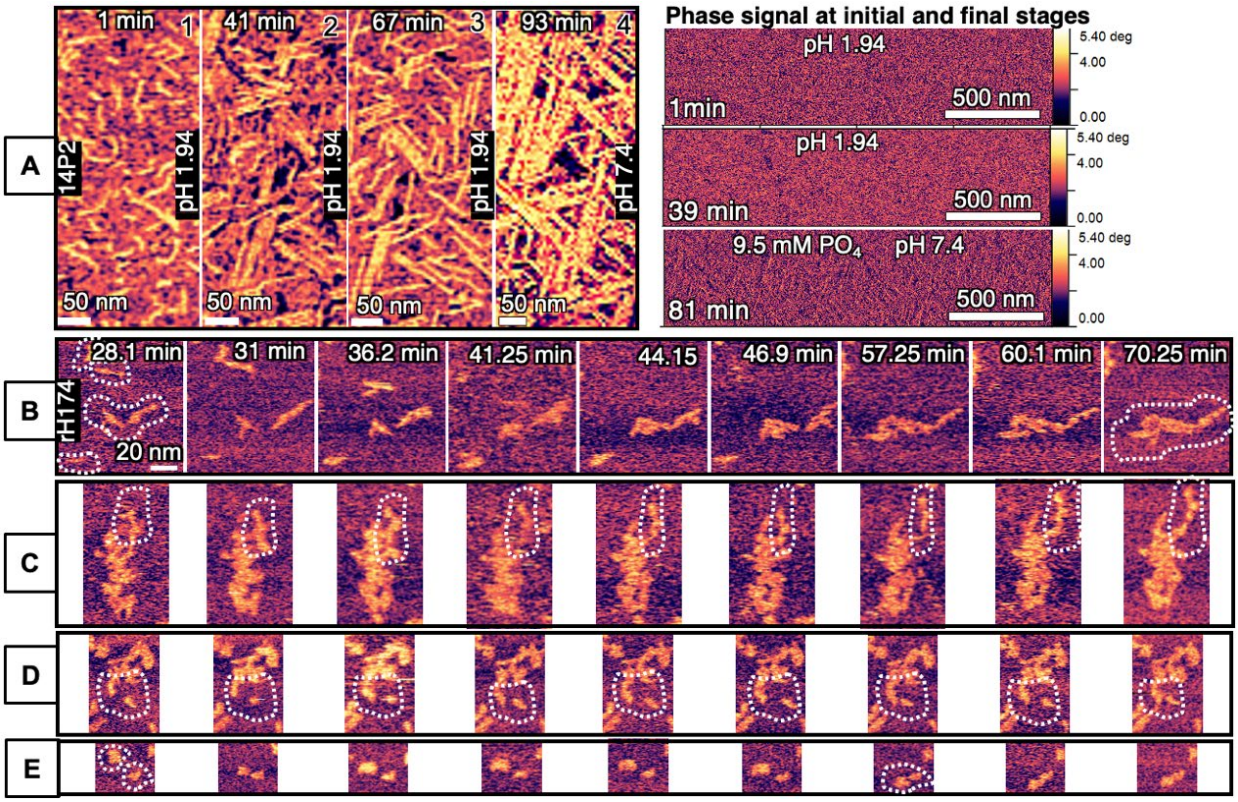

Figure 2.10. Time-lapse of *in situ* AFM images for nanoribbon self-assembly in 10 mM HCl on HOPG. (**A**) for 14P2 using 1 mg/ml (62.63 μM) solution (aged in bulk for 7 days) and adsorbed onto HOPG. Left four panels show height image and right three panel shows phase images when ribbons are imaged within 1 min of introducing the solution, 39 min later, and when the buffer is switched to 9.5 mM PO_4 pH 7.4. All panels demonstrate ribbons undergo no visible changes in physical dimensions (height and width) and internal and surface structure-related properties (phase contrast), other than rearrangement of NRs, from the point of binding to HOPG, epitaxial alignment, packing into islands and pH change. (**B - E**) Self-assembly of rH174 NRs in contact with HOPG at pH 1.94 using 5 nM freshly made solution. (B) 5 nanoribbons come together by elongation or side-by-side modes. (C) Growth of nanoribbon highlighted in circled area. (D) Smaller nanoribbon meets the end of a larger structure, recedes away and come together again to join the large structure. (E) another instance of attraction, repulsion, reorientation and fusion seen in (d). Width of rH174 nanoribbons is ~16.3 nm. Scale bar is the same for (B) to (E) and snap shots in the same columns have the same time scales.

2.7 STRUCTURE BY *IN SITU* SYNCHROTRON X-RAY DIFFRACTION

2.7.1 *Method*

Protein/peptide solutions were prepared according to the mineral-free self-assembly protocol using higher concentrations to increase the XRD signal to noise ratio. Concentrations were 1 mg/ml (626.90 μM) for 14P2, 1.5 mg/ml (894.9 μM) for p14P2, 4 mg/ml (1.48 mM) for 14P2Cterm, 4.5 mg/ml (1.62 mM) for p14P2Cterm and 2 mg/ml (100.17 μM) for rH174. The stock solutions were aliquoted to prepare two samples, one with Amel NR adsorbed on graphite and the other without graphite. To prepare suspensions containing graphite, 1-2 mm size freshly cleaved HOPG flakes were added to the freshly prepared stock solution aliquot then sonicated for an additional 30 min to disperse and exfoliate the HOPG flakes into smaller fragments for increasing the surface area and adsorption amount for Amel NRs. Both, with and without graphite, aliquots were then aged for 14 days and vortexed prior to use.

A 5 μl droplet of solution with or without graphite was drop cast onto the XRD mesh (M3-L18SP-10 MicroMesh or M7-L18SP-50 MicroGripper; MiTeGen, USA) and incubated for 40 minutes, then the excess solution was gently wicked away to leave a film covering the whole sample holder loop (**Figure 2.11**). Measurements were performed within 5 minutes of preparation to avoid dehydration and repeated at least three times. Powder diffraction measurements were performed with 0.11159-nm synchrotron radiation at Beamline 8.3.1 of the Advanced Light Source at Lawrence Berkley National Laboratory.

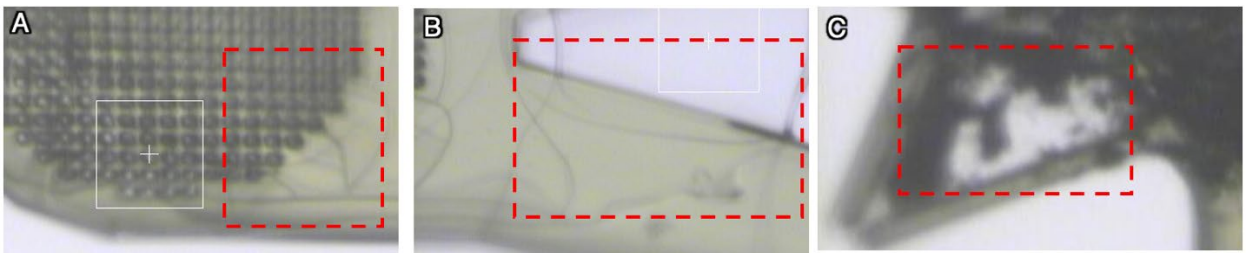

Figure 2.11. Hydrated thin film of protein/peptide solutions suspended on XRD sample loops. Optical micrographs from the beamline show samples without graphite (A and B) and with graphite (C).

The 2D diffractograms were first converted into 1-D d-spacing scans by radial integration using FIT2D software. Due to low signal to noise ratio, background subtraction was performed with FullProf software using two baselines, one from the sample due to water and second from a blank sample with comparable exposure time and detector distance to identify the nanoribbon peaks. These two controls identified the prominent peaks from the protein or peptide samples. Subsequently, the background signal was subtracted for each sample spectrum to get the refined spectrum.

2.7.2 *Additional characterization of XRD samples by AFM and TEM*

HOPG as substrate was used to deposit the constituents of the protein/peptide and graphite suspension **(Figure 2.12**). In situ AFM demonstrated neither sonication nor HOPG negatively impact assembly of NR as observed by the formation of aligned islands of NRs on the HOPG substrate **(Figure 2.12 A**) and presence of long NR closely associated with the dispersed graphite flakes from bulk solution (**Figure 2.12 B**) in the same experiment. Further analysis of solutions containing graphite and 14P2 peptides by TEM of negatively stained samples shows a layer of organic material on the HOPG flake (**Figure 2.12 C**). HRTEM and FFT analysis (**Figure 2.13**) indicates NR has width 5.19 nm and 5.34 nm, which strongly match the R2 NR width of 5.8±0.6

nm observed by AFM, and weak 0.47 and 2 nm which match 0.47 nm d-spacing by XRD, MD and AFM of the β-sheet structure and the ~ 2 nm periodicity in XRD and AFM, respectively.

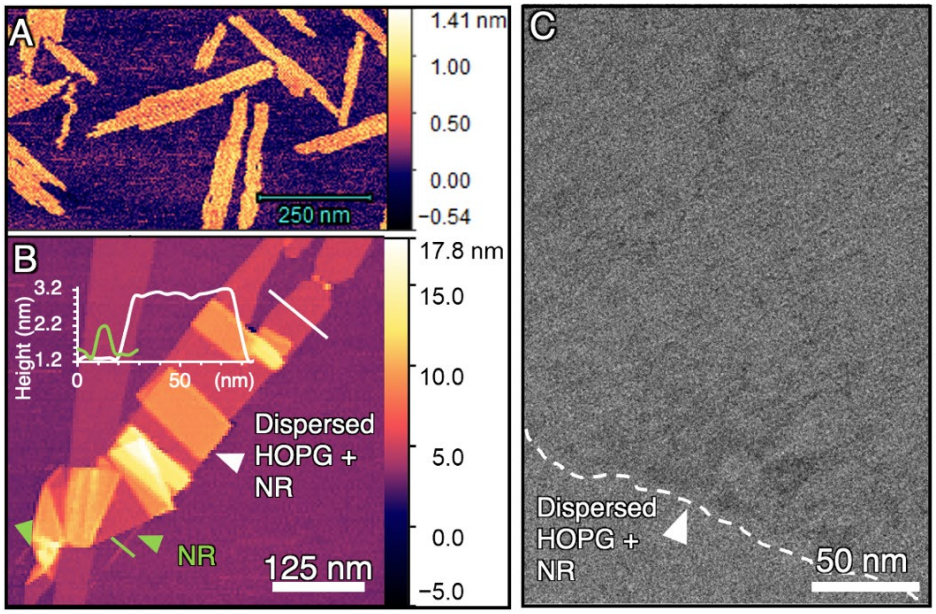

Figure 2.12. (**A** and **B**) *In situ* AFM analyses of peptide and graphite solution (14P2) on HOPG demonstrates the method assembles NRs in solution that (A) bind to freshly cleaved HOPG as well as (B) generates 2-3 nm thick graphite sheets closely associated with ~1 nm thick NR in the same experiment. (**C**) Negative-stained TEM analysis of a 14P2 solution used for XRD shows a thin organic layer adsorbed on graphite.

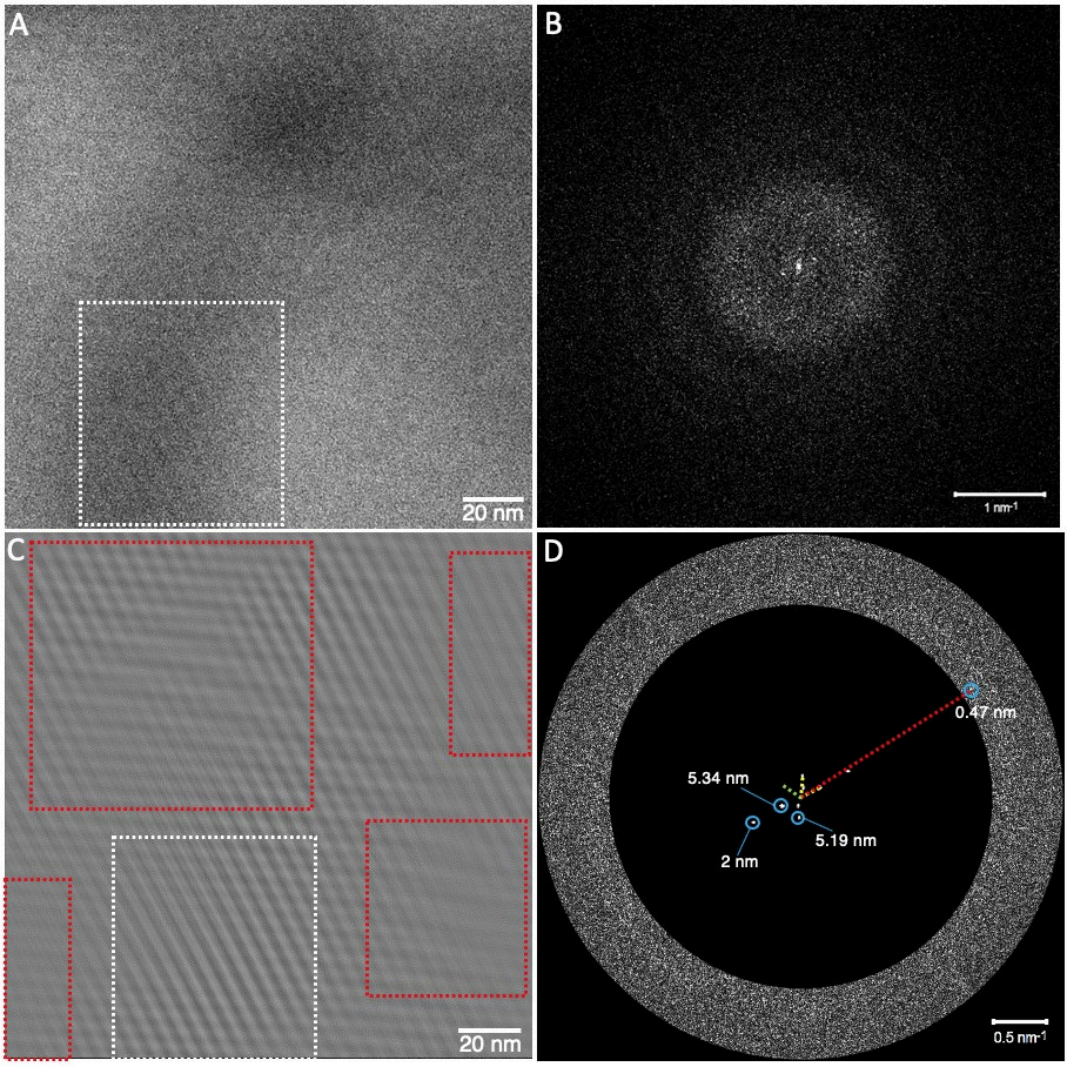

Figure 2.13. HRTEM and FFT analysis of negative stained nanoribbons. (A) Negatively stained TEM image of single β-sheet 14P2 R2 NR on graphene grid. **(B)** Raw FFT of (A). **(C)** Inverse-FFT obtained using **(D)** noise filtered FFT. White dotted box in (A) and (C) highlight the magnified area shown in previous version of SI. Red boxes in (C) indicate areas with features in directions different to those in the white box. Yellow lines in (D) highlight 60º angle between the two clear reflections, green line highlights the missing orientation of NRs and red line highlights the 105º (or 70º) angle with the missing orientation. Analysis shows presence of NRs with width 5.19 nm - 5.34 nm (blue circles), which closely matches the 5.8±0.6 nm width observed by AFM.

2.7.3 *XRD results and discussion*

Previous analysis of the cross-β-sheet structure of amyloid ribbons by X-ray Diffraction (XRD) show that the dominant diffraction peaks lie at d-spacings of ~0.47 nm and ~1 nm [65,88,92,106].

~0.47 nm correlates to the distance between monomers arranged in parallel (-N-N-N-…terminals) in the β-sheet backbone due to hydrogen bonding that resembles a tape or ribbon structure, while ~1 nm stems from the distance between two β-sheets in an antiparallel steric zipper conformation with N-termini of one sheet facing C-termini of the second and separated by a hydrophobic interface. A previous study also investigated the amyloid-like, cross-β-sheet of amelogenin and demonstrated that the 14P2 domain has a high propensity to form β-sheets in solution [81]. Subsequent solid-state Nuclear Magnetic Resonance (ssNMR) and XRD studies performed on the LRAP segment of murine amelogenin (contains 14P2 except for F replaced with L), confirmed the presence of β-sheet structure within the 14P2 domain [106]. The NRs of all sequences prepared using our protocol exhibit similar diffraction patterns in bulk solution (at concentrations ≥1 mg/mL and aged for 14 days) with and without HOPG, thus confirming the absence of other periodic conformations such as α-helix (**Figure 2.14)**. The structures in these solutions were further characterized using *in situ* AFM, detailed below. Muscovite mica, a charged hydrophilic surface, was also employed to compare the effect of surface chemistry on NR orientation.

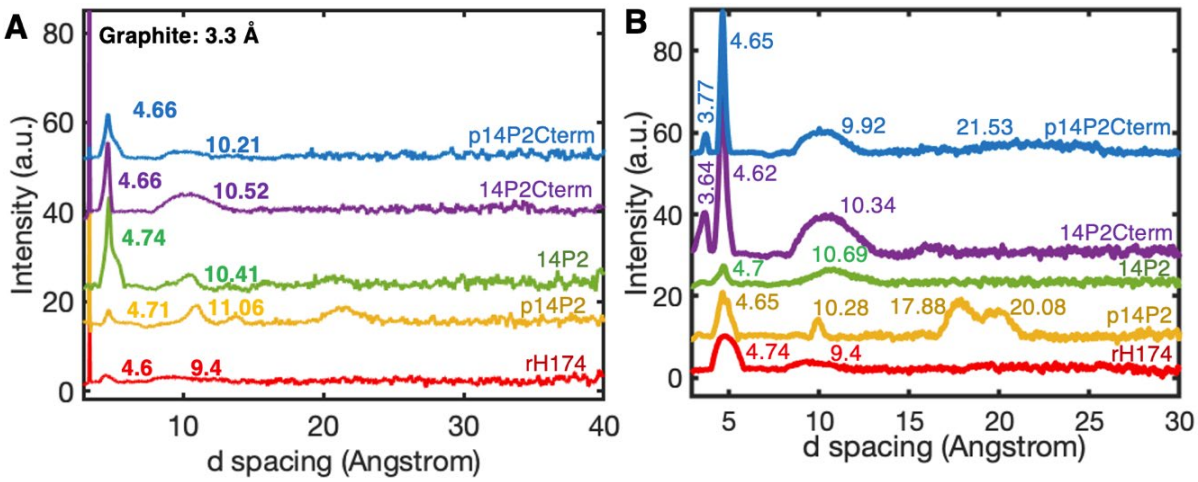

Figure 2.14. In situ XRD patterns of Amel (rH174) and derived peptide analogs in 10 mM HCl (pH 1.94) aged for 14 days [120]. (**A**) in presence of graphite prepared by using peptides as an adsorbate on HOPG and (**B**) without graphite.

2.7.4 *Method to identify supramolecular structures in XRD samples*

Using 14P2, solutions typically used for XRD (≥1 mg/mL, pH 1.94, aged for 14 days) and those used for mineralization experiments (0.1 mg/mL, pH 1.94, aged for 14 days then diluted to 0.1 mg/mL) were deposited on muscovite mica and HOPG to determine the composition and impact of surfaces on NR assembly, orientation and dimensions (**Figure 2.15**). Identical method was used to avoid sample preparation artifacts. 30 μL of the solution was drop cast onto the substrate (HOPG or muscovite mica) and left to incubate for 1 hour in a sealed chamber. After incubation on the substrate, the excess solution was carefully removed and exchanged with pure water then immediately characterized using *in situ* AFM.

2.7.5 *Supramolecular structure characterization by AFM on HOPG and mica*

1 mg/ml solutions of 14P2 aged for 14 days contained NRs with thickness 3-4.5 nm when deposited on muscovite mica or HOPG (**Figure 2.15 A and B).** The height and width had large variations due to aggregation of the multiple ribbons and non-specific binding, but the smallest width observed was ~6 nm and height was ~ 3 nm which match the dimensions of cross-β sheet 14P2 NRs previously prepared in physiologically relevant conditions [81]. In addition to cross-β sheet NRs, the solution also deposited NRs with thickness ~0.65 nm on HOPG or ~1.7 nm on muscovite mica seen in the background, however no ordered islands of aligned NR were observed, likely due to oversaturation of surface with proteins.

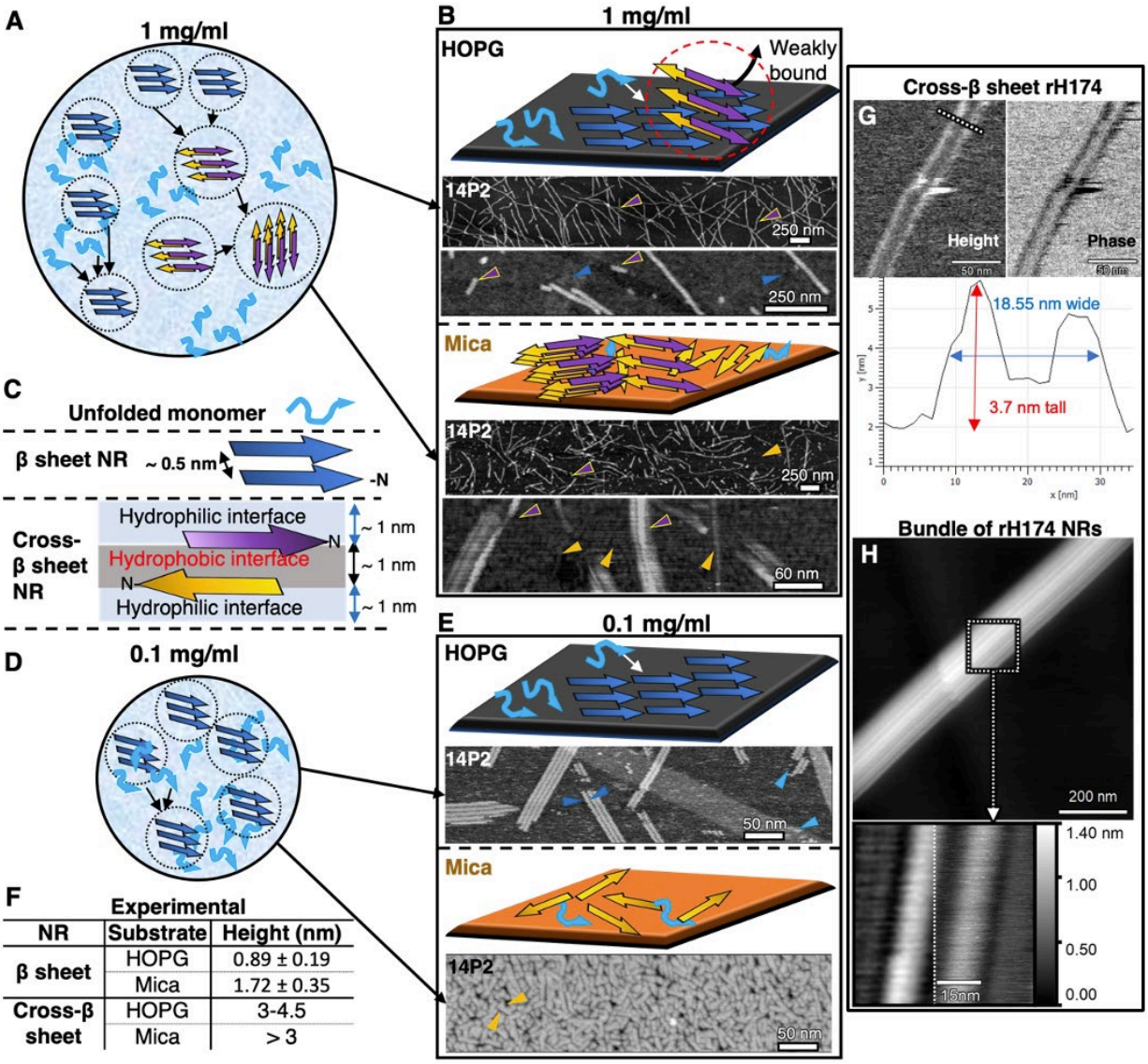

Figure 2.15. Schematic describing the composition of typical protein solutions containing NRs self-assembled at different concentrations at pH 1.94 and impact of surfaces monitored by *in situ* AFM [120]**.** Arrow color legend: Light blue - monomers; Dark blue - single β-sheet; Yellow: single β-sheet with hydrophilic interface facing mica; Yellow and Violet: Cross-β-sheet (**A**) Cartoon of the constituents in high concentration solutions (1 mg/ml or more), as seen in (**B**) for 14P2 (1 mg/ml or 626.29 µM, aged for 14 days) on HOPG and muscovite mica. (**C**) Legend of various features observed in (B and E) and their expected configuration. (**D**) Cartoon of the constituents in low concentration solutions (0.1 mg/ml or less), as seen in (**E**) for 14P2 (0.1 mg/ml or 62.63 µM, aged for 14 days) on HOPG and muscovite mica. (**F**) Comparison of typical heights from AFM expected for various 14P2 structures on HOPG and mica. (**G**) Morphology (top left panel), phase contrast (top right) and height profile (bottom panel) of rH174 cross-β-sheet NR from 0.0001 mg/ml solution that matches reported AFM and TEM structure [64] and (**H**) bundled NRs ~15 nm wide observed in 0.1 mg/ml solution (area to the left of dotted line is 2D-FFT Filtered); both were freshly diluted from 1 mg/ml stock aged for 7 days.

In contrast, 0.1 mg/ml concentration solutions diluted from 1 mg/mL aged for 14 days mainly deposited NRs with thickness ~0.65 nm on HOPG or ~1.7 nm on muscovite mica **(Figure 2.15 D and E**). Furthermore, these NRs assembled into highly aligned islands by binding on HOPG (0001) surface epitaxially, in the three symmetrical directions, similar to other β-sheet amyloids previously reported 135. Whereas mica had no direct evidence of assembly using our protocol. These NRs with thickness roughly half of cross-β sheet NR are generally characterized as protofibrils with β sheet structure that dimerize or aggregate in anti-parallel configuration to form cross-β sheet NR by binding of the hydrophobic interfaces as shown in **Figure 2.15 C** [95,121,122,124]. This process generates a 'dry' core and a hydrophilic 'wet' exterior in cross-β sheet NR. The variation in height on mica vs. HOPG for single β sheet NR further confirms this **(Figure 2.15 F**); binding of the hydrophilic side of the single β sheet NR likely traps water between mica and NR, thus increasing the apparent height. Whereas binding of the hydrophobic side of single β sheet NR excludes water to create a dry interface between HOPG and NR, and the π-π interactions with HOPG may further reduce the overall height. These observations of single β sheet NR assembly on HOPG vs. mica show HOPG surface can act as a proxy for the buried hydrophobic interface of the cross-β-sheet dimer similar to previous studies on amyloids 136,138. Cross-β sheet NRs and bundles were also observed at 0.1 mg/ml in other data but they were relatively low in number and easily desorbed during buffer exchange (rinsing).

The above findings were also observed for other sequences as well, including rH174, though a detailed investigation was not performed since the XRD results demonstrated there are NRs in 1 mg/mL solutions and single β sheet NR assembled on HOPG with 0.1 mg/mL solutions. For e.g., rH174 solutions diluted from high concentration stock solutions (1 mg/ml aged for at least

7 days) consistently showed presence of cross β-sheet NRs (17.55 ± 0.6 wide and 4.045 ± 0.28 thick) as shown in Figure 2.15 G and bundled NRs, in addition to single β-sheet NRs, on HOPG as shown in **Figure 2.15 H** which were similar in morphology of NRs prepared in physiologically relevant conditions obtained through negatively stained TEM and AFM [64,65,81,86,88,89,106].

2.8 STRUCTURE BY HIGH-RESOLUTION AFM

Periodic features observed in the AFM images of 14P2 R1 and R2 were analyzed by radial integration of the noise filtered Fast Fourier transform (FFT) patterns and topography (**Figure 2.16 A and G**). Instrument generated noise was filtered out by masking the high intensity points in the raw FFT **(Figure 2.16 B and H)** and subtracting the background using 2D FFT-Filtering on Gwyddion (**Figure 2.16 C**). Subsequently, 2D FFT was performed on these 2D FFT-filtered images to generate the noise-filtered FFT patterns **(Figure 2.16 D and J**). The noise filtered FFT patterns were then radially integrated using the Radial Profile plugin with spatial calibrations on Image J/Fiji (NIH) and converted to real-space (in nm) using $V(r) = 1/r_{INT}$, where r_{INT} is the reciprocal distance from the center (**Figure 2.16 F and K**). The peak positions were identified by fitting using the Peak Analyzer tool on OriginPro software.

Sharp peaks between 0.4-0.65 nm were clearly visible in Figure 2.16 F and K and identical to XRD pattern. The broad peak between 0.9-1.2 nm is not related to the cross-β-sheet structure since these are single β-sheets of R2 NR. For deconvolution of periodic features in the AFM topography, the high intensity spots in noise filtered FFTs were categorized into group 1 (~2 nm), group 2 (~1nm) and group 3 (~0.5 nm) (Figure **2.16** D and J). 2D FFT-filtering was performed again on the raw AFM data, but by masking combinations of the points marked in groups 1, 2 and 3 while subtracting the rest, until artifact-free features were generated (**Figure 2.16** E and I).

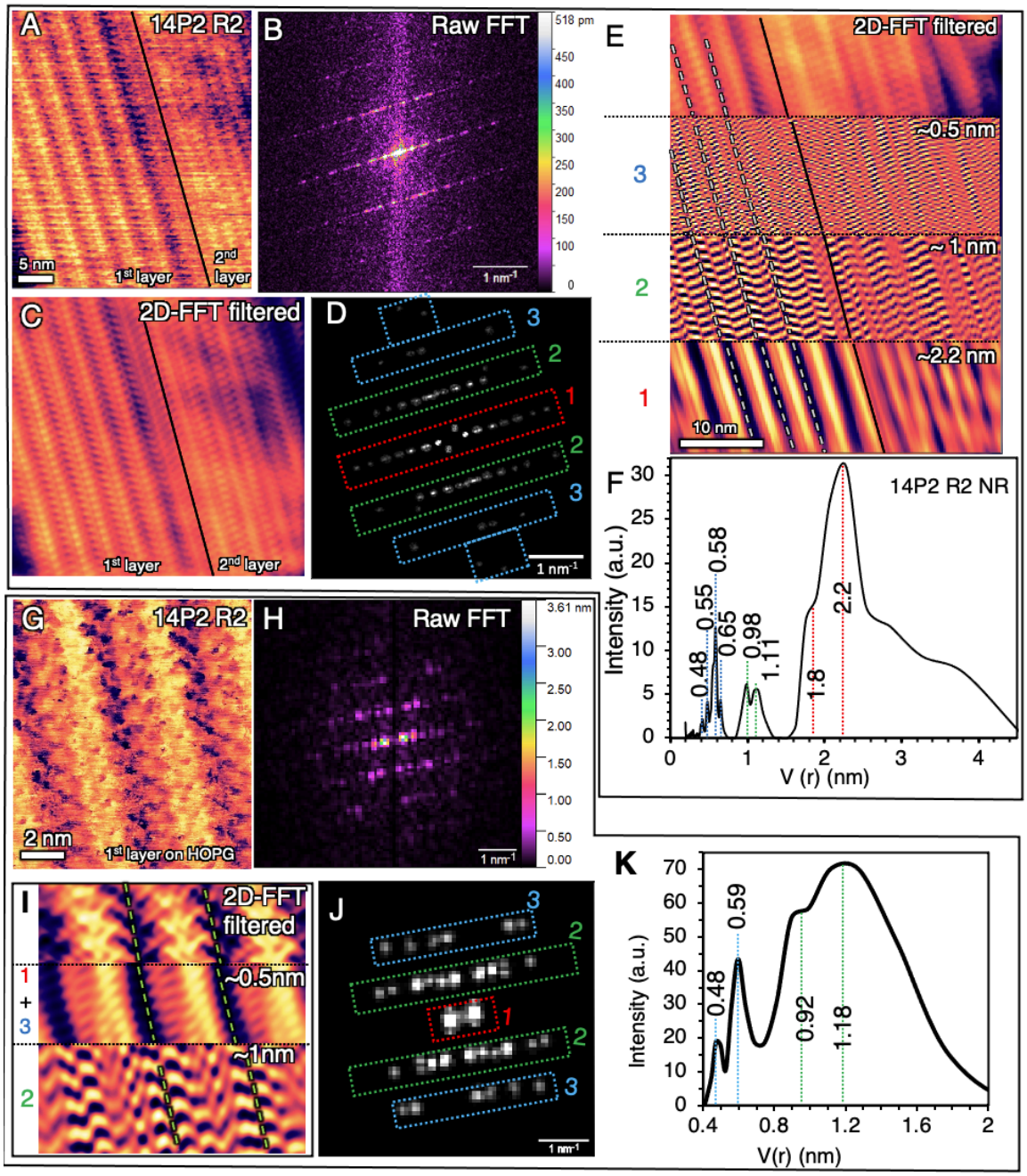

Figure 2.16. FFT analysis of prominent periodic features in 14P2 R2 structures from AFM. (**A** -**F**) first and second layer R2 NRs of 14P2, (**G**-**K**) Higher magnification of 1st layer of R2 NR of 14P2 in (A). (**A** and **G)** Raw AFM height images. (**B** and **H**) Raw FFT from un-filtered AFM images (A and G). (**C** and **I top panel**) filtered images after 2D FFT-Filtering by masking and reconstructing high intensity points. (**D** and **J**) are FFTs generated by 2D-FFT filtered images in C and I (top panel). (**F** and **K**) are radially integrated plots of filtered-FFT data (D and J) after conversion to real space using $V(r)=1/r_{INT}$, where r_{INT} is the distance from the center in FFT reciprocal space. Solid black lines in A, C and E separate the boundary of the 2nd layer from the first. Dashed lines in E and I highlight boundaries of individual NR.

Analysis showed group 2 (~0.5 nm) lies at the center of the NR and correlates with the distance between backbones of the monomers in β-sheet. Deconvoluted features in group 3 (~1 nm) have an unusual pattern and appear to coincide with the positions of N- and C-terminals in the overlaid model. Both periodicities were at different orientations therefore show they are not duplicates. Group 1 (~2nm) features belong to the reduced width of the NR and may correlate to the ordered YINFSY domain.

A similar protocol was used for 14P2 R1 NR (**Figure 2.17** A-C). R1 has intense peaks at periodicities of 0.78, 1.04, 1.24, 1.61, 1.76, 2.29 and 2.56 nm (Figure 2.17 C) which are too large for a β-sheet structure and absent in the XRD measurements. Therefore, we infer that R1 may not form in solution and assembles only on graphite. The large distances (~0.7) between the diagonally arranged units (assumed as one monomer indicated by white lines in (Figure 2.17 A) within a ribbon suggests a structure with fully extended monomers held together by hydrogen bonds between the side chains (tyrosine) or between the side chain and the backbone. Such structures were previously reported to exist on atomically flat surfaces [125,126].

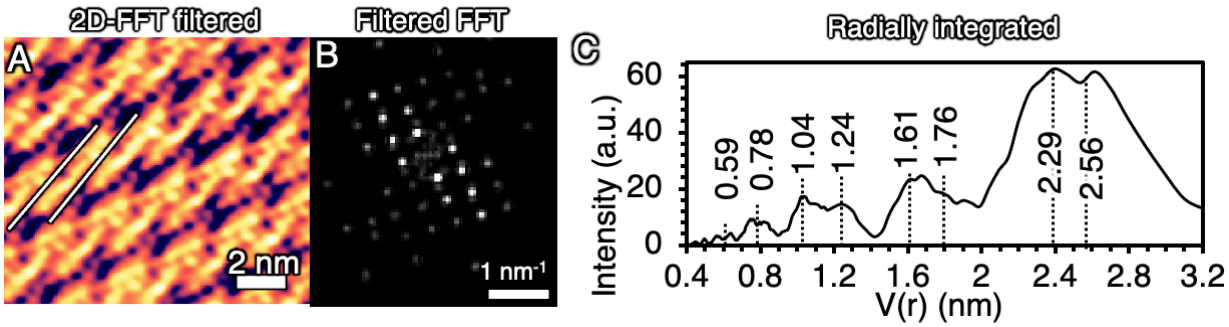

Figure 2.17. Structure of 14P2 R1 NR by high-resolution AFM. (**A**) Filtered images after 2D FFT-Filtering by masking and reconstructing high intensity points. (**B**) FFT generated by filtered image B. (**C**) Radially integrated plots of filtered-FFT data (B) after conversion to real space. Solid white lines in A highlight feature that resemble fully extended peptide monomers.

2.9 STRUCTURE BY MOLECULAR DYNAMICS SIMULATIONS

Deconvolution of the high-resolution structure of R2 type NRs of 14P2 on HOPG (**Figure 2.16)** revealed distinct 0.4-0.6 nm periodicities at the center of the NR (**Figure 2.16 F** and **K**), consistent with the 0.47 nm d-spacing of the β-sheet backbone from obtained bulk solution XRD measurements with or without graphite **(Figure 2.14**) and previous reports on 14P2 and rH174 nanoribbons [65,88,92]. In contrast, the periodicities of the surface features of R1 NR do not match any β sheet models or XRD d-spacings. Since R2 rather than R1 matches the β-sheet NR structure relevant to *in vivo* Amel NR, R1 type was not used further.

To gain insights into the identity and distribution of exposed residues arising from the R2 NR assembly, we performed MD simulations using the CHARMM-based Interface Force Field (IFF) with over 50 conformations for all peptides in solution and on HOPG, including the use of virtual π electrons on graphite and aromatic amino acids which was shown to be critical to reproduce solvent and organic interfacial interactions [125,127,128].

2.9.1 *Equilibrium conformation in solution*

Systematic simulations for 13-15 ns predicted the most favorable β-sheet conformation in solution at pH 1.94 for both the basic 14P2 sequence and the three modified versions (**Figure 2.18**). These results were also compared to the structure and energetics of a random coil conformation. The equilibrated structures of the monomers in β-sheet, which exhibit parallel orientation, show that YINFSY domains for all sequences were, while the N-termini, which were relatively flexible, displayed transient pairing of adjacent N-to-N terminal in a single β-sheet. In contrast, the Cterm domains (DKTKREEVD) in 14P2Cterm and p14P2Cterm were flexible,

tended to twist away from the backbone, and showed pairing of the adjacent C-to-C terminal in a single β-sheet, which may account for the preference of the Cterm to adopt a random coil or flexible conformation in solution. Whereas modification of the single serine to phosphoserine had no distinct impact on the stability of the β-sheet structure. In addition, a small degree of twist was observed for all the β-sheets after simulations.

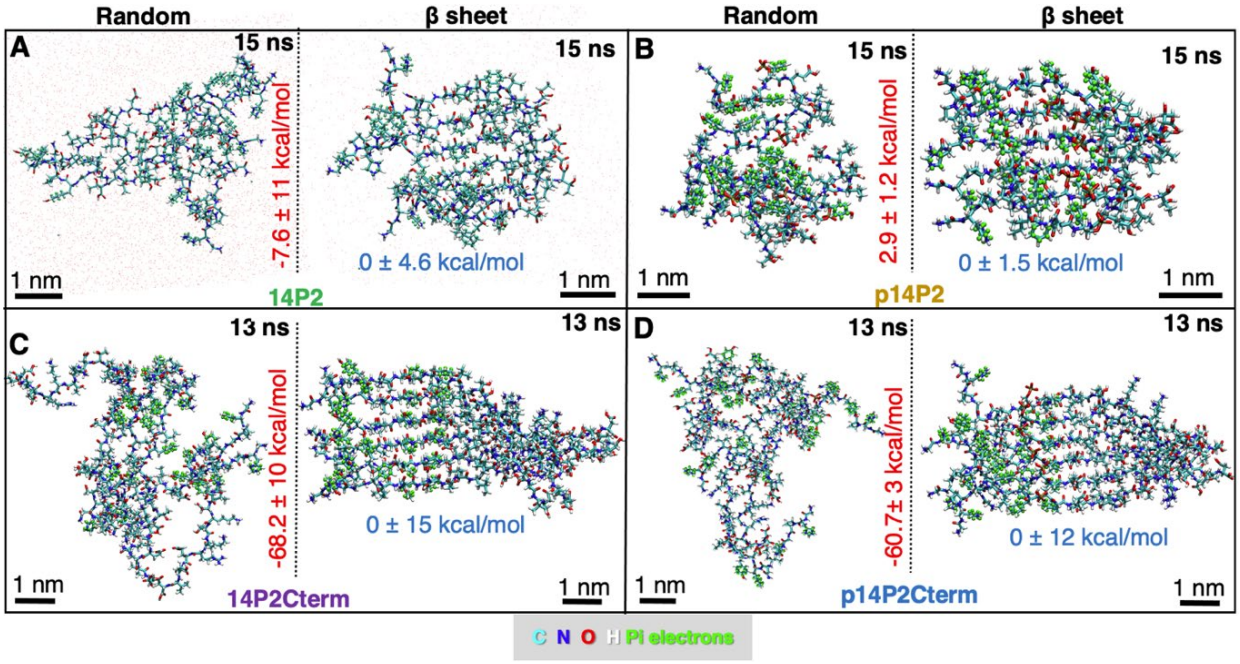

Figure 2.18. Equilibrated structures and relative energies for 6-monomer peptides with random coil and β-sheet conformations in solution (10 mM HCl, pH 1.94) after 13-15 ns simulations [120]**.** The average energy of the β-sheet structure was set to zero as a reference state including the uncertainty. (**A**) 14P2, (**B**) p14P2, (**C**) 14P2Cterm and (**D**) p14P2Cterm. Water molecules are hidden for clarity (except in A).

For direct comparison of the energy between the four sequences, the β-sheets were assumed to be zero energy for reference within the uncertainties of 14P2: 0±4.6 kcal/mol, p14P2: 0±1.5 kcal/mol, 14P2Cterm: 0±15 kcal/mol and p14P2Cterm: 0±12 kcal/mol. Therefore, the energies of random coil conformations relative to the β-sheet structure, were 14P2: -7.6±11 kcal/mol, p14P2: 2.9±1.2 kcal/mol, 14P2Cterm: -68.2±10 kcal/mol and p14P2Cterm: -60.7±3 kcal/mol. The energy differences between random and β-sheet conformation for 14P2 and p14P2 are similar and within

the error bar, which implies β-sheets can form in solution within the experimental conditions. Interestingly, 14P2Cterm and p14P2Cterm show propensity (energetically favorable) to adopt random conformation, however, this is likely related to the attraction of water molecules to the highly charged Cterm domain. Because molecular resolution AFM and XRD results have clearly demonstrated the formation and existence of peptide β-sheets in solution and on HOPG at concentrations from 6.26 μM to 1.6 mM. A previous study also suggested certain amyloid-like ribbon forming sequences can adopt a random-coil conformations in solution prior to nucleation and the existence of barrier associated with conformational switching to form β-sheets in solution. The free energy change for protofibril (single β-sheet) formation with a similar structure (*Sup35*) suggested the energies are unlikely to be strongly negative since the amyloid-like fibrils are stabilized by protein concentration, formation of cross-β-sheets and hydrogen bonded backbones [92]. But once a nucleus forms, high concentrations of protein drive the formation and contribute to a large barrier to dissolution of the protofibrils.

2.9.2 *Adsorption energy of peptides on HOPG*

The calculated E_{ads} for β-strands are -23.9±5 kcal/mol for 14P2 (**Figure 2.19**), -23.9±2 kcal/mol for p14P2, -26.9±8 kcal/mol for 14P2Cterm and -25.9±8 kcal/mol for p14P2Cterm, respectively. The negative E_{ads} implies peptide binding onto HOPG is thermodynamically favorable, but weak enough to allow for reversible binding of β-strands to the surface. This explains why peptides can self-assemble into NR on the HOPG surface. The other contribution towards ΔG could be monomer-monomer binding energies within the β-sheet structure as measured previously by Dynamic Force Spectroscopy for 14P2 [81], but highly accurate structure and energy calculations by MD for a β-sheet on HOPG would need at least 100 monomers [125]. The

$E_{ads}$for β-sheets on HOPG was not carried out since the calculations of 100 monomers for our four peptide systems with 14 to 23 amino acids per peptide would require a monumental amount of computational resources. However, these calculations were performed previously for a 7 amino acid MoS_2 binding peptide (MoSBP1) that forms NRs on MoS_2 and HOPG. 14P2 and MoSBP1 (YSATFTY) have some sequence homology in the YINFSY domain. In MoSBP1 system, the E_{ads} for binding of one monomer on MoS_2 is -96 kcal/mol and -18 kcal/mol for ~100 monomer system. These energies corresponded to strong binding, consistent with *in situ* AFM experiments. Therefore, the results suggest similar trends for 14P2; E_{ads} for 14P2 β-sheets may be smaller in magnitude compared to monomers yet have sufficiently strong binding to HOPG.

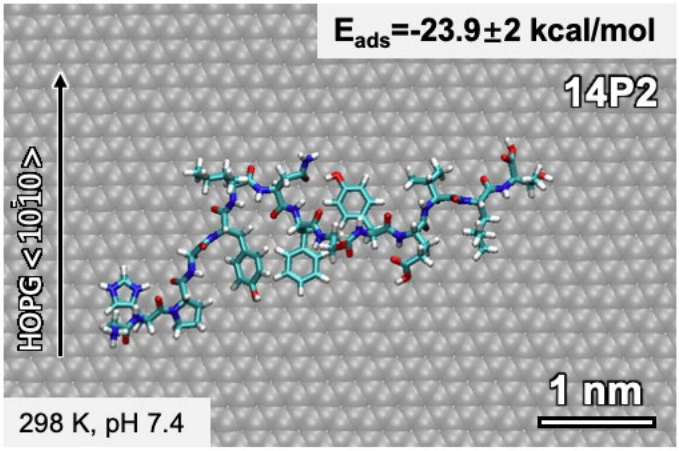

Figure 2.19. Representative snapshot of a fully extended 14P2 (β strand) on HOPG at 8 ns [120]**.** Virtual π electrons are hidden).

2.9.3 *Equilibrium conformation on graphite*

On graphite, the experimentally observed shortest length of 14P2 R2 NR was ~10 nm. Therefore, an equivalent length of a 14P2 β-sheet with 21 monomers was placed on graphite based on the R2 NR structure and orientation shown in **Figure 2.20 A**. Simulations performed for 13.5 ns showed an equilibrium conformation that matches the AFM morphology and ~1 nm height (Figure 2.20 B**)**. In addition, the relative amino acid flexibility near the N termini in the simulations

and the overlay of the simulated structure on the AFM images indicate the 0.9-1.2 nm periodicity and corresponding bright features at the NR edges (Figure 2.20 A bottom panel) can be due to N- to N- terminal pairing between every two monomers within a NR, likely due to electrostatic interactions.

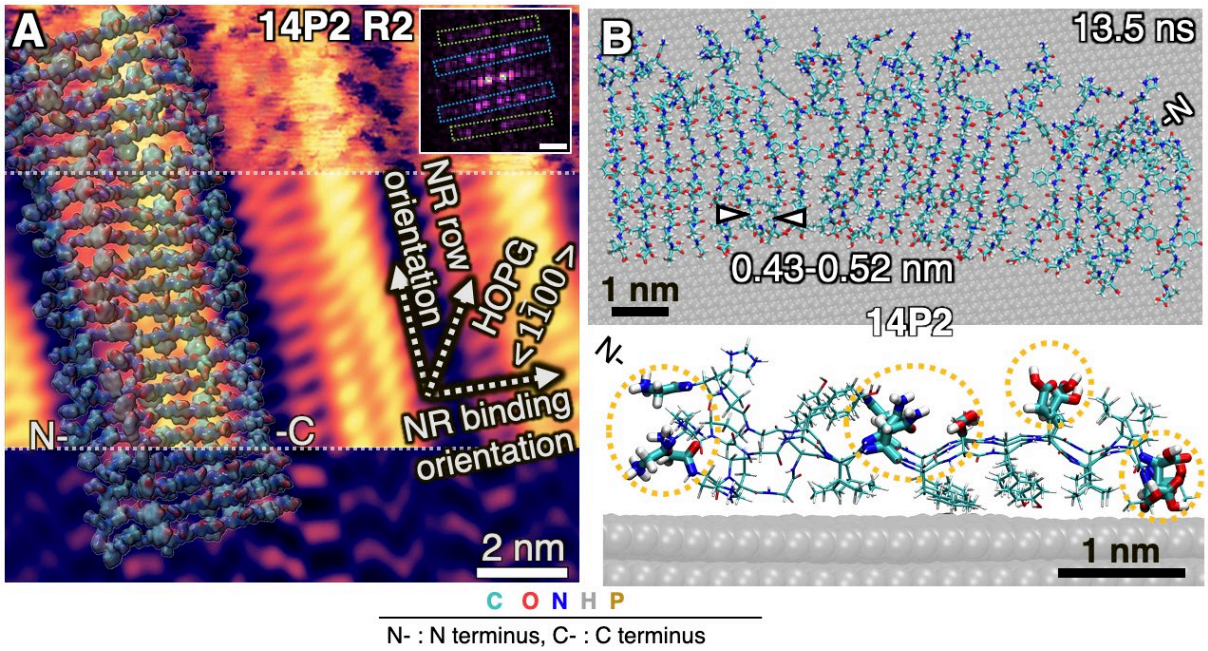

Figure 2.20. Lowest energy β-sheet conformations of peptides on HOPG (0001) at pH 1.94 from all-atom MD simulations [120]**.** (**A**) 21 monomer β-sheet of 14P2 overlayed on high-resolution AFM structure of 14P2 R2 NRs. Inset FFT shows high intensity points (in magenta) used to deconvolute the raw image in top panel of B; middle panel shows the 2D-FFT filtered β-sheet structure with ~0.5 nm periodicities (green boxes in FFT), and without noise and 0.92-1.18 nm features; bottom panel shows only periodic 0.92-1.18 nm features (blue boxes in FFT), with highest intensity at edges of the NR. FFT scale bar is 1 nm^{-1}. (**B**) Top view and side view snapshots of of 21 monomer 14P2 β-sheet on HOPG simulated for 13.5 ns shows structure is stable.

A similar analysis for p14P2, 14P2Cterm and p14P2Cterm NRs was limited to 6 monomers on graphite due to the computationally intensive nature of simulations for the higher number of atoms involved. Despite the limitation, simulations show that modifying 14P2 with phosphoserine or appending the C-terminus generated similar ordered packing in the YINFSY segment of the 14P2 domain on graphite (**Figure 2.21**). However, the Cterm domains (DKTKREEVD) in 14P2Cterm and p14P2Cterm were more disordered than their 14P2 domains and pair up to twist

away from the backbone, indicating flexibility at the C-terminal end of the ribbons, consistent with the simulations in solution. To further resolve the structure of the Cterm sequences on graphite, we overlayed the simulated β-sheet structure of 14P2Cterm in solution onto the high-resolution AFM image (**Figure 2.22)**. The overlay shows an excellent match in the width of the β-sheet and the gap between two adjacent NRs, both of which are larger than those for 14P2 NRs (Figure 2.20).

In addition to showing that the most stable predicted structures match that of the single β-sheet structure deduced from AFM and XRD measurements, the MD simulations also predict that, for all peptides investigated, the phenyl residues are bound to the graphite surface by π-π interactions (**Figure 2.20** and **Figure 2.21** side view), whereas nearly all hydrophilic side chains, including phosphoserine, glutamic acid and asparagine, protrude into the solution with a 0.43 – 0.52 nm periodicity that transverses the long axis of the NR (highlighted by dashed yellow circles in **Figure 2.20** and **Figure 2.21).** While detailed *in situ* physicochemical studies on R2 NRs on HOPG at the molecular-level to confirm these predictions are currently not possible, from the simulations and their comparison to the AFM and XRD results, we again conclude that the R2 NRs formed on HOPG are single β-sheets, which are precursors to the cross-β-sheets both formed in bulk solution and observed in vivo and present a similar (hydrophilic) NR surface to the solution. Thus, they provide a suitable NR-solution interface for AFM-based nucleation studies.

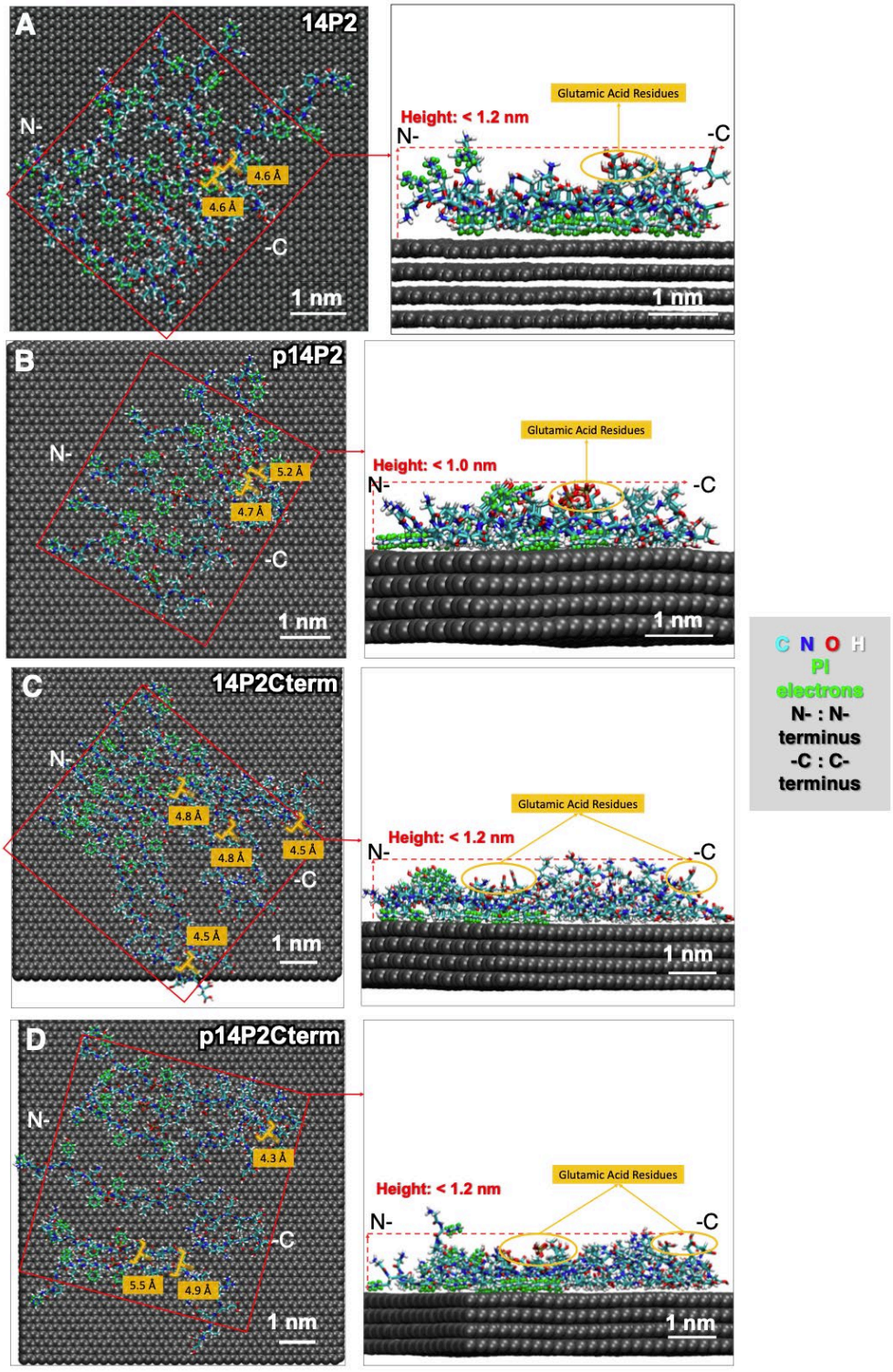

Figure 2.21. Simulations of 6-monomer β sheet conformation for 20 ns simulations in 10 mM HCl (pH 1.94) on HOPG [120]. Snapshots shown for (**A**) 14P2, (**B**) p14P2, (**C**) 14P2Cterm and (**D**) p14P2Cterm. Left: top view; right: side view. Water molecules are hidden for clarity. Distances between part of the backbone of the β strands and height of the peptides are marked in A-D.

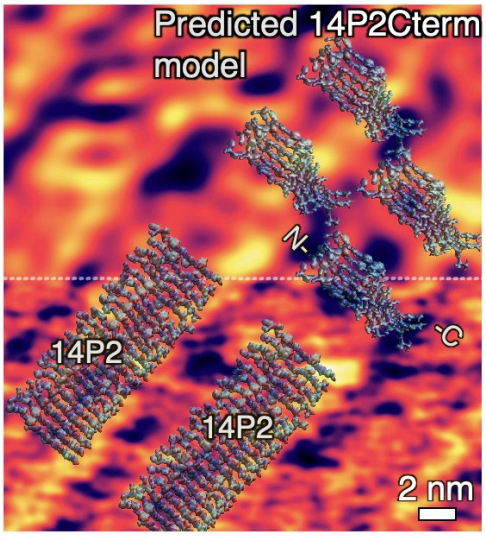

Figure 2.22. Predicted β sheet structure of 14P2Cterm R2 NRs on HOPG [120]**.** Image shows a comparison of 14P2 model on HOPG and 14P2Cterm equilibrated in solution in overlayed on AFM image of 14P2Cterm; bottom: original image, top: 2D-FFT filtered.

Chapter 3. CALCIUM PHOSPHATE NUCLEATION, GROWTH AND PHASE TRANSFORMATION

To quantify the impact of Amel NR-solution interfaces on calcium phosphate nucleation rates, we used *in situ* AFM to investigate nucleation and growth using substrates with R2 NRs, identical to those in **Figure 2.6 A - E**, at pH 7.4 and 25 ºC for a range of supersaturations σ (**Table 3.2**) over timescales for which nucleation was absent both in solution and on bare HOPG (**Figure 3.1**). The value of σ was calculated using an equilibrium solubility determined in two ways: 1) from the value of the equilibrium constant K_{sp} reported previously at a different ionic strength [129] and 2) using the ionic activity product at which the post-nucleation growth rate extrapolated to zero, discussed below.

Table 3.2. Sample Ion activities and supersaturations with respect to ACP for the three sets of solutions used for mineralization [120].

Activity (mM) at pH 7.4		**σ_{ACP} (K_{sp}=1.155 x 10^{-15} M^5 from growth rates)**	**σ_{ACP} (K_{sp}=8.03 x 10^{-17} M^5 from Habraken et al.)**
Ca^{2+}	**HPO_4^{2-}**		
0.2826	3.526	0.221	0.75
0.2618	3.227	0.138	0.67
0.239	2.916	0.04	0.57

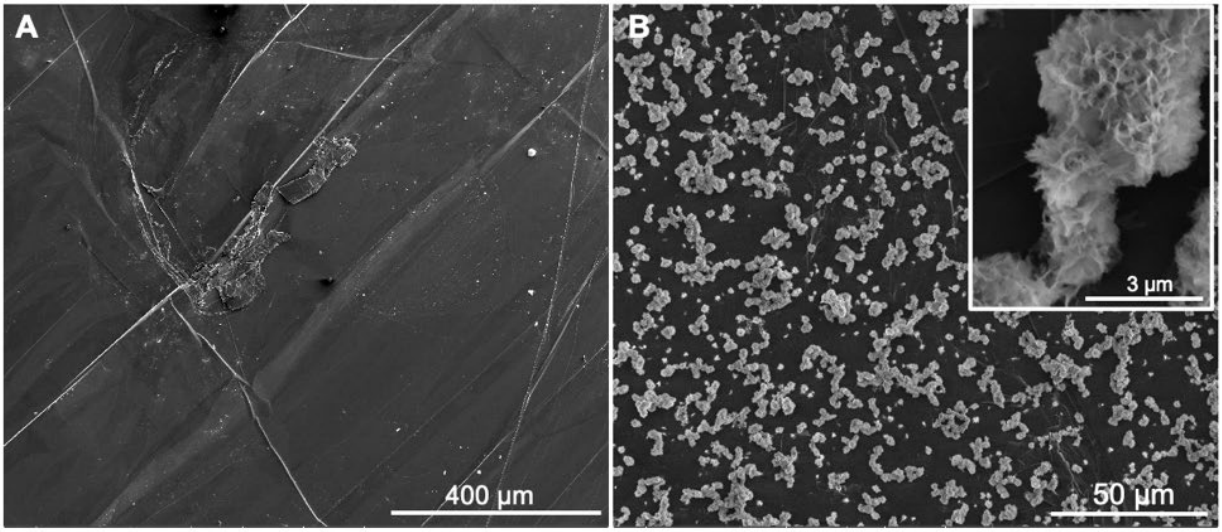

Figure 3.1. SEM images of HOPG surfaces incubated in supersaturated calcium phosphate solutions σ_{ACP} = 0.221 for 1hr [120]**.** (**A**) without adsorbed peptide and (**B**) with 14P2 NRs. Control of bare HOPG shows no significant mineral, whereas 14P2 coated HOPG has plate-like mineral at 1 hr,

3.1.1 *Calculation of supersaturations with respect to ACP*

Equilibrium solubility values of ACP (K_{sp}) from most studies in literature and VISUAL MINTEQ calculations indicate that solutions used here are undersaturated with respect to all types of ACP. For such cases, ACP could nucleate, but not continue to grow, unless the previously reported solubilities do not reflect our solution conditions. Therefore, the relationship between growth velocity (V) and supersaturation in **Eq.** 3.1 is used to extract the apparent solubilities, where IAP is ionic activity product for previously reported $(Ca_2(HPO_4)_3)^{2-}$ pre-nucleation cluster given by $(a(Ca^{2+})^2 \bullet a(HPO_4^{2-})^3)$, ω is volume of growth unit (ACP: 5 x 10^{-29} m^3), n= 5, a([x]) is ionic activity (in M), and β is the kinetic coefficient, was exploited to plot growth velocity vs $IAP^{1/5}$ Figure 3.2 G

$$V = \omega \beta (IAP^{1/5} - K_{sp}^{1/5}) \quad \text{Eq. 3.1}$$

Ionic activity product of all three solutions was determined from free ion concentrations given by Visual MINTEQ for each solution conditions (**Table 3.3**). Growth rates for each sequence and saturation were obtained from average slopes of linear fits to heights vs elapsed time for multiple particles (**Table 3.4)**. Then the relationship between growth rate vs $IAP^{1/5}$ was linearly fit with an error-weight and extrapolated to zero growth rate to determine IAP at which no growth occurs (V= 0, x-axis intercept), i.e., K_{sp}. From these measurements and *SI Appendix,* Equation 3, we found that solubility of ACP is 1.155 x 10^{-15} M^5 which lies between Visual MINTEQ (8.42 x 10^{-12} M^5) and our previous bulk solution measurements (8.03 x 10^{-17} M^5) [129]. Using K_{sp} from growth rates extrapolated to zero or from previous measurements, supersaturations were calculated using **Eq** 3.2**.**

$$\boldsymbol{\sigma_{ACP}} = \frac{\mathbf{\ln IAP - \ln K_{sp}}}{\boldsymbol{n}} \qquad \text{Eq 3.2}$$

Table 3.3. Species relevant to ACP and activities calculated by Visual MINTEQ for solutions supersaturated with respect to hydroxyapatite (σ_{AP}) at pH 7.4, with stoichiometry (log (activity of Ca^{2+}/activity of PO_4^{3-})) = 3.87. The phosphate reagent concentration (column 3) is the total concentration of phosphate species that includes HPO_4^{2-}, PO_4^{3-}, $H_2PO_4^-$ and all other phosphate containing species in solution.

Bulk σ_{AP}	Species	Reagent concentration (mM)	Free ion concentration (M)	Activity (M)	Exponents for ACP	Ionic Strength (M)
3.37	Ca^{2+}	1	4.94 x 10^{-4}	2.826 x 10^{-4}	2	0.0203
	HPO_4^{2-}	-	6.164 x 10^{-3}	3.526 x 10^{-3}	3	
	PO_4^{3-}	9.5	1.312 x 10^{-7}	3.735 x 10^{-8}	-	
3.28	Ca^{2+}	0.875	4.462 x 10^{-4}	2.618 x 10^{-4}	2	0.0182
	HPO_4^{2-}	-	5.499 x 10^{-3}	3.227x 10^{-3}	3	
	PO_4^{3-}	8.475	1.134 x 10^{-7}	3.417x 10^{-8}	-	
3.19	Ca^{2+}	0.75	3.963 x 10^{-4}	2.39 x 10^{-4}	2	0.016
	HPO_4^{2-}	-	4.8336 x 10^{-3}	2.916 x 10^{-3}	3	
	PO_4^{3-}	7.45	9.63 x 10^{-8}	3.089 x 10^{-8}	-	

Table 3.4. Vertical growth rates (V) of particles for various sequences at different supersaturation and intercepts and slopes obtained from error-weighted linear fits using Eq. 3.1. Error is std. dev., for sample size refer to Statistics (main text) [120]

		14P2Cterm	14P2	p14P2Cterm	p14P2	rH174
σ_{ACP}	$IAP^{1/5}$ (M)	V (nm/sec)	V (nm/sec)	V (nm/sec)	V (nm/sec)	V (nm/sec)
0.04	0.00107	1.89 ± 0.01	1.18 ± 0.04	1.18 ± 0.02	0.5 ± 0.02	1.05 ± 0.07
0.138	0.00118	5.24 ± 0.02	4.17 ± 0.08	3.86 ± 0.09	1.74 ± 0.05	4.3 ± 0.05
0.221	0.00128	10.16 ± 0.08	6.91 ± 1.96	6.93 ± 1.03	3.01 ± 0.06	6.78 ± 1.52
		14P2Cterm	14P2	p14P2Cterm	p14P2	rH174
Intercept ($K_{sp}^{1/5}$)		1.0202×10^{-3}	1.0265×10^{-3}	1.0264×10^{-3}	1.0284×10^{-3}	1.0284×10^{-3}
K_{sp} (M^5)		1.1052×10^{-15}	1.1395×10^{-15}	1.1392×10^{-15}	1.1501×10^{-15}	1.1503×10^{-15}
β		3.8×10^{-5}	2.72×10^{-5}	2.68×10^{-5}	1.18×10^{-5}	2.85×10^{-5}

Thus, the supersaturations calculated using K_{sp} of ACP reported previously [129] gave σ_{ACP} = 0.57, 0.67 and 0.75. Whereas supersaturations calculated using growth rates are σ_{ACP} = 0.04; σ_{ACP} = 0.138; and σ_{ACP} = 0.221, which were primarily for discussions as they are specific to our AFM experiments.

3.1.2 *Nucleation growth and phase transformation of ACP*

Time-lapse images revealed that, for all values of $\boldsymbol{\sigma}$ explored here, all five sequences nucleated similarly shaped spherical cap-shaped calcium phosphate particles (**Figure 3.2 A-E**), though at different rates (Figure 3.2 F). Additional post-nucleation characterization by *in situ* AFM, supported by Transmission Electron Microscopy (TEM), revealed that ACP was the first phase to form in all cases (**Figure 3.4**, **Figure 3.5**, **Figure 3.6**, and **Figure 3.7**). These ACP particles grew in size before transforming to fiber- or plate-shaped crystals with sequence-specific growth rates (Figure 3.2 G) and lifetimes of 14P2Cterm: ~39 min < p14P2Cterm: 56.63 min <

14P2: 56.71 min < rH174: 125.71 min < p14P2: ~218.9 min (Figure 3.7). The analysis of the radially integrated electron diffraction data of the initially formed particles confirmed the absence of 0.25-0.33 nm d-spacing corresponding to octacalcium phosphate (OCP) or AP found in late-stage mineral (Figure 3.6). The results obtained here are consistent with the identity and dynamics of nuclei formed under identical experimental conditions — with or without proteins — previously characterized using multiple techniques [40,129,130]. The composition of ACP was reported previously to be $Ca_2(HPO_4)_3)^{2-}$ [129].

Analysis of the early stage of mineralization on all sequences showed nucleation rates and nuclei number density were highest on the phosphorylated peptides, p14P2 and p14P2Cterm (**Figure 3.2** and **Figure 3.3)**, which had particles concentrated along the length of the NRs. In contrast, ACP growth rates were higher on non-phosphorylated peptides than on their phosphorylated versions (Figure 3.2 G). Furthermore, appending the C-terminus to 14P2 and p14P2 sequences resulted in an increase of 1.3 to 2 times in nucleation rates and a factor of 1.5 to 2.3 in (vertical) growth rates. Comparison to previous results using conformationally dissimilar Amel nanospheres (8-9 nm in size) and nanospheres co-assembled with enamelin (Enam), a highly-charged protein also associated with enamel formation (Figure 3.2 H, Amel sph: Enam, 50:0 and 50:1)[40], shows that all NR sequences drive higher nucleation rates than do nanospheres, and the phosphorylated NRs outperform the mixed Amel nanosphere-Enam system, even at lower supersaturations and for the optimal Amel:Enam ratio. Interestingly, phosphorylated NRs induced ACP nucleation rates 1.9 to 2.8 times larger than observed even on collagen (Figure 3.2 H, Col. σ_{ACP} = 0.128**;** bovine Type I 97%) [129]*,* which is also rich in proline and phosphoserines and has an extended acicular morphology. These findings show that both sequence and conformation strongly

impact template activity and that phosphorylated Amel NRs are the most potent ACP nucleators investigated to date.

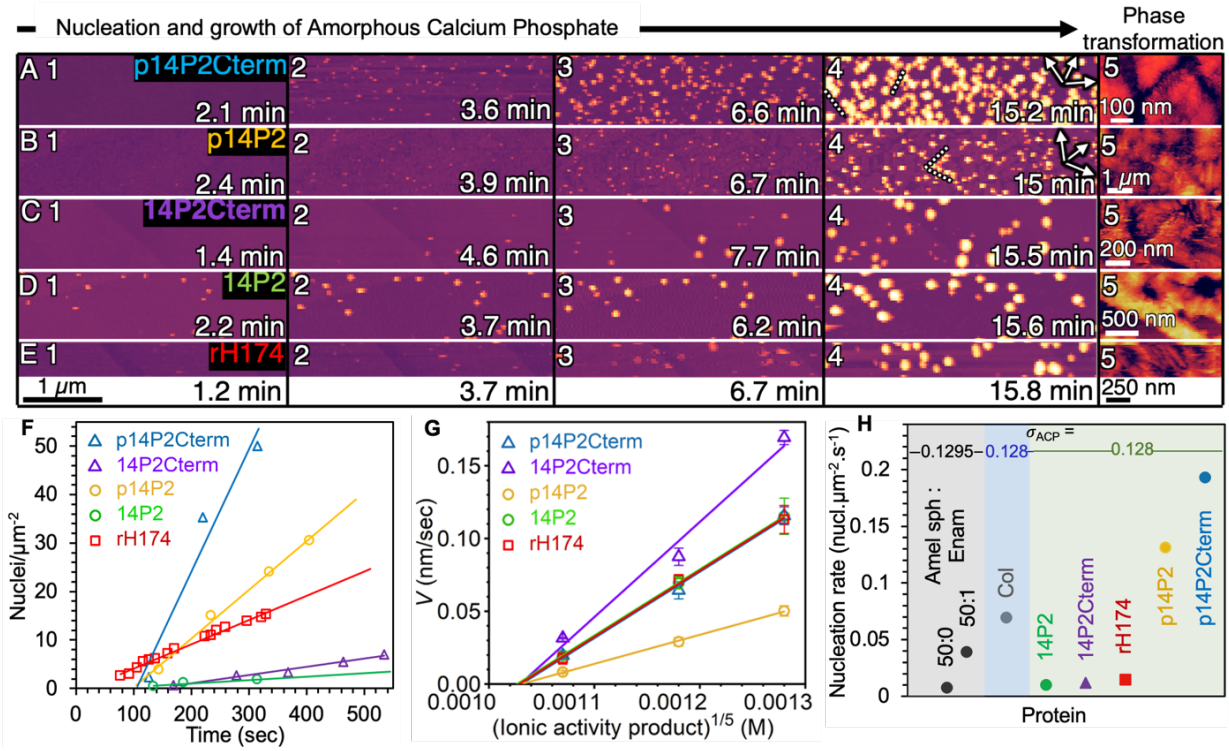

Figure 3.2. Kinetics of ACP nucleation and growth on peptide and protein nanoribbons [120]**.** (**A-E**) Time lapse of AFM images using constant supersaturation, σ_{ACP} = 0.221 (σ_{AP} = 3.37), at 25˚ C and pH 7.4, with t = 0 min defined as the time when solution is introduced into the flow cell. Dotted lines indicate ACP aligned with direction of NRs (arrows). (**F**) Plot of nuclei number density over time measured for all sequences at σ_{ACP} = 0.22. Error bar is smaller than data points. (**G**) Average growth rate of particle height (*V*) at σ_{ACP} = 0.04, 0.138 and 0.221. **(H)** Comparison of nucleation rates for different proteins: amelogenin nanospheres co-assembled without (50:0) and with enamelin (50:1) at σ_{ACP} = 0.1295, collagen at σ_{ACP} = 0.128 and amelogenin nanoribbons at σ_{ACP} = 0.128.

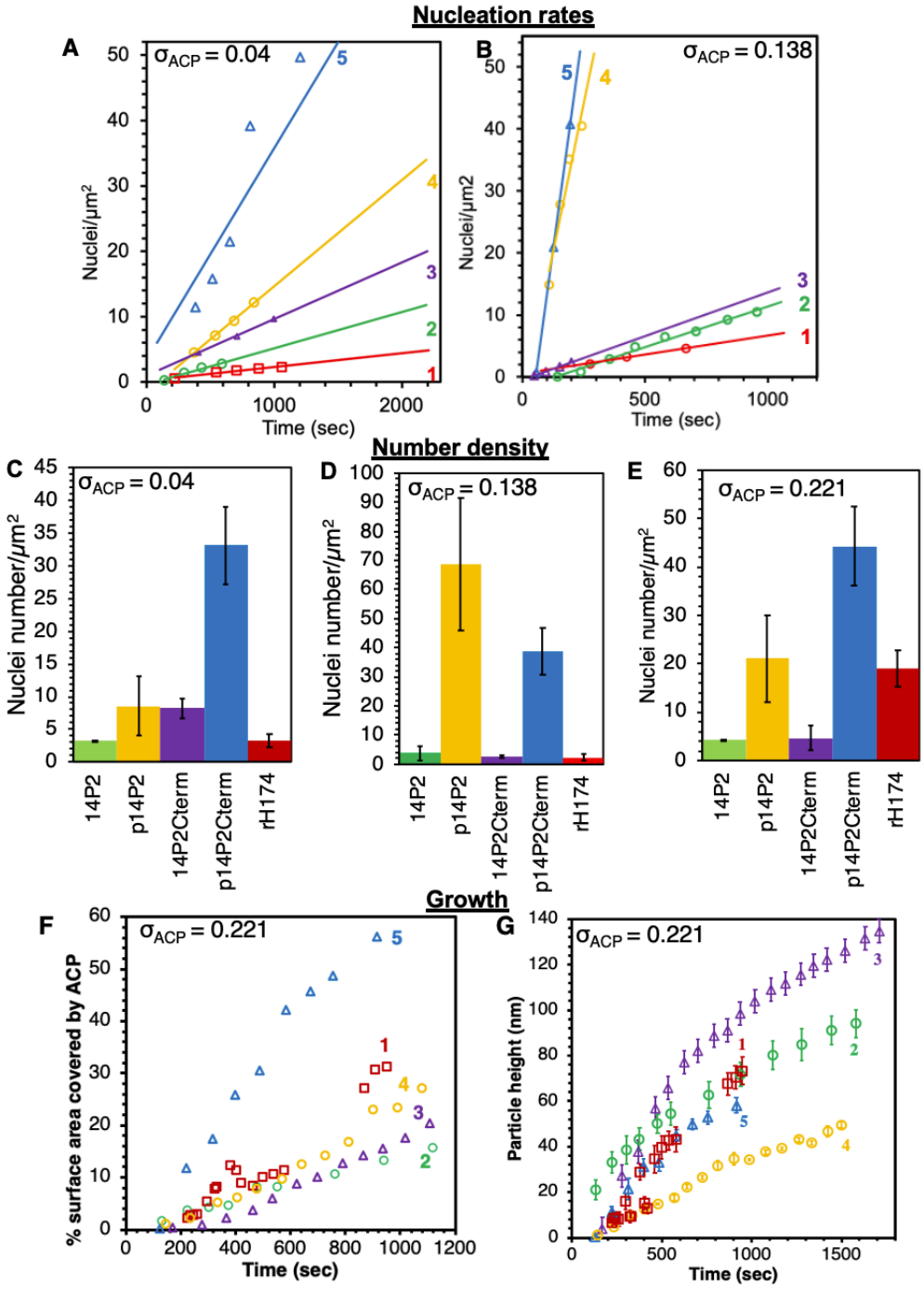

Figure 3.3. Analysis of nucleation and growth on various sequences at different supersaturations using height images from in situ AFM where (1) is rH174, (2) is 14P2, (3) is 14P2Cterm, (4) is p14P2, and (5) is p14P2Cterm [120]. Representative nucleation rates (J_o) at (**A**) σ_{ACP} = 0.04 and (**B**) σ_{ACP} = 0.138. Average nuclei density per μm^2 for various sequences at (**C**) σ_{ACP} = 0.04, at time = 15-18 minutes (**D**) σ_{ACP} = 0.138 at time = 5-6 minutes and (**E**) σ_{ACP} = 0.221 at time = 5-6 minutes. (**F**) Percentage surface area covered by ACP and (**G**) average height of ACP particles increase over time for all sequences measured for σ_{ACP} = 0.221, n = 4 particles.

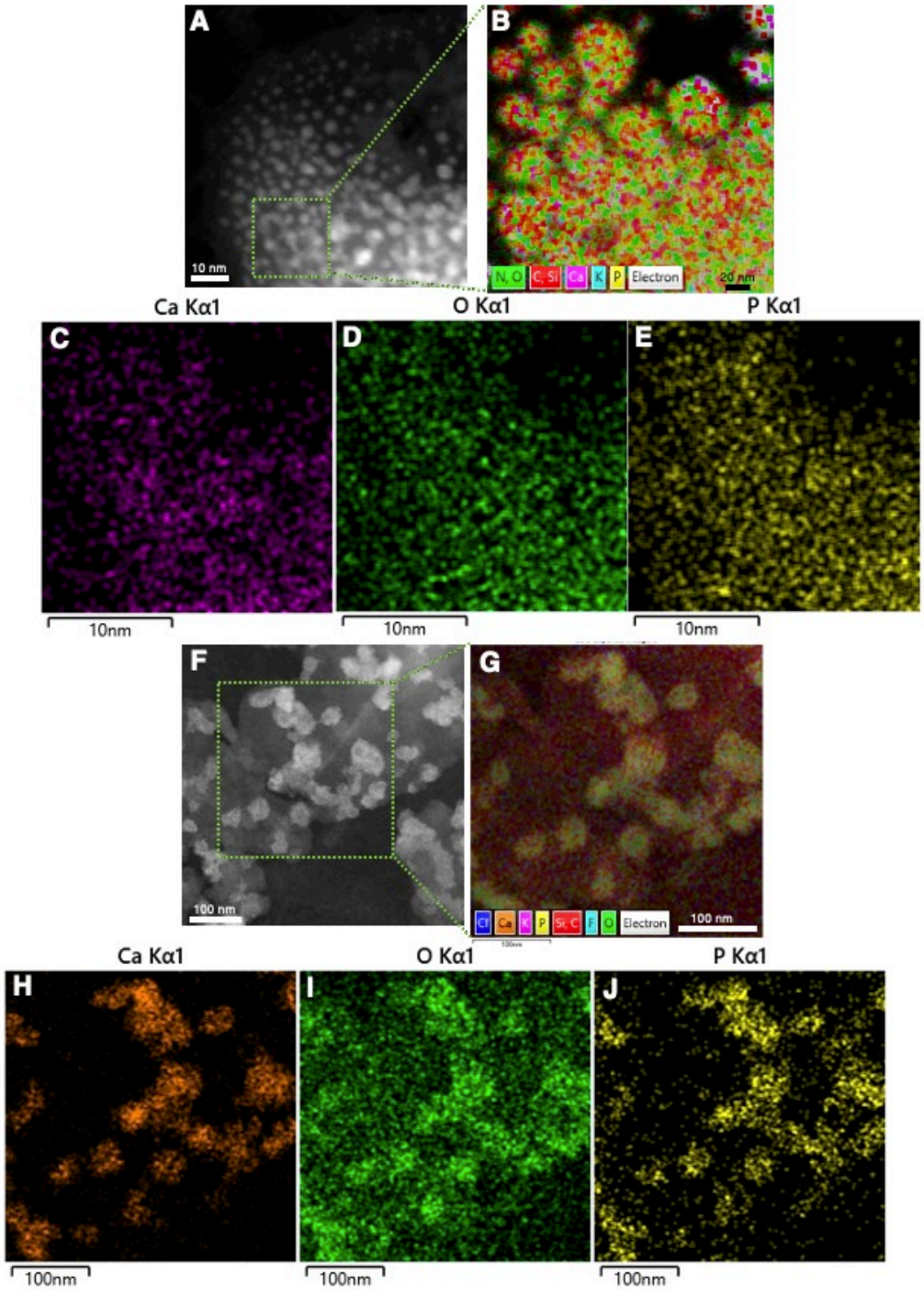

Figure 3.4. STEM and Elemental Dispersive Spectroscopy (EDS) map of minerals [120]. Graphene grids functionalized (**A** to **E**) with rH174 and (**F** to **J**) with p14P2Cterm then incubated in supersaturated calcium phosphate solution $\sigma_{ACP} = 0.221$ at pH 7.4 for 20 min. (A) and (f) STEM image, (B) and (G) Composite image of elements N, O, C, Si, Ca, K, P and electrons, (C) and (H) Map of Calcium atoms, (D) and (I) Map of Oxygen atoms, and (E) and (J) Map of Phosphate atoms. The particles had a high concentration of Ca, P and O compared to the background. The background had high C, O and N signal corresponding to the graphene or organic constituents.

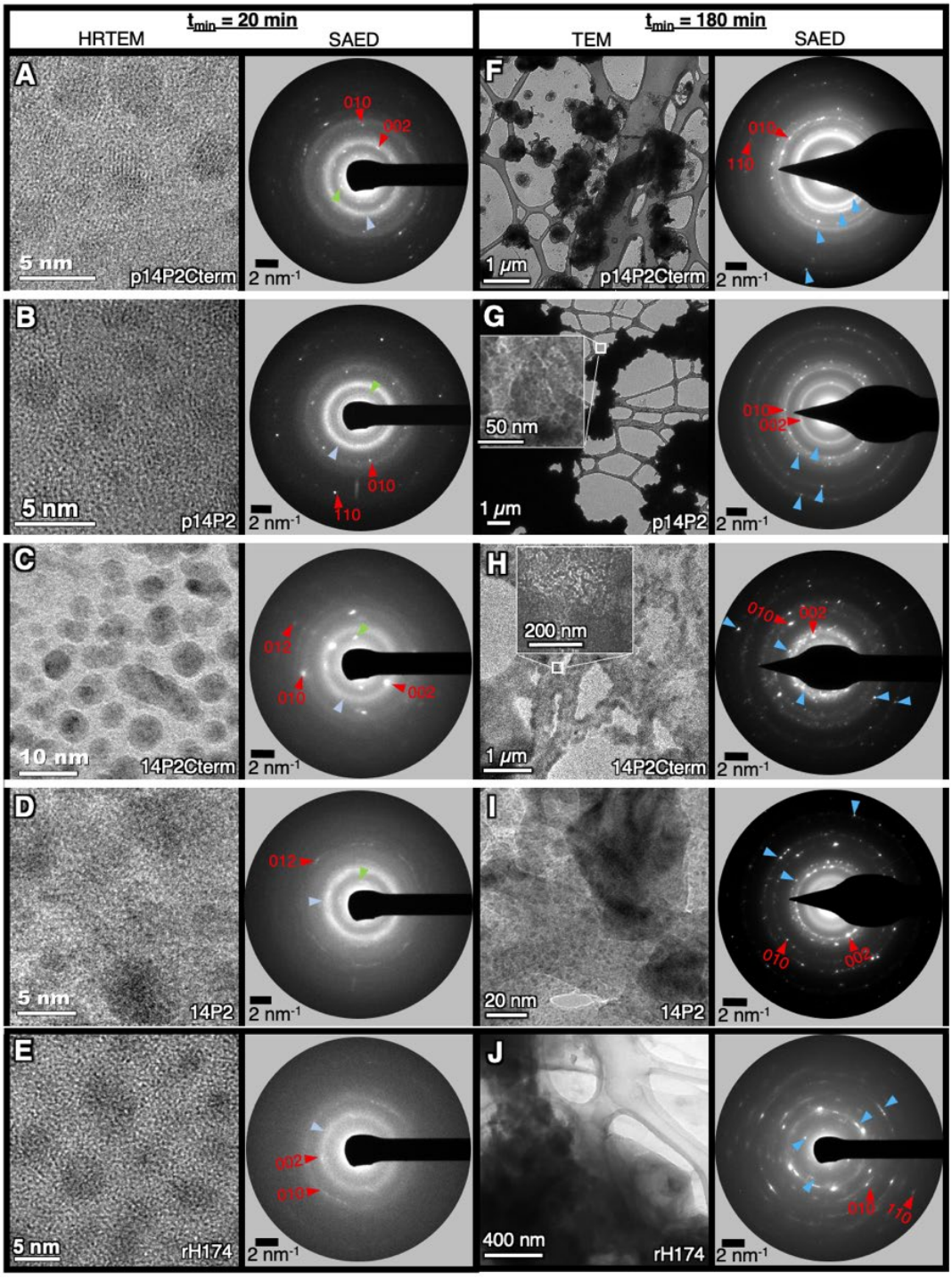

Figure 3.5. TEM characterization of quenched graphene grids functionalized with NRs of (**A**) and (**F**) p14P2Cterm, (**B**) and (**G**) p14P2, (**C**) and (**H**) 14P2Cterm, (**D**) and (**I**) 14P2, and (**E**) and (**J**) rH174 after incubation in $\sigma_{ACP} = 0.221$ calcium phosphate solution for (**A**) to (**E**) 20 min and (**F**) to (**J**) 180 min [120]. At 20 min, particles are amorphous, shown by SAED with diffraction spots from graphite (red), peptides (green) and diffuse ring of ACP (light blue) and further analyzed in Figure 3.6. (F) to (J) shows higher crystallinity at 180 min and SAED confirms speckled ring diffraction with spots from AP or OCP (blue).

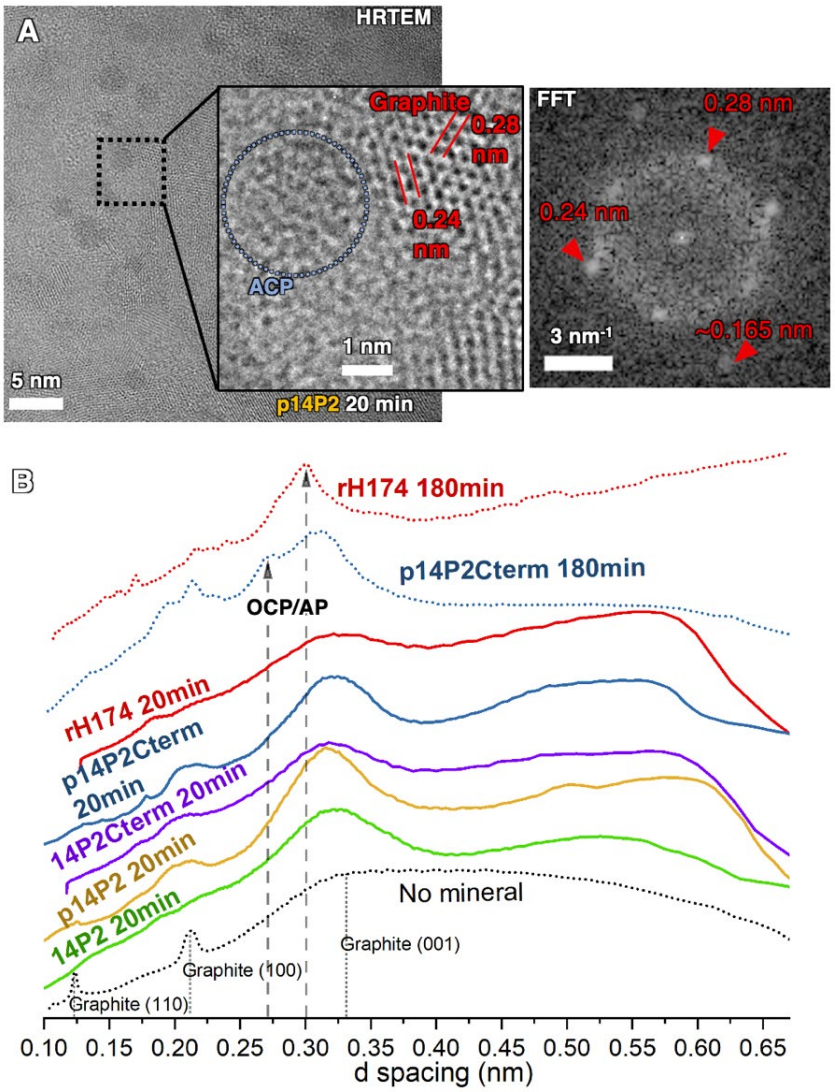

Figure 3.6. Amorphous nature of particles mineralized for 20 min on 3-5 layer graphene substrates coated with NRs assessed through FFT of HRTEM and radially integrated SAED data [120]. HRTEM for p14P2 in **(A)** shows several round particles (dark features). Further magnification of area in black dotted square shows the region marked as ACP (blue circle) lacks long range order and FFT of the image shows spacing correlated to graphene. 0.28 and 0.24 nm spacings match the C-C distance in armchair <10$\bar{1}$0> and zig-zag <1$\bar{1}$00> directions (Cong et al 2013) while the weak ~0.165 nm matches the (004) plane of 3-5 layer graphene or graphite. **(B)** Radially integrated profiles of SAED on protein-coated grids after 20 min and 180 min mineralization. At 20 min, all sequences show absence of the sharp crystalline peaks of OCP and AP at 0.26-0.33 nm d-spacing, (indicated by dashed vertical lines) previously reported using Cryo-TEM and Low Dose-SAED (Habraken et al. 2013) and observed here at 180 min for rH174 and p14P2Cterm mineralization. Other sequences show similar diffraction patterns at 180 min. SAED from a 3-5 layer graphene grid coated with p14P2Cterm NRs but without mineral was used as control.

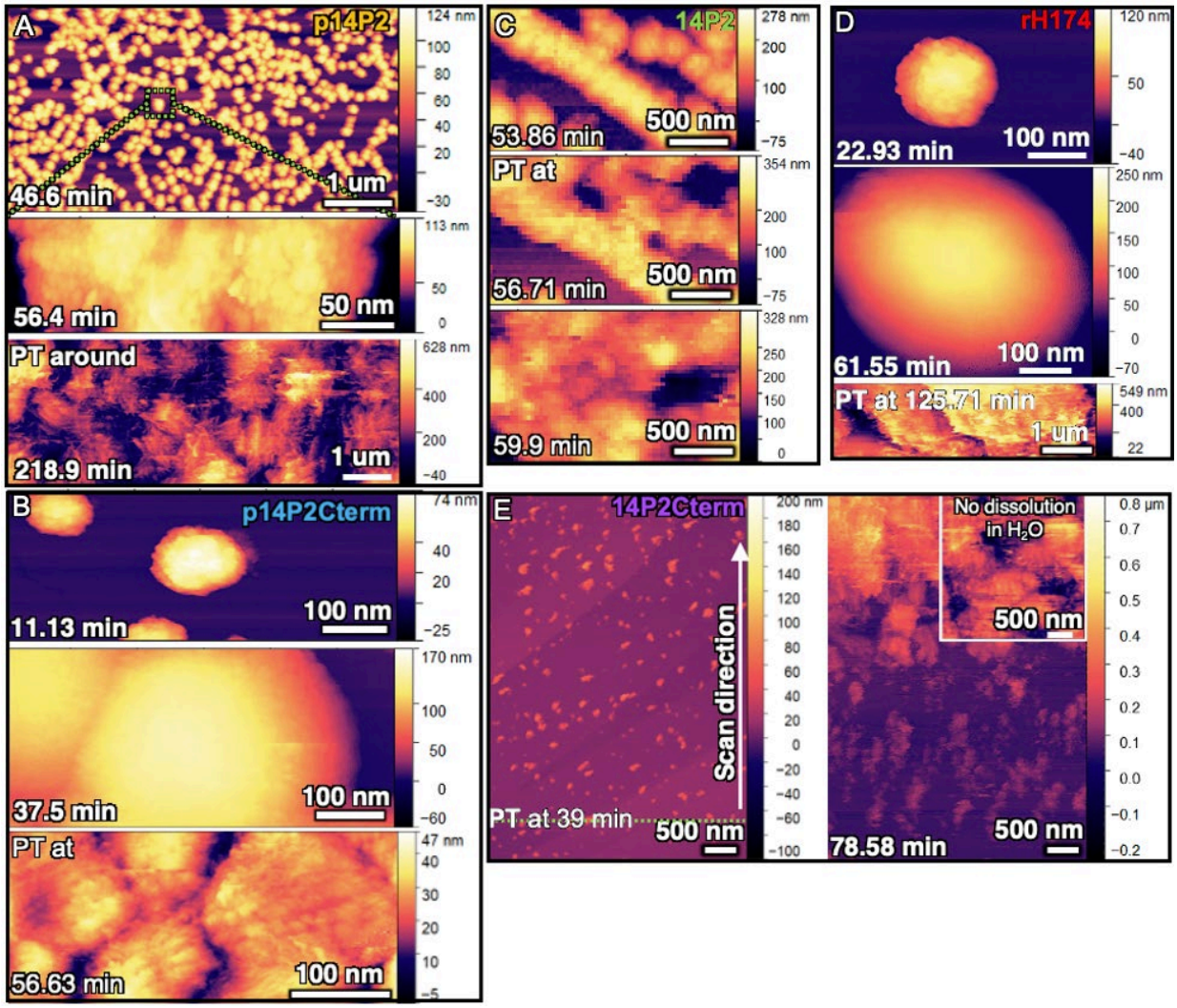

Figure 3.7. ACP growth and phase transformation using height images from in situ AFM under constant composition (σ_{ACP} = 0.221), pH 7.4 and 25˚C on NRs of **(A)** p14P2, **(B)** p14P2Cterm, **(C)** 14P2, **(D)** rH174 and **(E)** 14P2Cterm [120]**.** Surface of the particles are initially smooth but eventually becomes rougher, which indicates that the amorphous particles phase transformed into a crystalline phase with a nanoplatelet or fibrous morphology. Phase transformation was fastest for 14P2Cterm (~39 min) and slowest for p14P2 (>150 min), which correlates with the growth rates, implying that without phosphorylation, ions prefer the ACP-solution interface over NR-solution or NR-mineral interfaces.

3.1.3 *Energetics of nanoribbon interface*

To determine the mechanism and underlying energetic factors through which Amel NRs drive ACP nucleation, the data on nucleation rates vs σ were analyzed using classical nucleation

theory (CNT), which has been used previously to analyze heterogeneous nucleation on organic templates [28,29,40,129,131] and has been shown to effectively describe ACP nucleation kinetics [129]. CNT predicts that the heterogeneous nucleation rate (J_o) varies exponentially with the effective interfacial energy (α_{ACP}) and σ_{ACP} according to:

$$\ln(J_o) = \ln(A) - \frac{B}{\sigma_{ACP}^2} \quad \text{Eq. 3.3}$$

$$B = \frac{8\pi\omega^2\alpha_{ACP}^3}{3(kT)^3} \quad \text{Eq. 3.4}$$

where A is the kinetic pre-factor, which depends on the density of possible nucleation sites [132], attachment rates, and barriers to ion desolvation [25], ω is volume of the ACP growth unit, k is Boltzmann's constant and T is absolute temperature.

This equation was originally derived from Eq 3.5 and the derivation is briefly described here. The change in free energy required to create a hemispherical nuclei of radius R on a substrate is given by Eq. 3.6. Subscripts *ML, MS and LS* refer to mineral-liquid, mineral-substrate and liquid-substrate interfaces, respectively. The critical radius R_c of nucleus is given by Eq. 3.7 where α_{eff} is given by Eq. 3.8**.** Substituting Eq. 3.7 in Eq. 3.6, then Eq. 3.8, to simplify ΔG in Eq. 3.6, gives Eq. 3.9. Substituting Eq. 3.9 back into Eq 3.5, gives Eq. 3.10, and taking natural logarithm on both sides gives Eq. 3.11**.**

The volume of growth unit (ω**,** defined as the volume of complex/number of ions) of ACP ($Ca_2(HPO_4)_3)^{2-}$) used in this study is 5 x 10^{-29} m^3, which is an intermediate value between the volume of a Posner cluster with composition $Ca_9(PO_4)_6$ (2.993 x 10^{-29} m^3) and disk-like structure with volume of 9.5 x 10^{-29} m^3 that is the building block for OCP and AP [129]. α_{ACP}, the effective

interfacial energy of the nucleating phase, can be determined from plots of nucleation rates at different supersaturation using the classical nucleation theory (*SI Appendix,* Equation 11). The nucleation rates are obtained from nucleation events per μm^2 versus time (in seconds) then converted to m^{-2} s^{-1} (**Table 3.5**) for plotting **ln (J_o)** versus σ_{ACP}^{-2}. The values of α_{eff} obtained using K_{sp} from growth rates and previous report of K_{sp} from solution measurements are shown in **Table 3.6** and **Table 3.7**, respectively. The theoretical value of α_{ACP} in bulk solution was reported as 150 mJ m^{-2}, and nominal value of 100 mJ m^{-2} for comparison of experimental data. The value of the equilibrium solubility values of ACP (K_{sp}) affects the supersaturation values, and thus the interfacial energies values. However, the relative ratios of the energies for each sequence when compared to the other will remain unchanged for identical experimental conditions. Therefore, the ratios of the energies with respect to the basic 14P2 sequence without any functional group modifications are used for comparison. The interfacial energy and kinetic pre-factor A ratios with respect to 14P2 in the analysis reflect $\alpha_{\text{ACP of Sequence}}/\alpha_{\text{ACP of 14P2}}$ and $A_{\text{Sequence}}/A_{14P2}$, respectively.

$$J_o = A.e^{\left(\frac{-\Delta G_c}{kT}\right)} \quad \text{Eq 3.5}$$

$$\Delta G = -\frac{2\pi R^3 kT\sigma}{3\omega} + 2\pi R^2\alpha_{ML} + \pi R^2(\alpha_{MS} - \alpha_{LS}) \quad \text{Eq. 3.6}$$

$$R_c = \frac{2\omega\alpha_{eff}}{kT\sigma} \quad \text{Eq. 3.7}$$

$$\alpha_{eff} = \alpha_{ML} + \frac{1}{2}(\alpha_{MS} - \alpha_{LS}) \quad \text{Eq. 3.8}$$

$$\Delta G_c = \frac{8\pi\omega^2\alpha_{eff}^3}{3(kT\sigma)^2} \quad \text{Eq. 3.9}$$

$$J_o = Ae^{\left(\frac{-8\pi\omega^2\alpha_{eff}^3}{3(kT\sigma)^2}\right)} \quad \text{Eq. 3.10}$$

$$\ln(J_o) = \ln(A) - \frac{B}{\sigma^2} \quad \text{where } B = \frac{8\pi\omega^2\alpha_{eff}^3}{3(kT)^3} \quad \text{Eq. 3.11}$$

Table 3.5. Nucleation rates (J_o, in nuclei $m^{-2}s^{-1}$) at different supersaturations used in calculations for interfacial energies of ACP nucleation on various sequences. Error is Std. dev. [120]

		14P2	p14P2	14P2Cterm	p14P2Cterm	rH174
σ_{ACP}	σ_{ACP}^{-2}	Ln J_0	Ln J_0	Ln J_0	Ln J_0	Ln J_0
0.04	597.137	22.419 ± 0.021	23.408 ± 0.153	22.764 ± 0.164	24.165 ± 0.055	21.448 ± 0.011
0.138	52.502	23.075 ± 0.208	26.064 ± 0.162	23.089 ± 0.475	26.129 ± 0.323	22.447 ± 0.133
0.221	20.318	23.084 ± 0.313	25.362 ± 0.037	23.374 ± 0.179	26.021 ± 0.327	24.511 ± 0.180

Fitting the data for all values of σ_{ACP} reveals two key energetic features of Amel NRs (**Figure 3.8**). First, the values of α_{ACP} for all NR sequences are remarkably small when compared to either nucleation on collagen (40 mJ m^{-2}) or in bulk solution (100-150 mJ m^{-2}) [129], ranging from either 1.4 to 2.4 mJ m^{-2} or 12 to 20 mJ m^{-2}, depending on the method used to determine K_{sp}. Hence, we infer that nucleation is highly favorable on Amel NRs due to the low interfacial energy. The data also show that both addition of the C-terminus to 14P2 and phosphorylation of the analogs have minor effects on α_{ACP}, with the induced change ranging from a factor of 0.9 to 1.5 (Figure 3.8 B ad E). The second key feature, which stands in stark contrast to the uniformity of α_{ACP}, is a 15 to 19-fold increase in the kinetic pre-factor A with phosphorylation (Figure 3.8 C and F). Comparison of the relative values of A with the relative increase in net charge of the peptide reveals a positive linear scaling, likely reflecting higher rates of Ca ion binding or lifetimes of bound Ca ions at the NR-solution interface.

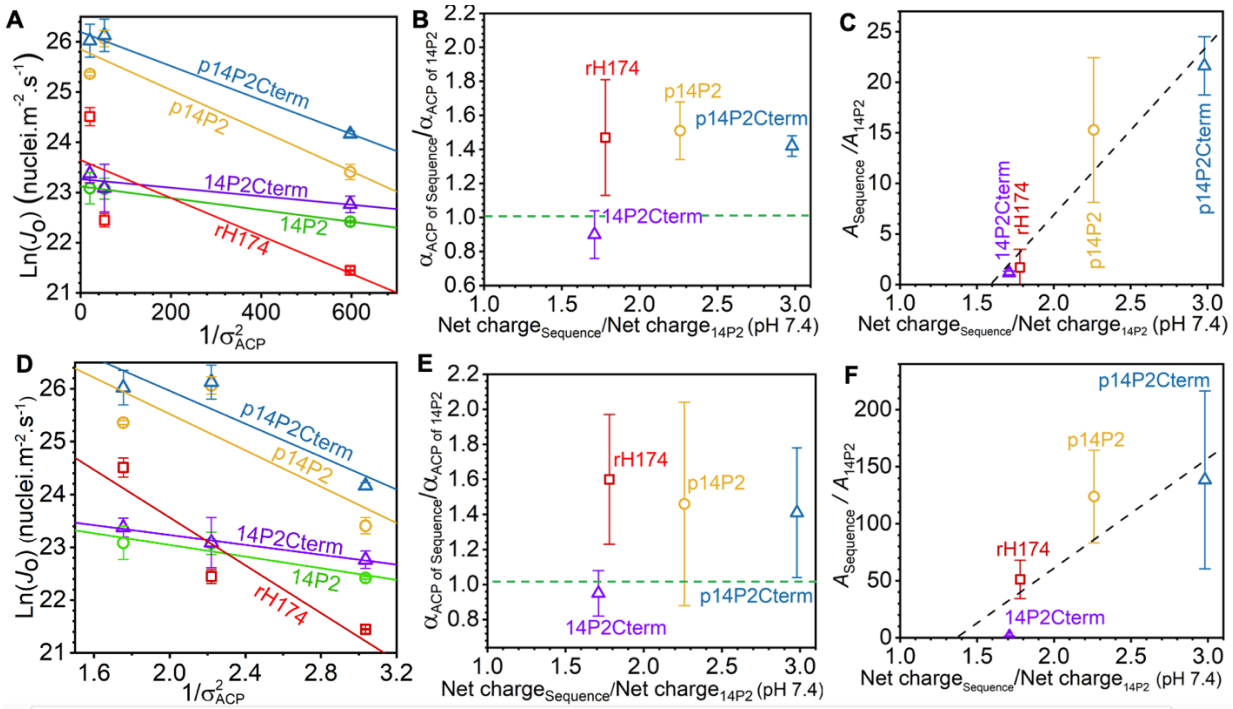

Figure 3.8. Energetics of ACP nucleation on peptide and protein nanoribbons [120]**.** (**A** to **C**) calculated using σ_{ACP} based on K_{sp} = 1.155 x 10^{-15} M^5 from extrapolation of growth rates to zero and (**D** to **F**) using K_{sp} = 8.03 x 10^{-17} M^5 from a previous study [129]. (**A** and **D**) Linear fits to ln(J_o) (nuclei m^{-2} s^{-1}) measured at different ACP supersaturations (1/ σ^2_{ACP}). (**B** and **E**) Ratio of interfacial energy (α_{ACP}) and (**C** and **F**) ratio of kinetic pre-factor (A) of sequences with respect to 14P2 for each sequence vs. ratio of net charge of sequences with respect to 14P2 (-1.4) at pH 7.4. Dashed line in (B and E) shows location of α_{ACP} of 14P2 and in (C and F) shows linear-fit. Error bar in A and D represents standard deviation, and standard error (range) in B, C, E and F.

Table 3.6. Net charge, ln(A) and α_{eff} obtained from linear fits to nucleation rate data using Equation S11 and supersaturations calculated from extrapolated growth rates [120]. Ratios of kinetic pre-factor A ($A_{Sequence}/A_{14P2}$), effective interfacial energy with respect to ACP α_{ACP} ($\alpha_{ACP\ of\ Sequence}/\alpha_{ACP\ of\ 14P2}$), and charge for each sequence with respect to 14P2 from analysis. Error is Std. error (range)

Sequence	Net charge per monomer at pH 7.4	Net charge relative to 14P2	Ln(A)	Ratios: $A_{sequence}$ / A_{14P2}	α_{eff} (mJ.m^{-2})	Ratios: $\alpha_{ACP\ of\ Sequence}/\alpha_{ACP\ of\ 14P2}$
14P2	-1.4	-	23.12 ± 0.01	-	1.58 ± 0.02	-
14P2Cterm	-2.4	1.71	23.27 ± 0.14	1.16 ± 0.18	1.41 ± 0.23	0.90 ± 0.14
rH174	-2.492	1.78	23.64 ± 1.04	1.69 ± 1.80	2.32 ± 0.73	1.47 ± 0.34
p14P2	-3.16	2.26	25.85 ± 0.45	15.28 ± 7.15	2.38 ± 0.26	1.51 ± 0.17
p14P2Cterm	-4.166	2.98	26.19 ± 0.12	21.62 ± 2.88	2.24 ± 0.07	1.42 ± 0.06

Table 3.7. Net charge, ln(A) and α_{eff} obtained from linear fits to nucleation rate data using Equation S11 and supersaturations calculated from a previous study [129]. Ratios of kinetic pre-factor A ($A_{Sequence}/A_{14P2}$), effective interfacial energy with respect to ACP α_{ACP} ($\alpha_{ACP\ of\ Sequence}/\alpha_{ACP\ of\ 14P2}$), and charge for each sequence with respect to 14P2 from analysis. Error is Std. error (range)

Sequence	Net charge per monomer at pH 7.4	Net charge relative to 14P2	Ln(A)	Ratios: $A_{sequence}$ / A_{14P2}	α_{eff} (mJ.m^{-2})	Ratios: $\alpha_{ACP\ of\ Sequence}/\alpha_{ACP\ of\ 14P2}$
14P2	-1.4	-	24.15 ± 0.49	-	12.23 ± 0.20	-
14P2Cterm	-2.4	1.71	28.97 ± 2.98	1.02 ± 0.43	11.57 ± 1.24	0.95 ± 0.13
rH174	-2.492	1.78	28.08 ± 2.00	51.19 ± 16.79	19.57 ± 0.83	1.60 ± 0.37
p14P2	-3.16	2.26	24.17 ± 0.13	123.86 ± 40.70	17.87 ± 0.06	1.46 ± 0.58
p14P2Cterm	-4.166	2.98	29.08 ± 1.65	138.49 ± 77.97	17.29 ± 0.69	1.41 ± 0.37

3.1.4 *Structure-function relationship*

From the perspective of chemical kinetics, the presence of phosphate groups on surfaces should lead to strong binding of multi-ion Ca-complexes and a larger kinetic pre-factor [29]. However, this does not explain why phosphorylated 14P2 NRs have low interfacial energies. Therefore, we investigated structural contributions from the template by comparing the geometric arrangement of the NR's charged side chains with the dimer structure of the $Ca(HPO_4)_3^{4-}$ multi-ion complexes shown previously to be the incipient species leading to formation of ACP through binding of an additional Ca^{2+} ion, as well as to formation of OCP and HAP [129] through further ion binding reactions.

The Ca-Ca distance in the $(Ca_2(HPO_4)_3)^{2-}$ dimer is around 1 nm and the overall size of the dimer is 1.2 ± 0.2 nm. Superposition of Ca^{2+} ions in this dimer onto the predicted p14P2 R2 NR conformation shows an excellent match with the spacing of the periodic hydrophilic residues that span the long axis of the NR (**Figure 3.9**).

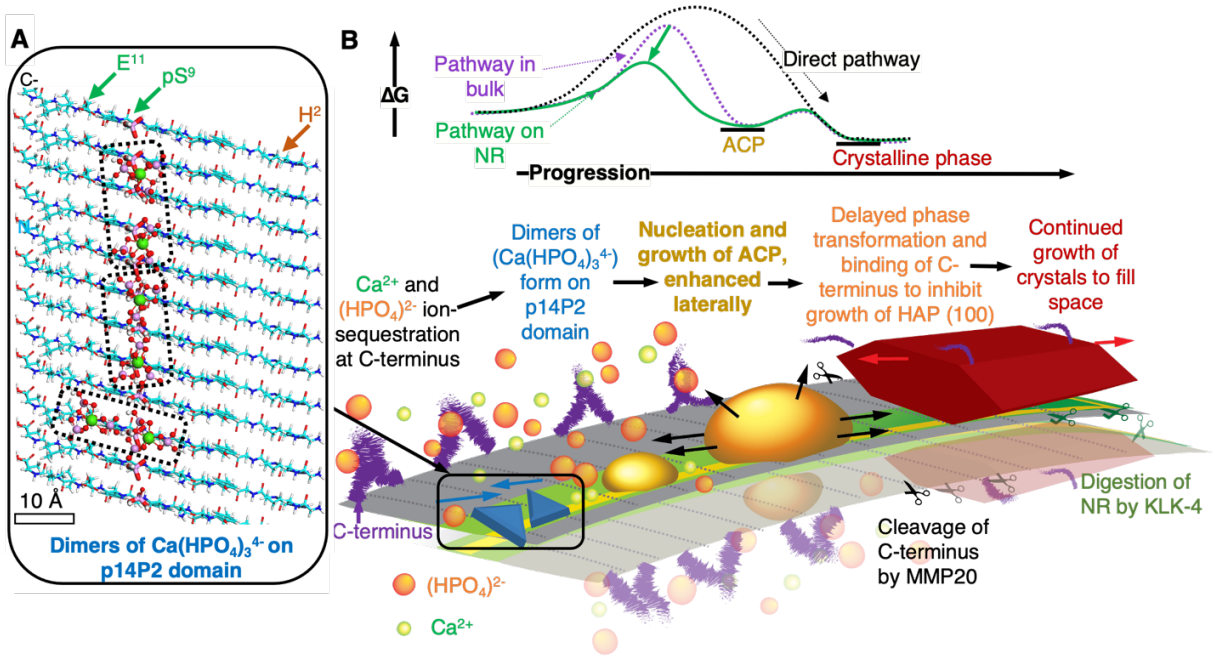

Figure 3.9. Proposed mechanism for full-length amelogenin nanoribbon guided mineralization [120]**. (A)** Cartoon of pre-nucleation clusters $(Ca_2(HPO_4)_3)^{4-}$ superimposed on β-sheet conformation of p14P2 nanoribbon shows potential sites for Ca^{2+} ion docking to allow formation of $(Ca_2(HPO_4)_3)^{2-}$dimers with 1 nm Ca-Ca distance; negative: glutamic acid (E^{11}) and phosphoserine (pS^9), positive: histidine (H^2). **(B)** Proposed role of phosphorylated, cross-β-sheet full-length amelogenin NR based on energetics and kinetics; NR lowers the barrier (ΔG) for nucleation of ACP by stabilizing dimers of $(Ca(HPO_4)_3^{4-})$ on 14P2 domain and following a multi-step crystallization pathway. Phosphorylated 14P2 domain induces ACP to nucleate and spread laterally. ACP eventually transforms to a crystalline phase (OCP or AP), along with binding of C-terminus cleaved by Matrix metalloproteinase-20 (MMP20)). The template structure is retained, the crystal continues to grow along the c-axis, and NR is finally enzymatically digested by Kallikrein-4 (KLK-4) [133]. In presence of ion-rich polymer induced liquid precursors (PILP), Amel NRs may promote binding of PILP to further enhance the local supersaturation and ACP nucleation rates along the NR long-axis.

The dimer could form either over 3-4 protein monomers at the phosphoserine (pS^9) sites or over a single protein monomer between pS^9 and glutamic acid (E^{11}). Thus, binding of Ca^{2+} ions to the periodically repeating phosphoserine residues may provide a means to stabilize dimers of calcium triphosphate and promote formation of ACP by enhancing kinetics without a drastic impact on interfacial energy (α_{ACP}). Interestingly, the protonated **a** (010) and **b** (110) planes of OCP and AP have d-spacings of 0.92 nm (or a/2=b/2= 0.47 nm), which coincides with the

periodicity of hydrophilic residues in Amel NR (Fig. 2A). Therefore, when ACP transforms, the NR may continue to act as a template for OCP or AP due to the structural matching, consistent with both recent studies showing that negatively charged residues likely remain bound to AP phases [134] and the Amel NR model proposed in Carneiro et al. (2016) wherein every alternate phosphoserine is available for interaction with the mineral.

The experiments performed here differ from a number of calcium phosphate mineralization studies, which utilized a polymer induced liquid precursor (PILP) phase produced by addition of acidic macromolecules, such as polyaspartic acid [35,36,135], including the study that demonstrated synthetic NRs can template growth of AP filaments [86]. Our results do not rule out the involvement of PILP during ACP nucleation *in vivo*. However, the stereochemical relationship between Amel NR and calcium phosphate ion complexes, the low interfacial energies, and the enhanced ion binding kinetics are expected to promote ACP nucleation, regardless of whether the ions are delivered from an ion-rich PILP droplet or a less concentrated calcium phosphate solution like that used in our study. As concluded in these previous studies, PILP likely provides a means for liquid-phase infiltration of ions into the protein scaffold (**Figure 3.10**), but nucleation of a solid ACP phase is still promoted by charged residues on the scaffold or complexation of PILP molecules with the scaffold [36]. The low energy interface presented by Amel NR likely promotes binding of the PILP liquid phase, which then creates a high local supersaturation due to the high concentration of calcium and phosphate ions around the acidic macromolecules [136]. Because higher supersaturation leads to higher nucleation rate (Eq. 3.3 and Figure 3.8 A and D**),** nucleation rates can be dramatically higher with PILP. Thus, wetting by PILP may lead to rapid formation of ACP

along the length of the NR following the energetics presented here, while transformation of the ACP, guided by the Ca-binding sites, may then result in a single crystal AP filament.

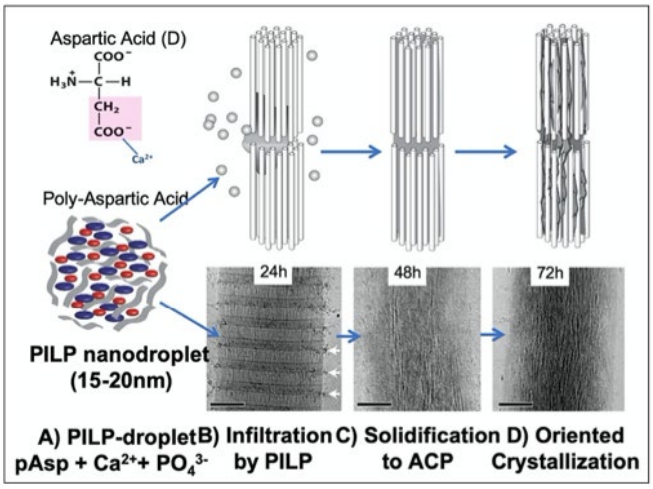

Figure 3.10. Schematic of the polymer-induced liquid precursor (PILP) process based on TEM evidence with collagen fibrils[32,36,101]. Reprinted from Ref.[101]

3.1.5 *Conclusion*

The above experimental findings show that the amyloid structure of Amel NRs, especially the evolutionarily conserved 14P2 self-assembly domain [81,137], drastically lowers the thermodynamic barrier for ACP nucleation. The atomistic-scale simulations highlight that Amel NR presents a periodic template of hydrophilic residues for mineral formation — without involvement of non-Amel proteins — that correlates with our experimental results (Figure 3.9 B). The presence of periodic phosphoserines in NRs dramatically enhances the kinetic pre-factor, likely through enhanced Ca^{2+} ion binding at charged residues, whereas addition of the Amel C-terminus has little impact on these two factors, suggesting that amyloid-like Amel NR can retain its structure and mineralizing function even after cleavage of the C-terminal by MMP20. Whether the C-terminus then independently acts to inhibit HAP (010) growth as previously proposed [44,138], or complexes with mineralizing ions to form PILP-like droplets used in previous NR mineralization experiments to produce aligned AP filaments [86], or both, remains to be explored.

Chapter 4. BIOMIMETIC TEMPLATING OF CALCIUM PHOSPHATE VIA PATTERNED PROTEIN NANORIBBONS

4.1 INTRODUCTION

Directed self-assembly of organic scaffold and nucleation of inorganic particles on pre-defined patterns are important prerequisites for scalable, bottom-up fabrication of advanced hybrid materials with high fidelity [139–143]. Several reports highlighted the thermodynamic, kinetic, stereochemical, and spatial constraints connecting the organic-inorganic interfaces [27–29,144–147]. However, patterning was largely performed with self-assembled monolayers (SAMs) of different organic small molecules [136,144,145,148,149], and yet to be effectively applied for supramolecular assemblies with secondary, tertiary, or quaternary structures[150], which generate sequence-specific local interfaces and environments [120].

4.2 APPROACH AND DESIGN

To address the knowledge gap in structural and physicochemical parameters governing patterned protein-templated mineralization, pAmel NRs—p14P2 (GHPGYINF p(S) YEVLT) and p14P2Cterm (GHPGYINF p(S) YEVLT DKTKREEVD) — were used as the supramolecular template [81,120]. Both sequences are potent amorphous calcium phosphate (ACP) nucleators which present high nucleation rates and low surface energy to ACP nucleation, though p14P2Cterm has higher net charge, ACP nucleation pre-factor and ACP growth rates, and a disordered DKTKREEVD domain appended at C terminus [120].

For directed-self-assembly of pAmel NRs on pre-defined high-resolution patterns, we employ a versatile substrate—silicon supported thin films of block copolymer (BCP) lamellae with alternating hydrophilic and hydrophobic stripes—which were shown to pattern assembly of Fibrinogen[150], SbpA S-layer, and collagen fibers[151]. BCP thin films offer excellent chemical contrast with minimal topographical contrast of stripes, and whose width can be easily tuned and allows exploration of lateral domain sizes and confinement. For our study, we use polystyrene-*block*- poly(methylmethacrylate) (PS-*b*-PMMA), with 50.3 ± 4.1 nm wide PS stripes and 170.9 ± 5.2 nm periodicity, labelled as 50 nm PS (**Figure 4.1**). The hydrophobic and aromatic PS is expected to interact with the aromatic amino acid rich interface of pAmel NRs, while the hydrophilic PMMA is stable at pH 1.94 and charge neutral at pH 7.4 for mineralization. PMMA stripes were fabricated wider than PS to minimize coalescence of mineral particles growing on PS stripes, and simple intrepretation via atomic force microscopy (AFM). This BCP-pAmel NR system is expected to generate heterogeneous hydrophilic interfaces, and as a stringent test of patterning, we show pAmel NRs retain their functionality and biases nucleation of ACP on PS stripes, which, without further functionalization, remain inert during mineralization. In principle, BCP assembly can be tuned to fabricate 3D scaffolds or 3D printed, thus enable scalable, rapid engineering of synthetic bone, tooth, or other hybrid materials by reducing protein load and accelerating fabrication times [152–155].

4.3 Directed self-assembly of pAmel NRs on PS-b-PMMA lamellae

In situ AFM shows a clear change in morphology, height, and phase contrast on assembly of pAmel NRs after 30 min, notably on the PS stripes (Figure 4.1 A). For example, with p14P2 in Figure 4.1 A, PS regions are taller by 1.4 ± 0.3 nm), consistent with measurements on graphite [120],

and NR length ranged from 10 to 150 nm (inset) forming one or two rows on PS (inset). In contrast, PMMA stripes are taller by ~0.6 nm and have ~ 3 nm tall particles interspersed, which are close to the expected thicknesses of a disordered layer of peptide monomers and cross β-sheet aggregate (bi-layers β-sheets), respectively.

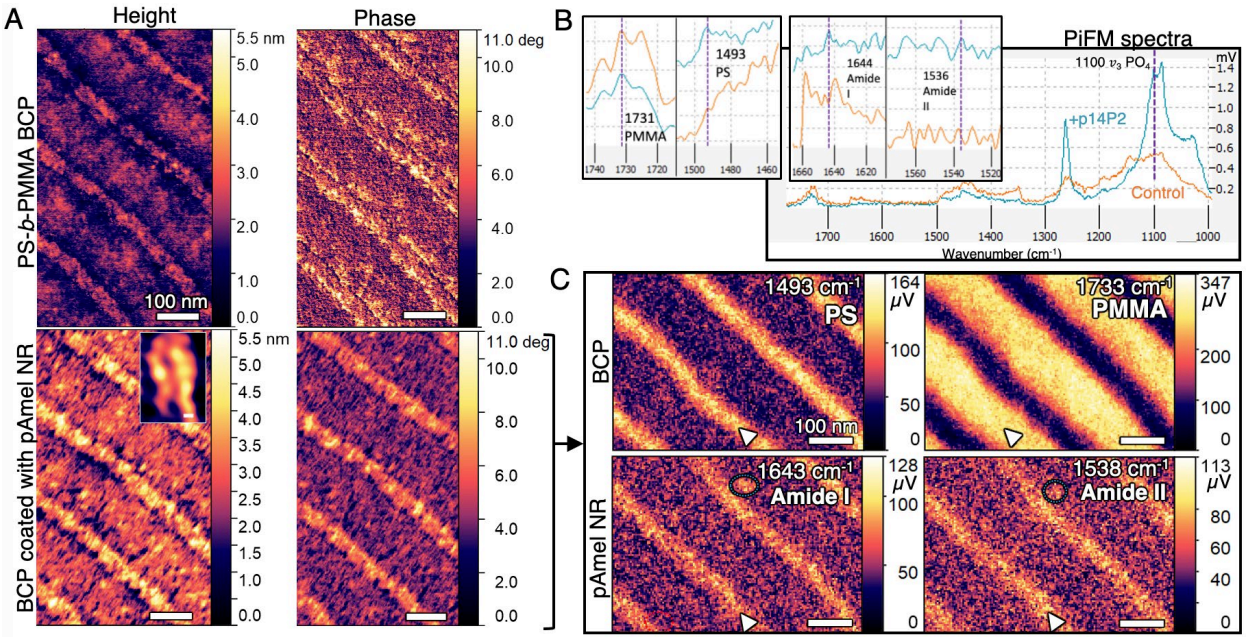

Figure 4.1. In situ AFM and PiFM of pAmel NRs assembled on 50 nm PS stripes of PS-b-PMMA BCPs. (**A)** BCP before and after incubation of 0.05 mg/mL p14P2 for 30 min shows height of PS and PMMA stripes increase by ~1.4 nm and ~0.6 nm, respectively along with significant change in phase contrast of PS stripes. (**B)** PiFM-IR spectra of BCPs with and without pAmel NR used to evaluate BCP and pAmel NR conformation. (**C**) PiFM surface map of pAmel NR coated BCP (dried) at excitation wavelengths specific to BCP and β-sheet pAmel NR shows pAmel NR assembled on PS stripes (bright stripes). Arrows indicate excited regions while circles indicate peptide with non-specific binding or cross-β-sheet pAmel NR on PMMA.

After washing and drying the BCP surfaces, Photo-induced Force Microscopy (PiFM) was performed for correlated local chemical and conformational spectroscopy. Excitation wavelengths specific to PS (1493 cm^{-1}), PMMA (1733 cm^{-1}), and β-sheet Amel NR (Amide I: 1643 cm^{-1} and Amide II: 1538 cm^{-1}) were identified through the spectra of bare BCP vs. pAmel NR coated BCP (Figure 4.1 B) and prior reports [86,156]. PiFM maps for BCP-p14P2 NR (Figure 4.1 C**)** highlighted

the location of the individual chemical species (bright stripes indicated by white arrows) and clearly demonstrates PS stripes predominantly bind pAmel NR with β-sheet conformation and the ~3 nm tall particles on PMMA (circles) are likely cross-β-sheets.

4.4 NUCLEATION OF ACP AT CONSTANT SUPERSATURATION

For mineralization, surfaces with peptide solutions are incubated at 37 ºC (100% relative humidity) for 60 min and excess solution is exchanged thoroughly with pure water. Classical heterogenous nucleation is performed on these substrates with calcium phosphate solutions supersaturated with respect to ACP (σ_{ACP}) without concomitant precipitation in bulk solution [40,120,129]. The nucleation dynamics, kinetics, and patterning fidelity on p14P2 and p14P2Cterm coated BCPs were determined by in situ AFM at constant $\sigma_{ACP} = 0.04$ using perfusion apparatus (**Figure 4.2 A to C**). The nucleated particles are extracted by exposing the substrate to ethanol that induces the BCP to swell and eject particles then characterized by high-resolution transmission electron microscopy (HRTEM) and selected area electron diffraction (SAED) (Figure 4.2 D).

We found β-sheets of both sequences nucleated calcium phosphate, which were amorphous under HRTEM and SAED, exhibiting high nuclei number density and sequence-specific ACP growth rates (p14P2Cterm > p14P2 in Figure 4.2 E), consistent with our previous results on graphite. Therefore, we infer the templating potency of pAmel NR-solution interfaces was transferred to the PS stripes and patterned supramolecular protein interfaces can be generated. Of the two sequences, p14P2 displayed higher fidelity than p14P2Cterm over time. Analysis shows high fidelity is achieved by p14P2 due to the high ACP nucleation rate on PS-p14P2, which is 8.4 times and 1.8 times higher than on PMMA-p14P2 and PS-p14P2Cterm respectively, and low

(vertical) growth rate of ACP on p14P2 which is 3/10th the rate on p14P2Cterm. Moreover, nucleation rates on PMMA for both sequences are similar (and low), however, overtime the ACP on PMMA-p14P2 dissolves while the ACP on PMMA-p14P2Cterm grows. The comparison also highlights local competition between nucleation of a new particle and growth of an existing particle; the Ca-PO_4 ion complexes prefer the β-sheet p14P2-solution interface over ACP-solution interface while they prefer the ACP-solution over the prefer the β-sheet p14P2Cterm-solution interface. In stark contrast, our controls—bare BCPs (without peptide coating), bare BCPs with 12 nm PS width and 24 nm periodicity (Figure 4.2 F), and BCPs with pre-assembled pAmel NRs randomly adsorbed and oriented—show no ACP nucleation and growth.

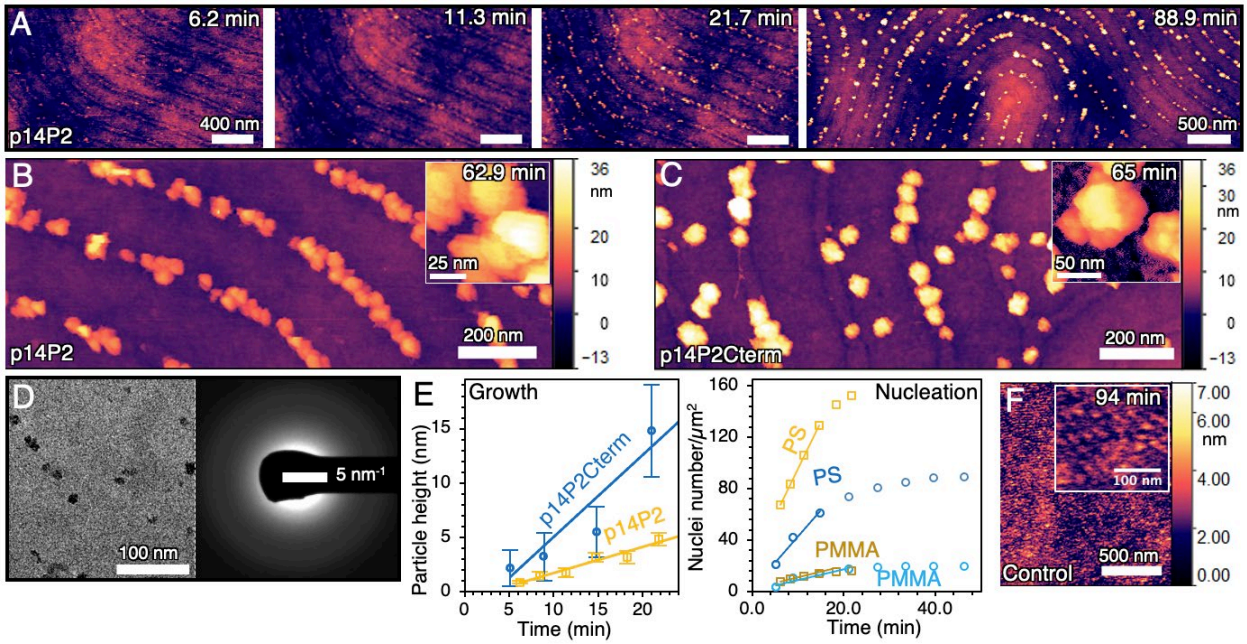

Figure 4.2. pAmel NR-PS stripes nucleate ACP under constant chemical potential. *In situ* AFM shows BCPs coated with (**A**) p14P2 nucleates and grows calcium phosphate particles over time. (**B**) p14P2 has high fidelity and (**C**) p14P2Cterm has lower fidelity and larger particles. (**D**) Under TEM and SAED, particles were amorphous. (**E**) Comparison of representative ACP nucleation and growth rates for p14P2 (yellow) and p14P2Cterm (blue). For nucleation rates, the number of nuclei on PS and PMMA are separated and normalized to their corresponding area. (**F**) Absence of mineralization on BCP (control (20 nm wide PS and PMMA) without pAmel NR after 94 min.

4.5 FILAMENT-LIKE APATITE USING POLYMER-INDUCED LIQUID PRECURSOR

Crystallization of many biogenic crystals is thought to be mediated by cooperative and site-specific interactions between the insoluble template and soluble macromolecules [19]. This typically involves nucleation of an amorphous or crystalline polymorph on the template from a polymer-induced liquid precursor (PILP) phase produced by addition of acidic macromolecules. For example, ACP nucleation to apatite transformation on amelogenin nanoribbons in developing tooth enamel [86], amorphous calcium carbonate in sea urchin spicule [12], aragonite on silk-fibroin-like protein, and calcite on periphery of coccolithophore baseplates [157]. Therefore, patterned pAmel NR-PS interfaces should template filament-like ACP or apatite from PILP phase since they localize ACP nucleation on surfaces with mixed interfaces. To test this conclusion, the pAmel NR-BCPs were exposed to PILP solutions of calcium phosphate with 27 kD poly-Aspartic acid (pAsp) additive [86] and characterized by AFM, HRTEM and SAED. Furthermore, we alter the PS stripe width to demonstrate the versatility of the BCPs patterns and determine impact of increasing pAmel NR-PS surface area. The altered BCPs have 95.2 ± 23.3 nm wide PS with 174.5 ± 12.4 nm periodicity (labelled as 95 nm PS) and 151.7 ± 14.6 nm wide PS and 249.7 ± 21.8 periodicity (labelled as 150 nm PS).

Multiple in situ AFM experiments with p14P2Cterm-BCP show all PS stripe widths do indeed template smooth, apatite crystals using PILP (**Figure 4.3 A** to **C**) and the width of the PS can control the size and width of the formed crystal (**Figure 4.3 D)**. The average thickness and width of these crystals were 20.1 ± 3.6 and 78.9 ± 10.8 nm for 50 nm PS, 7.8 ± 1.8 and 101.3 ± 18.7 nm for 95 nm PS, and 36.4 ± 27 and 108.7 ± 31.3 nm for 150 nm PS, respectively. The crystals

lack large grain boundaries, as seen in studies of calcium carbonate nucleation on SAMs [136], and exhibit *ab* planes ((202), (211) and (222)) of apatite normal to the crystal surface under SAED and HRTEM (**Figure 4.3 E**), similar to apatite in enamel [158]. Specificity of mineral to PS over PMMA stripes was 1.5 times higher on 90 nm PS than on 50 nm PS, but both PS form filament shaped mineral that lay along the length of the stripes. Whereas the crystals on 150 nm PS were shorter on average, nearly 1:1 in aspect ratio, and randomly oriented.

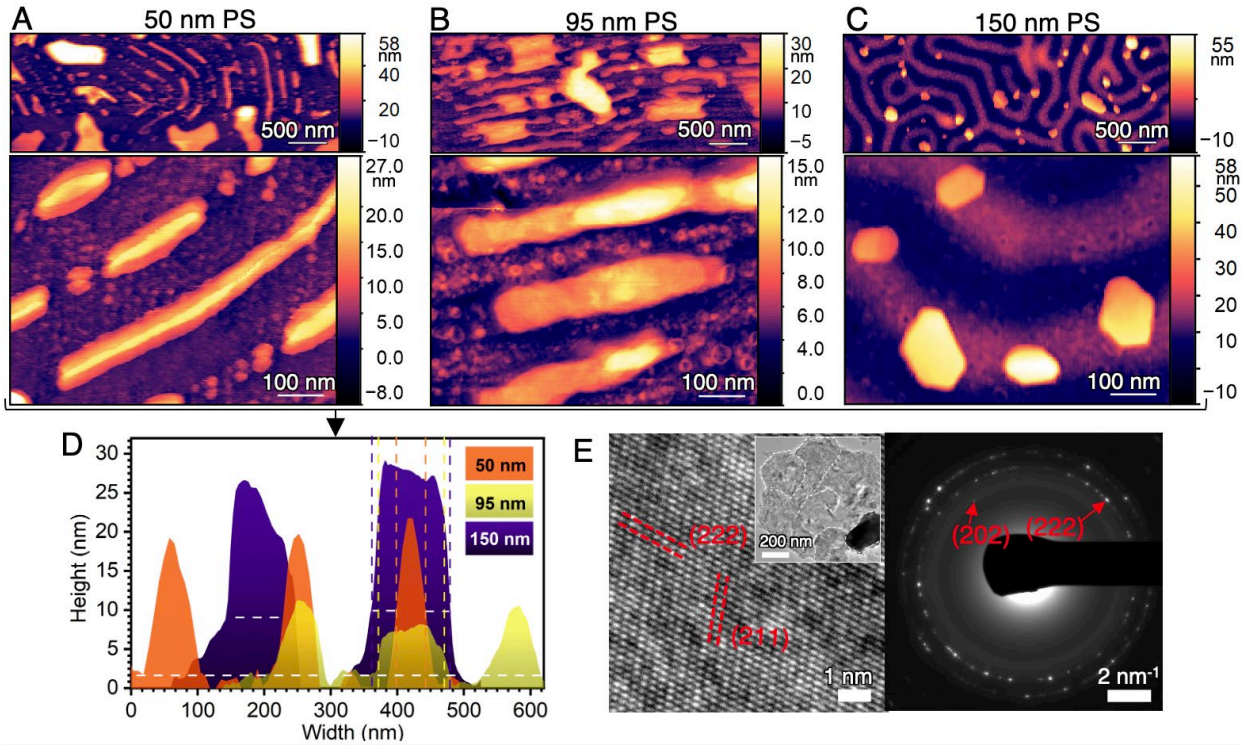

Figure 4.3. Smooth apatite crystals with tunable dimensions using PILP. *In situ* AFM shows filament-like morphology of the mineral particles with low surface roughness formed on p14P2Cterm-PS stripes for (**A**) 50 nm, (**B**) 95 nm and (**C**) 150 nm wide PS stripes. (**D**) Comparison of height profiles of crystals formed on 50, 95 and 150 nm p14P2Cterm-PS stripes; white horizontal dashes indicate base of the particle (PS stripe) and color-coded vertical dashes indicate the filament width. (**E**) Representative HRTEM and SAED analysis of extracted particles (shown for crystals in C) confirm the particles are crystalline with lattice and reflections specific to apatite.

The random orientation of the crystals on 150 nm PS compared to the 50 and 95 nm PS suggests the pAmel NRs alignment is relatively more isotropic on the 150 nm than the 50 and 95

nm PS. Similar experiments were performed on p14P2-BCP but yielded shorter crystals (156 ± 128 nm in length) compared to micrometer long crystals for p14P2Cterm-BCPs, likely due to the higher nuclei number density on PS and lower growth rate that leads more crystals, but smaller in size. Our future efforts will focus on developing local method of delivering PILP to the scaffold since the method used here has low fidelity compared to results of Fig. 2 though we attempted different conditions—heating to 50 ºC [86], cooling to 4 ºC [136], flow-through, drying [136], and inverted substrates suspended on solution [136].

4.6 IMPLICATIONS AND CONSTRAINTS FOR HIGH FIDELITY PATTERNING

In principle, a different supramolecular structure, such as collagen and SbpA S-layers [151], or a different mineral precursor chemistry, such as iron oxide, calcium carbonate and silica [33,159], can be used interchangeably to pattern other inorganic materials on BCPs via PILP or supersaturated solutions. Hence, based on ACP nucleation by p14P2 (Figure 4.2) and previous work [120], we outline structural and physicochemical constraints for high fidelity patterning as follows (**Figure 4.4**):

For protein design,

1) Match surface binding interface to one of the BCP chemistries.
2) Match stereochemistry of solution exposed interface to the desired inorganic material.
3) Use highly ordered supramolecular structures without minimal disordered domains, which exhibit low interfacial energy and high nucleation kinetics of the target mineral.

For BCPs,

1) Choose chemistry compatible with pH for protein assembly and mineralization.

2) Match the templating stripe width to the supramolecular structure dimension and use stripe periodicity ≥ protein-polymer stripe width to prevent coalescence of growing particles

And for mineral precursor solution,

1) Use supersaturated buffered solutions with saturation (σ) between 0.04 to 0.14 (though this can vary based on the system but can be explored using the methods described here) and no concomitant precipitation in bulk solution.

2) Increase mineralization duration to increase particle size.

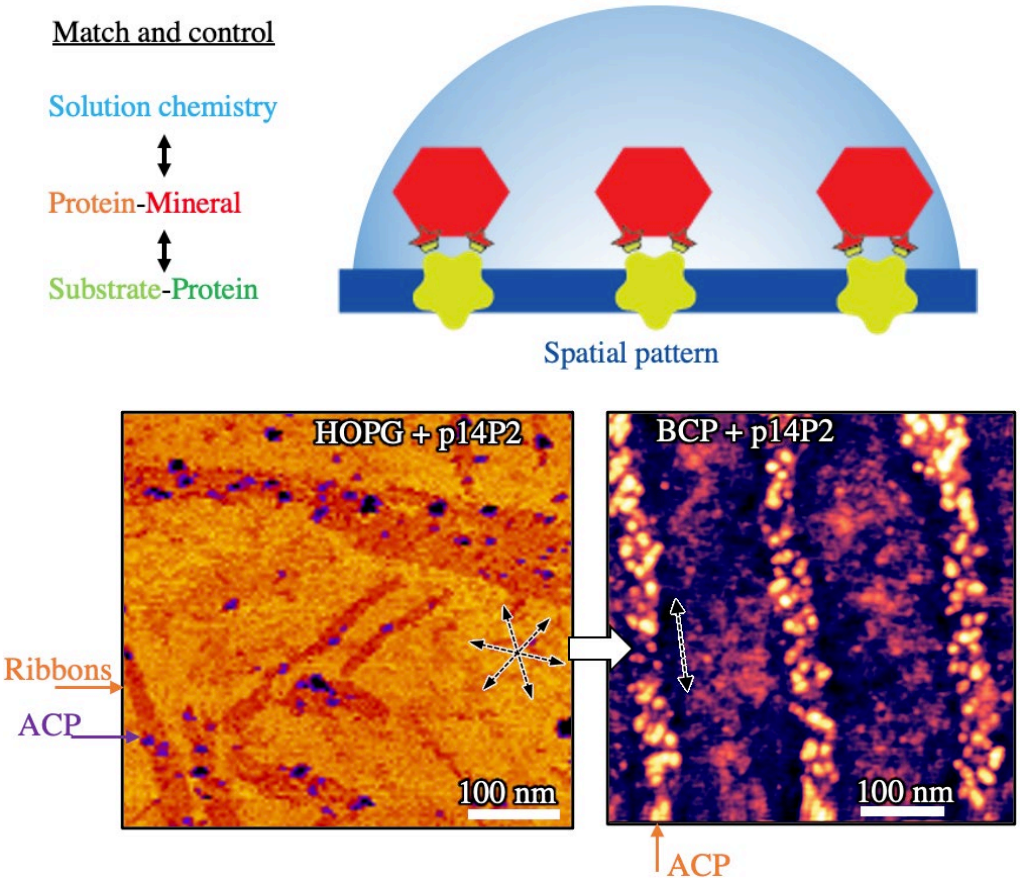

Figure 4.4. Parameters to match and control nucleation and growth at solid-liquid interfaces. ACP nucleated on p14P2 NRs aligned in three symmetric directions on HOPG vs. p14P2 NRs aligned on BCP lamellae on immersion in σ_{ACP}=0.04 solution for 20 min.

4.7 CONCLUSION

The primary findings from this fundamental study on the application of protein nanoribbons patterns as mineral templates show conformation and interfacial properties of phosphorylated Amel NRs previously seen on graphite are conserved on BCPs, even after 1D alignment and spatial patterning (**Figure 4.4**). pAmel NR β-sheet coated BCPs can effectively pattern amorphous mineral nucleation using supersaturated solutions and the number density and size of the mineral particles can be tuned through changes in mineralization duration and/or peptide sequence, while the disordered peptide monomers are unable to nucleate and grow mineral. Furthermore, in agreement with the templating function of pAmel NR β-sheet, the same substrates pattern smooth, filament-like mineral crystals via the use of acidic macromolecules in PILP-phase.

Taken together, the results here confirm the conclusions of our prior mechanistic study that demonstrated Amel NR as a template with a low-energy interface of ion-binding sites that is relevant to enamel biomineralization. Moreover, the observation of enamel-mimetic single crystals of apatite on BCP substrates with the PILP method does indeed strongly suggest *in vivo* enamel biomineralization may follow a similar mechanism. Therefore, we infer bottom-up, biomimetic (and biological) synthesis of patterned filamentous inorganic material on substrates may be possible through a combination of low energy barriers to nucleation, high nucleation rate, low growth rates, and discrete nucleation domains generated by aligned arrays of well-structured organic nanoribbons.

Chapter 5. SUMMARY AND OUTLOOK

This doctoral dissertation has focused on my efforts to understand the structural, physicochemical, mechanistic, and energetic factors governing protein-templated mineralization of biomaterials from *in situ* observations, with the goal of translating the knowledge towards scalable synthesis of organic-inorganic hybrid materials—ultimately to achieve unique properties. Besides the immediate impact on tissue engineering, such hybrid materials have immense potential to realize novel nano- electronic, optoelectronic, catalytic, or biomedical devices, and second, act as an ultra-lightweight protective layer for existing devices sensitive to ambient environment.

To briefly summarize, Chapter 1 introduced amyloid-like amelogenin nanoribbons (Amel NR) as the leading candidate for the structural motif of the protein scaffold that exists during enamel formation and guides formation of filamentous apatite crystals. Chapter 2 demonstrated new methods to assemble and characterize β-sheet Amel NRs in solution or as arrays of NRs on 2D materials. In Chapter 3, phosphorylated Amel NRs (pAmel NRs) were shown as more potent calcium phosphate nucleators than other amelogenin motifs or collagen, which provides the scaffold for bone. This potency stems from a periodic array of charged sites that provide a template for calcium phosphate ion binding on a low-energy interface. These findings establish the β-sheet amyloid-like structure of Amel-NR as a template of low interfacial energy for ACP nucleation and provide convincing evidence that the binding of anionic pre-nucleation complexes to the repeating pattern of phosphorylation sites is the key initial step in the mineralization process. In Chapter 4, the lessons learnt in Chapter 3 were translated towards developing methods for scalable synthesis of hierarchical materials. Here, assembly of β-sheet pAmel NRs was directed onto predefined

patterns of block copolymer (BCP) lamellae to demonstrate that nucleation can be localized to the pAmel NRs and generate arrays of highly aligned ACP or apatite crystals depending on the mineral precursor solution used. Finally, from this study, I infer that bottom-up, biomimetic fabrication of patterned filamentous inorganic material on substrates with high fidelity may be possible through the combination of low surface energy, high nucleation rate, and spatially separated discrete nucleation domains generated by aligned arrays of pAmel NR. These finding confirm the results of our mechanistic study on the function of Amel NR and the observation of single crystal apatite filaments on BCP substrates on using PILP do indeed show that *in vivo* mineralization may follow a similar mechanism.

The results here also provide evidence that one domain of an intrinsically disordered matrix protein can drive self-assembly into a template that stabilizes a mineral phase while leaving another domain flexible to interact with non-matrix proteins, ions or crystals [56,57]. The use of such domain-specific interfacial behavior towards crystal nucleation along with careful control of supersaturations can, in principle, be expanded beyond proteins to understanding and engineering crystallization on block copolymer, peptoid and other amphiphilic polymer templates [160–162], as shown in **Figure 5.1** from my experience in working with a wide variety of molecules.

Beyond fundamentals, the link between the self-assembled molecular structure of Amel NR templates and mineral nucleation points towards a range of translational opportunities (**Figure 5.1**). For example, the ability to readily assemble solid-binding peptides with control over orientation on crystalline surfaces like graphene[163], mica [164] or MoS_2 [125], or to array proteins on surfaces patterned at the nanoscale using block copolymers films [151], as well as nanolithography

[165], provides a potential path to organizing Amel NRs for engineering mineralized tissue and synthesis of hybrid materials.

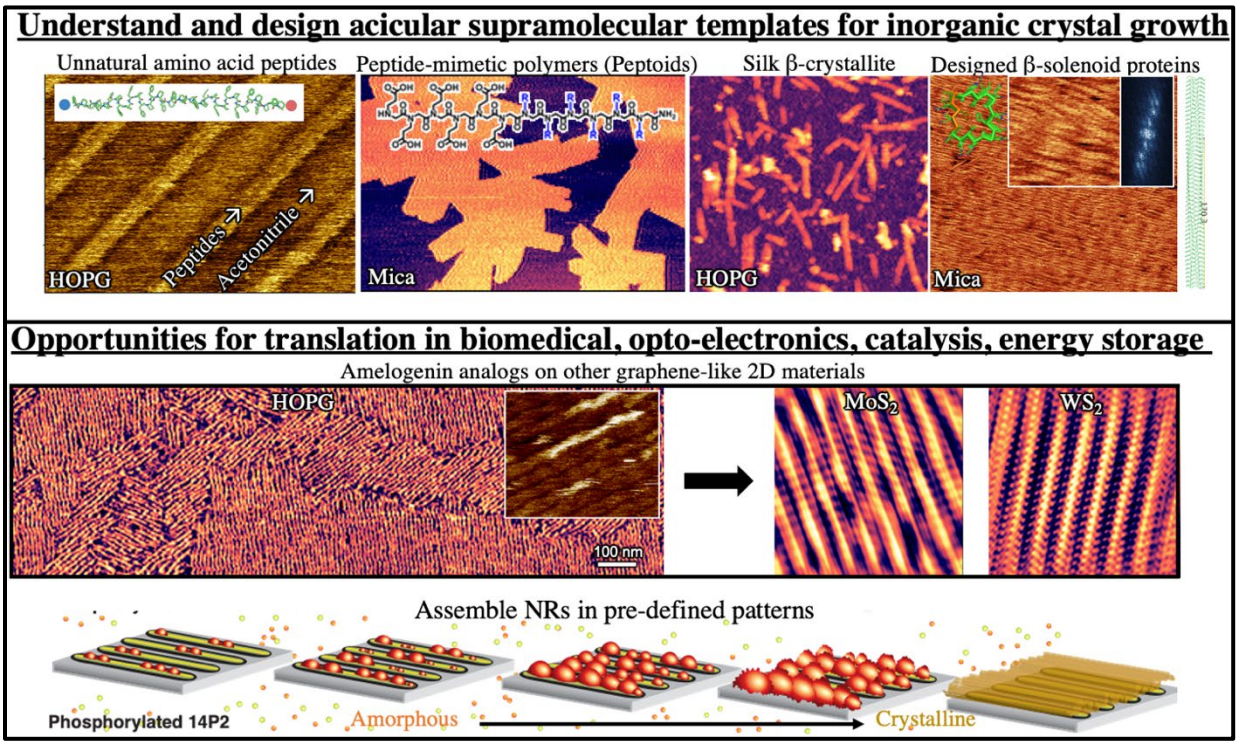

Figure 5.1. Expansion to other acicular supramolecular assemblies and translational opportunities for hybrid materials synthesis

Alternatively, the periodic organization of nucleation sites on the NRs suggests a means for creating patterns of quantum dots or oriented crystals of other materials by tailoring the site chemistry. More broadly, achieving predictive hierarchical growth of inorganic crystalline arrays directed by an organic scaffold, inspired by Nature**,** is a long sought-after vision of bioinspired material science. The robust hierarchical design of amyloid NRs arrayed with modular functional groups around a self-assembling domain, provides a general scaffold design upon which that vision may be realized.

BIBLIOGRAPHY

1. Kröger, N. & Brunner, E. Complex-shaped microbial biominerals for nanotechnology. *Wiley Interdisciplinary Reviews: Nanomedicine and Nanobiotechnology* **6**, 615–627 (2014).
2. Zhao, H. *et al.* Multiscale engineered artificial tooth enamel. *Science (1979)* **375**, 551–556 (2022).
3. Beniash, E. *et al.* The hidden structure of human enamel. *Nature Communications 2019 10:1* **10**, 1–13 (2019).
4. Rönnholm, E. An electron microscopic study of the amelogenesis in human teeth: I. The fine structure of the ameloblasts. *Journal of Ultrastructure Research* **6**, 229–248 (1962).
5. Jodaikin, A., Weiner, S. & Traub, W. Enamel rod relations in the developing rat incisor. *Journal of Ultrastructure Research* **89**, 324–332 (1984).
6. Daculsi, G. & Kerebel, B. High-resolution electron microscope study of human enamel crystallites: Size, shape, and growth. *Journal of Ultrastructure Research* **65**, 163–172 (1978).
7. Stifler, C. A. *et al.* X-ray Linear Dichroism in Apatite. *J Am Chem Soc* **140**, 11698–11704 (2018).
8. Wang, C. *et al.* The Enamel Microstructures of Bovine Mandibular Incisors. *The Anatomical Record: Advances in Integrative Anatomy and Evolutionary Biology* **295**, 1698–1706 (2012).
9. Pandya, M. *et al.* Posttranslational amelogenin processing and changes in matrix assembly during enamel development. *Frontiers in Physiology* **8**, (2017).
10. Antonio Nanci. *Ten Cate 's Oral histology 8th edition*. (2008).
11. Smith, C. E. Cellular and Chemical Events During Enamel Maturation. *Critical Reviews in Oral Biology & Medicine* **9**, 128–161 (1998).
12. Politi, Y., Arad, T., Klein, E., Weiner, S. & Addadi, L. Sea urchin spine calcite forms via a transient amorphous calcium carbonate phase. *Science (1979)* **306**, 1161–1164 (2004).
13. Towe, K. M. & Lowenstam, H. A. Ultrastructure and development of iron mineralization in the radular teeth of Cryptochiton stelleri (mollusca). *Journal of Ultrastructure Research* **17**, 1–13 (1967).
14. Moura, H. M. & Unterlass, M. M. Biogenic Metal Oxides. *Biomimetics 2020, Vol. 5, Page 29* **5**, 29 (2020).
15. Mahamid, J., Sharir, A., Addadi, L. & Weiner, S. Amorphous calcium phosphate is a major component of the forming fin bones of zebrafish: Indications for an amorphous precursor phase. *Proc Natl Acad Sci U S A* **105**, 12748–12753 (2008).

16. Beniash, E., Aizenberg, J., Addadi, L. & Weiner, S. Amorphous calcium carbonate transforms into calcite during sea urchin larval spicule growth. *Proceedings of the Royal Society B: Biological Sciences* **264**, 461 (1997).

17. Gong, Y. U. T. *et al.* Phase transitions in biogenic amorphous calcium carbonate. *Proc Natl Acad Sci U S A* **109**, 6088–6093 (2012).

18. Cölfen, H. (Helmut) & Antonietti, M. Mesocrystals and nonclassical crystallization. 276 (2008).

19. de Yoreo, J. J. *et al.* Crystallization by particle attachment in synthetic, biogenic, and geologic environments. *Science (1979)* **349**, aaa6760–aaa6760 (2015).

20. Mann, S. *et al.* Crystallization at Inorganic-organic Interfaces: Biominerals and Biomimetic Synthesis. *Science (1979)* **261**, 1286–1292 (1993).

21. Weiner, S. & Addadi, L. Design strategies in mineralized biological materials. *Journal of Materials Chemistry* **7**, 689–702 (1997).

22. Mann, S. Molecular tectonics in biomineralization and biomimetic materials chemistry. *Nature 1993 365:6446* **365**, 499–505 (1993).

23. Qiu, S. R. & Orme, C. A. Dynamics of Biomineral Formation at the Near-Molecular Level. *Chemical Reviews* **108**, 4784–4822 (2008).

24. Gilbert, P. U. P. A., Abrecht, M. & Frazer, B. H. The Organic-Mineral Interface in Biominerals. *Reviews in Mineralogy & Geochemistry* **59**, 157–185 (2005).

25. de Yoreo, J. J. & Vekilov, P. G. Principles of Crystal Nucleation and Growth. *Reviews in Mineralogy and Geochemistry* **54**, 57–93 (2003).

26. de Yoreo, J. J., Chung, S. & Nielsen, M. H. The Dynamics and Energetics of Matrix Assembly and Mineralization. *Calcified Tissue International* **93**, 316–328 (2013).

27. Elhadj, S., de Yoreo, J. J., Hoyer, J. R. & Dove, P. M. *Role of molecular charge and hydrophilicity in regulating the kinetics of crystal growth*. *PNAS* vol. 103 https://www.pnas.org/content/pnas/103/51/19237.full.pdf (2006).

28. Giuffre, A. J., Hamm, L. M., Han, N., de Yoreo, J. J. & Dove, P. M. Polysaccharide chemistry regulates kinetics of calcite nucleation through competition of interfacial energies. *Proc Natl Acad Sci U S A* **110**, 9261–6 (2013).

29. Hamm, L. M. *et al.* Reconciling disparate views of template-directed nucleation through measurement of calcite nucleation kinetics and binding energies. *Proc Natl Acad Sci U S A* **111**, 1304–9 (2014).

30. Gal, A. *et al.* Particle accretion mechanism underlies biological crystal growth from an amorphous precursor phase. *Advanced Functional Materials* **24**, 5420–5426 (2014).

31. Gal, A., Weiner, S. & Addadi, L. A perspective on underlying crystal growth mechanisms in biomineralization: solution mediated growth versus nanosphere particle accretion. *CrystEngComm* **17**, 2606–2615 (2015).

32. Olszta, M. J. *et al.* Bone structure and formation: A new perspective. *Materials Science and Engineering: R: Reports* **58**, 77–116 (2007).

33. Maria Oosterlaken, B. *et al.* In Vitro Mineralization of Collagen. *Advanced Materials* **33**, 2004418 (2021).

34. Lin, M. *et al.* Carboxymethyl chitosan as a polyampholyte mediating intrafibrillar mineralization of collagen via collagen/ACP self-assembly. *Journal of Materials Science & Technology* **35**, 1894–1905 (2019).

35. Ma, Y.-X. *et al.* Involvement of prenucleation clusters in calcium phosphate mineralization of collagen. *Acta Biomater* **120**, 213–223 (2021).

36. Nudelman, F. *et al.* The role of collagen in bone apatite formation in the presence of hydroxyapatite nucleation inhibitors. *Nature Materials* (2010) doi:10.1038/NMAT2875.

37. Tester, C. C. *et al.* Time-Resolved Evolution of Short- and Long-Range Order During the Transformation of Amorphous Calcium Carbonate to Calcite in the Sea Urchin Embryo. *Advanced Functional Materials* **23**, 4185–4194 (2013).

38. Yang, L., Killian, C. E., Kunz, M., Tamura, N. & Gilbert, P. U. P. A. Biomineral nanoparticles are space-filling. *Nanoscale* **3**, 603–609 (2011).

39. Addadi, L., Raz, S. & Weiner, S. Taking Advantage of Disorder: Amorphous Calcium Carbonate and Its Roles in Biomineralization. *Advanced Materials* **15**, 959–970 (2003).

40. Tao, J. *et al.* Control of Calcium Phosphate Nucleation and Transformation through Interactions of Enamelin and Amelogenin Exhibits the "goldilocks Effect." *Crystal Growth and Design* **18**, 7391–7400 (2018).

41. Tao, J., Buchko, G. W., Shaw, W. J., de Yoreo, J. J. & Tarasevich, B. J. Sequence-Defined Energetic Shifts Control the Disassembly Kinetics and Microstructure of Amelogenin Adsorbed onto Hydroxyapatite (100). *Langmuir* **31**, 10451–10460 (2015).

42. Tao, J., Pan, H., Zeng, Y., Xu, R. & Tang, R. Roles of amorphous calcium phosphate and biological additives in the assembly of hydroxyapatite nanoparticles. *Journal of Physical Chemistry B* **111**, 13410–13418 (2007).

43. Tao, J. *et al.* The energetic basis for hydroxyapatite mineralization by amelogenin variants provides insights into the origin of amelogenesis imperfecta. *Proc Natl Acad Sci U S A* **116**, 13867–13872 (2019).

44. Friddle, Dr. R. W. *et al.* Single-Molecule Determination of the Face-Specific Adsorption of Amelogenin's C-Terminus on Hydroxyapatite. *Angew Chem Int Ed Engl* **50**, 7541 (2011).

45. Weiner, S. Organization of Organic Matrix Components in Mineralized Tissues'. **24**, 945–951 (1984).

46. Addadi, L. & Weiner, S. Interactions between acidic proteins and crystals: stereochemical requirements in biomineralization. *Proc Natl Acad Sci U S A* **82**, 4110 (1985).

47. Moradian-Oldak, J. Protein-mediated enamel mineralization. *Front Biosci (Landmark Ed)* **17**, 1996–2023 (2012).

48. Vieira, A. R., Gibson, C. W., Deeley, K., Xue, H. & Li, Y. Weaker Dental Enamel Explains Dental Decay. *PLOS ONE* **10**, e0124236 (2015).

49. Gibson, C. W. *et al.* Rescue of the murine amelogenin null phenotype with two amelogenin transgenes. *European Journal of Oral Sciences* **119**, 70–74 (2011).

50. Lacruz, R. S., Habelitz, S., Wright, J. T. & Paine, M. L. Dental Enamel Formation and Implications for Oral Health and Disease. *Physiological Reviews* **97**, 939–993 (2017).

51. Gibson, C. W. *et al.* Amelogenin-deficient mice display an amelogenesis imperfecta phenotype. *J Biol Chem* **276**, 31871–5 (2001).

52. Anfinsen, C. B. Principles that govern the folding of protein chains. *Science* **181**, 223–30 (1973).

53. Delak, K. *et al.* The tooth enamel protein, porcine amelogenin, is an intrinsically disordered protein with an extended molecular configuration in the monomeric form. *Biochemistry* **48**, 2272–81 (2009).

54. Dunker, A. K. *et al.* Intrinsically disordered protein. *Journal of Molecular Graphics and Modelling* **19**, 26–59 (2001).

55. Dunker, A. K. *et al.* Intrinsically disordered protein. *Journal of Molecular Graphics and Modelling* **19**, 26–59 (2001).

56. Boskey, A. L. & Villarreal-Ramirez, E. Intrinsically disordered proteins and biomineralization. *Matrix Biol* **52–54**, 43–59 (2016).

57. Rao, A. *et al.* Stabilization of Mineral Precursors by Intrinsically Disordered Proteins. *Advanced Functional Materials* **28**, 1802063 (2018).

58. Baek, M. *et al.* Accurate prediction of protein structures and interactions using a three-track neural network. *Science (1979)* **373**, 871–876 (2021).

59. Jumper, J. *et al.* Highly accurate protein structure prediction with AlphaFold. *Nature 2021 596:7873* **596**, 583–589 (2021).

60. Ruan, Q. & Moradian-Oldak, J. Amelogenin and enamel biomimetics. *Journal of Materials Chemistry B* **3**, 3112–3129 (2015).

61. Wen, H. B., Fincham, A. G. & Moradian-Oldak, J. Progressive accretion of amelogenin molecules during nanospheres assembly revealed by atomic force microscopy. *Matrix Biology* **20**, 387–395 (2001).

62. Du, C., Falini, G., Fermani, S., Abbott, C. & Moradian-Oldak, J. Supramolecular assembly of amelogenin nanospheres into birefringent microribbons. *Science (1979)* **307**, 1450–1454 (2005).

63. Fang, P.-A., Conway, J. F., Margolis, H. C., Simmer, J. P. & Beniash, E. Hierarchical self-assembly of amelogenin and the regulation of biomineralization at the nanoscale. *Proceedings of the National Academy of Sciences* **108**, 14097–14102 (2011).

64. Martinez-Avila, O. *et al.* Self-Assembly of Filamentous Amelogenin Requires Calcium and Phosphate: From Dimers via Nanoribbons to Fibrils. *Biomacromolecules* **13**, 3494–3502 (2012).

65. Sanii, B., Martinez-Avila, O., Simpliciano, C., Zuckermann, R. N. & Habelitz, S. Matching 4.7-Å XRD Spacing in Amelogenin Nanoribbons and Enamel Matrix. *Journal of Dental Research* **93**, 918–922 (2014).

66. He, X., Wu, S., Martinez-Avila, O., Cheng, Y. & Habelitz, S. Self-aligning amelogenin nanoribbons in oil–water system. *Journal of Structural Biology* **174**, 203–212 (2011).

67. Moradian-Oldak, J. Amelogenins: assembly, processing and control of crystal morphology. *Matrix Biology* **20**, 293–305 (2001).

68. Lu, J. X., Xu, Y. S., Buchko, G. W. & Shaw, W. J. Mineral association changes the secondary structure and dynamics of murine amelogenin. *J Dent Res* **92**, 1000–4 (2013).

69. Kwak, S.-Y. *et al.* Regulation of calcium phosphate formation by amelogenins under physiological conditions. *European Journal of Oral Sciences* **119**, 103–111 (2011).

70. Beniash, E., Simmer, J. P. & Margolis, H. C. The effect of recombinant mouse amelogenins on the formation and organization of hydroxyapatite crystals in vitro. *Journal of Structural Biology* **149**, 182–190 (2005).

71. Bromley, K. M. *et al.* Dissecting Amelogenin Protein Nanospheres: CHARACTERIZATION OF METASTABLE OLIGOMERS*. *Journal of Biological Chemistry* **286**, 34643–34653 (2011).

72. Tarasevich, B. J. *et al.* The nucleation and growth of calcium phosphate by amelogenin. *Journal of Crystal Growth* **304**, 407–415 (2007).

73. le Norcy, E. *et al.* Leucine-rich amelogenin peptides regulate mineralization in vitro. *J Dent Res* **90**, 1091–7 (2011).

74. Tarasevich, B. J., Lea, S., Bernt, W., Engelhard, M. H. & Shaw, W. J. Changes in the quaternary structure of amelogenin when adsorbed onto surfaces. *Biopolymers* **91**, 103–107 (2009).

75. Fincham, A. G. *et al.* Evidence for Amelogenin "Nanospheres" as Functional Components of Secretory-Stage Enamel Matrix. *Journal of Structural Biology* **115**, 50–59 (1995).

76. Kwak, S.-Y. *et al.* Role of 20-kDa Amelogenin (P148) Phosphorylation in Calcium Phosphate Formation *in Vitro*. *Journal of Biological Chemistry* **284**, 18972–18979 (2009).

77. Masica, D. L., Gray, J. J. & Shaw, W. J. Partial High-Resolution Structure of Phosphorylated and Non-phosphorylated Leucine-Rich Amelogenin Protein Adsorbed to Hydroxyapatite. *The Journal of Physical Chemistry C* **115**, 13775–13785 (2011).

78. Buchko, G. W., Tarasevich, B. J., Bekhazi, J., Snead, M. L. & Shaw, W. J. A Solution NMR Investigation into the Early Events of Amelogenin Nanosphere Self-Assembly Initiated with Sodium Chloride or Calcium Chloride. *Biochemistry* **47**, 13215–13222 (2008).

79. Chen, C.-L., Bromley, K. M., Moradian-Oldak, J. & DeYoreo, J. J. In situ AFM Study of Amelogenin Assembly and Disassembly Dynamics on Charged Surfaces

Provides Insights on Matrix Protein Self-Assembly. *J Am Chem Soc* **133**, 17406–17413 (2011).

80. Paine, M. L. *et al.* Enamel Biomineralization Defects Result from Alterations to Amelogenin Self-Assembly. *Journal of Structural Biology* **132**, 191–200 (2000).
81. Carneiro, K. M. M. *et al.* Amyloid-like ribbons of amelogenins in enamel mineralization. *Scientific Reports* **6**, 1–11 (2016).
82. Pautard, F. G. E. An X-ray diffraction pattern from human enamel matrix. *Archives of Oral Biology* **3**, 217-IN13 (1961).
83. Jodaikin, A., Traub, W. & Weiner, S. Protein conformation in rat tooth enamel. *Archives of Oral Biology* **31**, 685–689 (1986).
84. Bai, P. & Warshawsky, H. Morphological studies on the distribution of enamel matrix proteins using routine electron microscopy and freeze-fracture replicas in the rat incisor. *The Anatomical Record* **212**, 1–16 (1985).
85. Travis, D. F. & Glimcher, M. J. The structure and organization of, and the relationship between the organic matrix and the inorganic crystals of embryonic bovine enamel. *The Journal of Cell Biology* **23**, 447–497 (1964).
86. Bai, Y. *et al.* Protein nanoribbons template enamel mineralization. *Proc Natl Acad Sci U S A* **117**, 19201–19208 (2020).
87. Huang, Y. *et al.* A N-Terminus Domain Determines Amelogenin's Stability to Guide the Development of Mouse Enamel Matrix. *Journal of Bone and Mineral Research* **n/a**, (2021).
88. Engelberth, S. A. *et al.* Progression of Self-Assembly of Amelogenin Protein Supramolecular Structures in Simulated Enamel Fluid. *Biomacromolecules* **19**, 3917–3924 (2018).
89. Martinez-Avila, O. M. *et al.* Self-assembly of amelogenin proteins at the water-oil interface. *European Journal of Oral Sciences* **119**, 75–82 (2011).
90. Sneideris, T. *et al.* pH-Driven Polymorphism of Insulin Amyloid-Like Fibrils. *PLOS ONE* **10**, e0136602 (2015).
91. Chiti, F. & Dobson, C. M. Protein Misfolding, Functional Amyloid, and Human Disease. *Annual Review of Biochemistry* **75**, 333–366 (2006).
92. Nelson, R. *et al.* Structure of the cross-β spine of amyloid-like fibrils. *Nature* **435**, 773–778 (2005).
93. Schleeger, M. *et al.* Amyloids: From molecular structure to mechanical properties. *Polymer (Guildf)* **54**, 2473–2488 (2013).
94. Wei, G. *et al.* Self-assembling peptide and protein amyloids: from structure to tailored function in nanotechnology. *Chemical Society Reviews* **46**, 4661–4708 (2017).
95. Serpell, L. C. Alzheimer's amyloid fibrils: structure and assembly. *Biochimica et Biophysica Acta (BBA) - Molecular Basis of Disease* **1502**, 16–30 (2000).
96. Fowler, D. M., Koulov, A. v., Balch, W. E. & Kelly, J. W. Functional amyloid – from bacteria to humans. *Trends in Biochemical Sciences* **32**, 217–224 (2007).

97. Walsh, D. M., Lomakin, A., Benedek, G. B., Condron, M. M. & Teplow, D. B. Amyloid β-protein fibrillogenesis: Detection of a protofibrillar intermediate. *Journal of Biological Chemistry* **272**, 22364–22372 (1997).

98. Srinivasan, R. *et al.* pH-Dependent Amyloid and Protofibril Formation by the ABri Peptide of Familial British Dementia. *Journal of Molecular Biology* **333**, 1003–1023 (2003).

99. Carrotta, R., Manno, M., Bulone, D., Martorana, V. & San Biagio, P. L. Protofibril formation of amyloid beta-protein at low pH via a non-cooperative elongation mechanism. *J Biol Chem* **280**, 30001–8 (2005).

100. Bai, Y. *et al.* A Brief History of the Discovery of Amelogenin Nanoribbons In Vitro and In Vivo. *Journal of Dental Research* **100**, 1429–1433 (2021).

101. Habelitz, S. & Bai, Y. Mechanisms of Enamel Mineralization Guided by Amelogenin Nanoribbons. *Journal of Dental Research* **100**, 1434–1443 (2021).

102. Nyrkova, I. A. *et al.* Self-assembly and structure transformations in living polymers forming fibrils. *The European Physical Journal B* **17**, 499–513 (2000).

103. Ionescu-Zanetti, C. *et al.* Monitoring the assembly of Ig light-chain amyloid fibrils by atomic force microscopy. *Proceedings of the National Academy of Sciences* **96**, 13175–13179 (1999).

104. Arce, F. T. *et al.* Polymorphism of amyloid β peptide in different environments: implications for membrane insertion and pore formation. *Soft Matter* **7**, 5267 (2011).

105. Arosio, P., Knowles, T. P. J. & Linse, S. On the lag phase in amyloid fibril formation. *Physical Chemistry Chemical Physics* **17**, 7606–7618 (2015).

106. Ma, C.-W., Zhang, J., Dong, X.-Q. & Lu, J.-X. Amyloid structure of high-order assembly of Leucine-rich amelogenin revealed by solid-state NMR. *Journal of Structural Biology* **206**, 29–35 (2019).

107. Shaw, W. J., Ferris, K., Tarasevich, B. & Larson, J. L. The Structure and Orientation of the C-Terminus of LRAP. *Biophysical Journal* **94**, 3247–3257 (2008).

108. Wu, S. *et al.* In Situ Atomic Force Microscopy Imaging of Octacalcium Phosphate Crystallization and Its Modulation by Amelogenin's C-Terminus. *Crystal Growth and Design* **17**, 2194–2202 (2017).

109. Shaw, W. J., Tarasevich, B. J., Buchko, G. W., Arachchige, R. M. J. & Burton, S. D. Controls of nature: Secondary, tertiary, and quaternary structure of the enamel protein amelogenin in solution and on hydroxyapatite. *Journal of Structural Biology* **212**, 107630 (2020).

110. Shin, N. Y. *et al.* Amelogenin phosphorylation regulates tooth enamel formation by stabilizing a transient amorphous mineral precursor. *Journal of Biological Chemistry* **295**, 1943–1959 (2020).

111. Fincham, A. G. & Moradianoldak, J. Amelogenin Post-translational Modifications: Carboxy-Terminal Processing and the Phosphorylation of Bovine and Porcine "TRAP" and "LRAP" Amelogenins. *Biochemical and Biophysical Research Communications* **197**, 248–255 (1993).

112. Beniash, E., Metzler, R. A., Lam, R. S. K. & Gilbert, P. U. P. A. Transient amorphous calcium phosphate in forming enamel. *Journal of Structural Biology* **166**, 133–143 (2009).

113. Gungormus, M. *et al.* Cementomimetics—constructing a cementum-like biomineralized microlayer via amelogenin-derived peptides. *International Journal of Oral Science* **4**, 69–77 (2012).

114. Gopinathan, G. *et al.* The expanded amelogenin polyproline region preferentially binds to apatite versus carbonate and promotes apatite crystal elongation. *Frontiers in Physiology* **5**, (2014).

115. Zhang, X., Ramirez, B. E., Liao, X. & Diekwisch, T. G. H. Amelogenin Supramolecular Assembly in Nanospheres Defined by a Complex Helix-Coil-PPII Helix 3D-Structure. *PLOS ONE* **6**, e24952 (2011).

116. Jin, T. *et al.* Elongated polyproline motifs facilitate enamel evolution through matrix subunit compaction. *PLoS Biology* **7**, (2009).

117. Wang, Y. *et al.* Formation of Amyloid Fibrils In Vitro from Partially Unfolded Intermediates of Human γC-Crystallin. *Investigative Ophthalmology & Visual Science* **51**, 672–678 (2010).

118. Harper, J. D., Wong, S. S., Lieber, C. M. & Lansbury, P. T. Assembly of Aβ Amyloid Protofibrils: An in Vitro Model for a Possible Early Event in Alzheimer's Disease. *Biochemistry* **38**, 8972–8980 (1999).

119. Jin, H. *et al.* Highly stable and self-repairing membrane-mimetic 2D nanomaterials assembled from lipid-like peptoids. *Nature Communications* **7**, 12252 (2016).

120. Akkineni, S. *et al.* Amyloid-like amelogenin nanoribbons template mineralization via a low-energy interface of ion binding sites. *Proceedings of the National Academy of Sciences* **119**, (2022).

121. Kowalewski, T. & Holtzman, D. M. In situ atomic force microscopy study of Alzheimer's beta-amyloid peptide on different substrates: new insights into mechanism of beta-sheet formation. *Proc Natl Acad Sci U S A* **96**, 3688–93 (1999).

122. Ruggeri, F. S. *et al.* Identification and nanomechanical characterization of the fundamental single-strand protofilaments of amyloid α-synuclein fibrils. *Proceedings of the National Academy of Sciences* **115**, 7230 LP – 7235 (2018).

123. Li, N. *et al.* Graphite-Templated Amyloid Nanostructures Formed by a Potential Pentapeptide Inhibitor for Alzheimer's Disease: A Combined Study of Real-Time Atomic Force Microscopy and Molecular Dynamics Simulations. *Langmuir* **33**, 6647–6656 (2017).

124. Arimon, M. *et al.* Fine structure study of Aβ 1–42 fibrillogenesis with atomic force microscopy. *The FASEB Journal* **19**, 1344–1346 (2005).

125. Chen, J. *et al.* Building two-dimensional materials one row at a time: Avoiding the nucleation barrier. *Science (1979)* **362**, 1135–1139 (2018).

126. Sun, L. *et al.* Chiral Recognition of Self-Assembled Peptides on MoS2 via Lattice Matching. *Langmuir* **37**, 8696–8704 (2021).

127. Heinz, H., Lin, T.-J., Kishore Mishra, R. & Emami, F. S. Thermodynamically Consistent Force Fields for the Assembly of Inorganic, Organic, and Biological Nanostructures: The INTERFACE Force Field. *Langmuir* **29**, 1754–1765 (2013).

128. Pramanik, C., Gissinger, J. R., Kumar, S. & Heinz, H. Carbon Nanotube Dispersion in Solvents and Polymer Solutions: Mechanisms, Assembly, and Preferences. *ACS Nano* **11**, 12805–12816 (2017).

129. Habraken, W. J. E. M. *et al.* Ion-association complexes unite classical and non-classical theories for the biomimetic nucleation of calcium phosphate. *Nature Communications* **4**, 1507 (2013).

130. Chien, Y.-C. *et al.* Using biomimetic polymers in place of noncollagenous proteins to achieve functional remineralization of dentin tissues. *ACS Biomater Sci Eng* **3**, 3469–3479 (2017).

131. Hu, Q. *et al.* The thermodynamics of calcite nucleation at organic interfaces: Classical vs. non-classical pathways †. *Faraday Discuss* **159**, 509–523 (2012).

132. Kashchiev, D. & van Rosmalen, G. M. Review: Nucleation in solutions revisited. *Crystal Research and Technology* **38**, 555–574 (2003).

133. Lu, Y. *et al.* Functions of KLK4 and MMP-20 in dental enamel formation. *Biological Chemistry* **389**, (2008).

134. Hoff, S. E., Liu, J. & Heinz, H. Binding mechanism and binding free energy of amino acids and citrate to hydroxyapatite surfaces as a function of crystallographic facet, pH, and electrolytes. *J Colloid Interface Sci* **605**, 685–700 (2021).

135. Jee, S.-S., Thula, T. T. & Gower, L. B. Development of bone-like composites via the polymer-induced liquid-precursor (PILP) process. Part 1: Influence of polymer molecular weight. (2010) doi:10.1016/j.actbio.2010.03.036.

136. Kim, Y. Y., Douglas, E. P. & Gower, L. B. Patterning inorganic (CaCO3) thin films via a polymer-induced liquid-precursor process. *Langmuir* **23**, 4862–4870 (2007).

137. Wald, T. *et al.* Intrinsically disordered proteins drive enamel formation via an evolutionarily conserved self-assembly motif. *Proc Natl Acad Sci U S A* **114**, E1641–E1650 (2017).

138. Iline-Vul, T. *et al.* Osteopontin regulates biomimetic calcium phosphate crystallization from disordered mineral layers covering apatite crystallites. *Sci Rep* **10**, 15722 (2020).

139. Mann, S. & Ozin, G. A. Synthesis of inorganic materials with complex form. *Nature 1996 382:6589* **382**, 313–318 (1996).

140. Rurack, K. & Martã-nez-Mãã ez, R. The Supramolecular Chemistry of Organic-Inorganic Hybrid Materials. *The Supramolecular Chemistry of Organic-Inorganic Hybrid Materials* (2010) doi:10.1002/9780470552704.

141. Faustini, M., Nicole, L., Ruiz-Hitzky, E. & Sanchez, C. History of Organic–Inorganic Hybrid Materials: Prehistory, Art, Science, and Advanced Applications. *Advanced Functional Materials* **28**, 1704158 (2018).

142. Guo, Z., Richardson, J. J., Kong, B. & Liang, K. Nanobiohybrids: Materials approaches for bioaugmentation. *Science Advances* **6**, 330–348 (2020).

143. Majewski, P. W. *et al.* Resilient three-dimensional ordered architectures assembled from nanoparticles by DNA. *Science Advances* **7**, (2021).

144. Aizenberg, J. Crystallization in Patterns: A Bio-Inspired Approach. *Advanced Materials* **16**, 1295–1302 (2004).

145. Chung, S., Chung, J., Wang, D., Lee, S.-W. & de Yoreo, J. J. Growth of Au and ZnS nanostructures via engineered peptide and M13 bacteriophage templates †. *2996 | Soft Matter* **14**, 2996 (2018).

146. Friddle, R. W. *et al.* Subnanometer atomic force microscopy of peptide-mineral interactions links clustering and competition to acceleration and catastrophe. *Proc Natl Acad Sci U S A* **107**, 11–5 (2010).

147. Deng, N. *et al.* Organic-mineral interfacial chemistry drives heterogeneous nucleation of Sr-rich (Bax, Sr1-x)SO4 from undersaturated solution. *Proc Natl Acad Sci U S A* **116**, 13221–13226 (2019).

148. Joanna Aizenberg, *,†, Andrew J. Black, ‡ and & George M. Whitesides*, ‡. Oriented Growth of Calcite Controlled by Self-Assembled Monolayers of Functionalized Alkanethiols Supported on Gold and Silver. (1999) doi:10.1021/JA984254K.

149. Kisailus, D., Truong, Q., Amemiya, Y., Weaver, J. C. & Morse, D. E. Self-assembled bifunctional surface mimics an enzymatic and templating protein for the synthesis of a metal oxide semiconductor. *Proceedings of the National Academy of Sciences* **103**, 5652–5657 (2006).

150. Xie, T. *et al.* Surface Assembly Configurations and Packing Preferences of Fibrinogen Mediated by the Periodicity and Alignment Control of Block Copolymer Nanodomains. *ACS Nano* **10**, 7705–7720 (2016).

151. Stel, B. *et al.* Contrasting Chemistry of Block Copolymer Films Controls the Dynamics of Protein Self-Assembly at the Nanoscale. *ACS Nano* **13**, 4018–4027 (2019).

152. Susca, E. M. *et al.* Preparation of Macroscopic Block-Copolymer-Based Gyroidal Mesoscale Single Crystals by Solvent Evaporation. *Advanced Materials* **31**, 1902565 (2019).

153. Onses, M. S. *et al.* Hierarchical patterns of three-dimensional block-copolymer films formed by electrohydrodynamic jet printing and self-assembly. *Nature Nanotechnology 2013 8:9* **8**, 667–675 (2013).

154. Scalfani, V. F., Turner, C. H., Rupar, P. A., Jenkins, A. H. & Bara, J. E. 3D Printed Block Copolymer Nanostructures. *Journal of Chemical Education* **92**, 1866–1870 (2015).

155. Cummins, C. *et al.* Enabling future nanomanufacturing through block copolymer self-assembly: A review. *Nano Today* **35**, 100936 (2020).

156. Nowak, D. *et al.* Nanoscale chemical imaging by photoinduced force microscopy. *Science Advances* **2**, (2016).

157. Gal, A. *et al.* Macromolecular recognition directs calcium ions to coccolith mineralization sites. *Science (1979)* **353**, 590–593 (2016).

158. DeRocher, K. A. *et al.* Chemical gradients in human enamel crystallites. *Nature 2020 583:7814* **583**, 66–71 (2020).

159. Oosterlaken, B. M. *et al.* Time-resolved cryo-TEM study on the formation of iron hydroxides in a collagen matrix. *ACS Biomaterials Science and Engineering* **7**, 3123–3131 (2021).

160. Oleske, K. W. *et al.* Nanopatterning of Crystalline Transition Metal Oxides by Surface Templated Nucleation on Block Copolymer Mesostructures. *Crystal Growth & Design* **17**, 5775–5782 (2017).

161. Kim, Y.-Y. *et al.* Hydroxyl-rich macromolecules enable the bio-inspired synthesis of single crystal nanocomposites. *Nature Communications* **10**, 5682 (2019).

162. Yan, F. *et al.* Controlled synthesis of highly-branched plasmonic gold nanoparticles through peptoid engineering. *Nature Communications* **9**, 2327 (2018).

163. Sarikaya, M., Tamerler, C., Jen, A. K.-Y., Schulten, K. & Baneyx, F. Molecular biomimetics: nanotechnology through biology. *Nature Materials* **2**, 577–585 (2003).

164. Pyles, H., Zhang, S., De Yoreo, J. J. & Baker, D. Controlling protein assembly on inorganic crystals through designed protein interfaces. *Nature* **571**, 251–256 (2019).

165. Lee, K.-B., Park, S.-J., Mirkin, C. A., Smith, J. C. & Mrksich, M. Protein Nanoarrays Generated By Dip-Pen Nanolithography. *Science (1979)* **295**, 1702–1705 (2002).

APPENDIX A: ARTICLES AND CONFERENCES

Peer-reviewed articles

- **Amyloid-like amelogenin nanoribbons template mineralization via a low energy interface of ion binding sites. S Akkineni**, C Zhu, J Chen, M Song, S E Hoff, J S Bonde, H Heinz, S Habelitz, J J De Yoreo. *Proceedings of the National Academy of Sciences* **119**, (2022).

- **Highly bright and photostable two-dimensional nanomaterials assembled from sequence-defined peptoids**. Song, Y; Wang, M; **Akkineni**, S; Yang, W; Hettige, J; Jin, H; Liao, Z; Mu, P; Yan, F; Baer, M D; De Yoreo, J; Du, D; Lin, Y; Chen, C. *ACS Materials Letters*. 2021

- **Controlling Metal-organic Framework/ZnO heterostructure kinetics through selective ligand binding to ZnO surface steps**. J Tao, M Lee, M L Sushko, J J De Yoreo, J Liu, Z Zhang, D Banerjee, **S Akkineni**, M E Bowden, P K Thallapally, Y Shin, M A Sinnwell. *Chemistry of Materials*. 2020

- **Solid-Binding Peptide-Guided Spatially Directed Immobilization of Kinetically Matched Enzyme Cascades in Membrane Nanoreactors**. DT Yucesoy, **S Akkineni,** B Hinds, Candan Tamerler, M Sarikaya. *ACS Omega*. 2021

Conferences

1. Biomimetic templating of calcium phosphate via patterned amelogenin nanoribbons. S Akkineni, C Zhu, G Doerk, J Chen, M Song, S Zhang, J S. Bonde, A Kulkarni, S E. Hoff, J Tao, H Heinz, S Habelitz, J J De Yoreo. **Enamel-X, 2022.** (Talk). Travel Award

2. Templating of calcium phosphate via patterned protein nanoribbons: a biomimetic approach to enamel tissue engineering. S Akkineni, C Zhu, G Doerk, J Chen, M Song, S Zhang, J S. Bonde, A Kulkarni, S E. Hoff, J Tao, H Heinz, S Habelitz, J J De Yoreo. **Materials Research Society, Spring 2022.** (Talk)

3. Amyloid-like amelogenin nanoribbons template mineralization via a low energy interface of ion bindings sites. S Akkineni, C Zhu, J Chen, M Song, S E Hoff, J S Bonde, H Heinz, S Habelitz, J J De Yoreo. **American Association for Crystal Growth and Epitaxy, 2021.** (Talk)

4. Periodic phosphorylation and disordered domain in amyloid nanoribbons impact nucleation and growth of amorphous mineral. S Akkineni, C Zhu, J Chen, M Song, S E Hoff, J S Bonde, H Heinz, S Habelitz, J J De Yoreo. **Materials Research Society, Spring 2021.** (Talk)

5. Impact Of Amyloid Structure And Phosphorylation Of Amelogenin And Its Peptide Analogs on Apatite Nucleation. S Akkineni, J Tao, J Chen, J Bonde, S Habelitz, J De Yoreo. **Enamel-10, 2020**. Young Investigator award

6. Impact of amyloid structure and phosphorylation of amelogenin and its peptide analogs on apatite nucleation. S Akkineni, J Tao, J Chen, J Bonde, S Habelitz, J De Yoreo. 13th **International Conference on the Chemistry and Biology of Mineralized Tissues. Montreal, Quebec, Canada**, **2019**. (Poster)

7. On the structure-function of amyloid-water interfaces in enamel biomineralization. S Akkineni, J Tao, B Legg, J Chen, J Bonde, S Habelitz, J De Yoreo. **Gordon Research Seminar and Conference. 2019**. **(**Poster)**.** Travel Award

8. On the kinetics and dynamics of apatite crystallization at amyloid-solution interfaces found during enamel biomineralization. S Akkineni**,** J Tao, B Legg, J Chen, J Bonde, S Habelitz, J De Yoreo. **American Physical Society. Boston, 2019.** (Poster)

9. Techniques to investigate apatite crystal growth on amyloid-like amelogenin fibrils. S Akkineni, S Engelberth, J Tao, J Bonde, S Habelitz, J De Yoreo. 73rd **ACS Northwest Regional Meeting NORM**, Richland, WA **2018** (Poster)

10. Role of amyloid-like amelogenin nanoribbons in enamel mineralization. S Akkineni, S Engelberth, J Tao, J Bonde, S Habelitz, J De Yoreo. Abstracts of 26th **AACGE Western Section Conference on Crystal Growth & Epitaxy**, Fallen Leaf Lake, CA **2018** (Talk)

11. Role of amelogenin β-sheet ribbons in biomineralization of hydroxyapatite. S Akkineni, S Engelberth, J Tao, J Bonde, S Habelitz, J De Yoreo. **ACS National Meeting**. New Orleans, LA, **2018**. (Talk)

12. *NI LabVIEW Based Embedded Text and Speech Synthesizer in Haptic Gloves for Sign Language Translation.* S. Akkineni*, R. Vasireddy*, S. Gupta*, A.K. Jayanthy. **Proceedings of International Conference on Biomedical Systems, Signals and Images** (**BSSI 2012**), Indian Institute of Technology-Madras, India. **(**Poster)

VITA

Susrut Akkineni received his Bachelors in Electronics and Instrumentation Engineering from SRM University, India. During his final year, he was fascinated by biominerals and developed a passion to create better devices using nanomaterials and biomimicry. For a short time in undergrad, he worked on a biomimetic nanomaterial synthesis project with Dr Yuxin Tang in Prof. Xiaodong Chen's group at Nanyang Technological University, Singapore. Subsequently, he obtained a Master's in Materials Science and Engineering at the University of Washington in 2015 while working with Prof. Bruce Hinds to develop bio-inspired membrane devices for protein purification and enzymatic catalysis. Following an interest in developing scalable bio-inspired methods for materials synthesis, he later returned to the University of Washington in September 2016 to join the Ph.D. program supervised by Prof. James De Yoreo, with the goal of understanding the fundamentals of organic matrix-mediated inorganic material synthesis in biomineralization. Susrut soon moved to the De Yoreo group at Pacific Northwest National Laboratory, Richland in May 2017 to use and develop a broad range of high-resolution techniques in microscopy and spectroscopy to study biomolecular self-assembly at solid-liquid interfaces, and investigate calcium phosphate nucleation, growth, and phase transformation on amyloid-like nanoribbons.